THE STUDY OF ELECTRICAL AND ELECTROCHEMICAL IMPEDANCE BEHAVIORS BY THE DISTRIBUTION OF PHYSICAL PROPERTIES OF COATED MATERIALS

A Dissertation

by

SEONGKOO CHO

Submitted to the Office of Graduate and Professional Studies of
Texas A&M University
in partial fulfillment of the requirements for the degree of

DOCTOR OF PHILOSOPHY

Chair of Committee,	Homero Castaneda
Committee Members,	Hung-Jue Sue
	Sarbajit Banerjee
	Ankit Srivastava
Head of Department,	Ibrahim Karaman

May 2020

Major Subject: Materials Science and Engineering

ABSTRACT

Impedance spectroscopy has been widely used to understand electric- and electrochemistry-related research. The use of impedance spectroscopy allows fast and reliable determination of material degradation and corrosion protection performance. Despite such advantages, there have been difficulties in the impedance analysis by various superimposed physical processes. The objective of this research was to specify the physical meaning by interpreting non-ideal and non-conventional impedance spectra.

A deterministic-probabilistic 2D impedance model was proposed to represent the physical degradation of a multi-layered coating system. The model allowed to overcome the limitations existed in the 1D model, such as limited parameter domain, by interpreting the effect of pore distribution in the 2D coating space. As a result, the effect of electrolyte penetration and self-healing process on impedance spectra was revealed along with the experimental results.

Non-ideal impedance spectra influenced by the distribution of electrical properties, such as electrical conductivity and permittivity, of the coating were studied. The distribution of the inter-correlated parameters on the impedance model described the physical meaning of the non-ideal impedance, represented by the combination of local segments, which resulted in distorted spectra of a bulk system.

Since the locally distributed parameters could represent the local electrical or electrochemical behavior, it was possible to evaluate localized impedance spectra. Thus, the modified two-dimensional impedance model based on charge conservation was suggested to understand the localized electrochemical impedance spectra (LEIS) responding the local defects. The modified model revealed the influence of electrical conductivity of electrolyte on the resolution of LEIS for local defects.

Lastly, non-conventional impedance responses of a zinc-rich coating system were observed in electrical and electrochemical impedance measurements previously considered to have no effect on the system. Non-electrolytic and electrochemical cells on zinc-rich coatings were analyzed to understand the intrinsic response of the coatings with electrical active and passive analogs under electrical and electrochemical cyclic tests. The aforementioned studies will not only be used as a method to interpret the various physical meanings of systems, such as black boxes, through impedance spectra, but also as an important guideline for optimal design of coating materials.

DEDICATION

To my beloved family for encouraging me and supporting me as always.

ACKNOWLEDGEMENTS

First of all, I would like to acknowledge my committee chair; Dr. Homero Castaneda for his dedicated help, guidance, and encouragement. I would also like to thank my committee members; Dr. Hung-Jue Sue, Dr. Sarbajit Banerjee, and Dr. Ankit Srivastava for their valuable suggestion and support to my research. I am also grateful to National Corrosion and Materials Reliability Center members for their precious time for discussion in my study and research.

I really thank my parents and my wife for believing and praying until the end during many unexpected long processes. I would also like to thank my lovely sons, Haim and Ireh, for being my joy in various situations.

I would like to express my sincere appreciation to all those who did not mention anything on the paper, but who supported and encouraged me.

Finally, there are still some shortcomings in this research, but I think this is also a step forward. This process was such a daunting experience for me, but I thank my God for not giving up and always being with me. Moreover, I would like to once again give glory to my living God who will walk with me in the future.

CONTRIBUTORS AND FUNDING SOURCES

Contributors

This work was supervised by a dissertation committee consisting of Professor Homero Castaneda [advisor], Professor Hung-Jue Sue, and Professor Ankit Srivastava of the Department of Materials Science and Engineering and Professor Sarbajit Banerjee of the Department of chemistry.

The experimental data analyzed for Chapter 2 was provide by Professor Homero Castaneda. The experimental analysis depicted in Chapter 2 were conducted in part by Yenny Cubides of the Department of Materials Science and Engineering and were published in 2017. The XRD results depicted in Chapter 5 and 6 were conducted in part by Tse-Ming Chiu of the Department of Materials Science and Engineering and were published in 2019.

All other work conducted for the dissertation was completed by the student independently.

Funding Sources

Graduate study was made possible in part by the funding sources including Department of Defense Office of Corrosion Policy and Oversight under Grant Number M1503199, Hyundai Motor Co. under Grant Number M1700936, Shell Exploration and Production Co. under Grant Number M1802804, Baker Hughes Co. under Grant Number M1800783, Hyundai Steel Co. under Grant Number M1802824, AZZ Inc.

under Grant Number M1901844. Its contents are solely the responsibility of the authors and do not necessarily represent the official views.

NOMENCLATURE

Acronyms

AC	Alternating current
CCC	Chromium conversion coating
CDF	Cumulative distribution function
CE	Counter electrode
CNTs	Carbon nanotubes
CPE	Constant phase element
CV	Coefficient of variation
DC	Direct current
EEC	Equivalent electrical circuit
EIS	Electrochemical impedance spectroscopy
IHP	Inner Helmholtz plane
IMC	Intermetallic compound phases
LEIS	Localized electrochemical impedance spectra
LST	Linear systems theory
OCP	Open circuit potential
OHP	Outer Helmholtz plane
PDF	Probability density function
RE	Reference electrode
SCE	Saturated calomel electrode

TLM	Transmission line modeling
WE	Working electrode
XRD	X-ray powder diffraction
ZRP	Zinc-rich primer

Symbols

Section 1

$Z(s)$	Laplace transform of impedance
$\bar{V}(s)$	Laplace transform of voltage
$\bar{I}(s)$	Laplace transform of electrical current
V_A	Amplitude of alternating voltage
I_A	Amplitude of alternating electrical current
φ	Phase shift between electrical current and voltage
$V(t)$	monochromatic sinusoidal voltage
ω	Angular frequency
t	Time
Z	Impedance
Z'	Real part of impedance
Z''	Imaginary part of impedance
$\|Z(\omega)\|$	Magnitude of impedance
τ	Time constant
$\mathcal{L}$	Laplace transform

R	Resistance
C	Capacitance
Ox	Oxidant
n	Number of electrons transferred
Rx	Reductant
C_d	Double-layer capacitor
R_{ct}	Charge transfer resistance
R_p	Polarization resistance
Z_w	Diffusion impedance
R_s	Solution resistance
Z_{CPE}	Impedance of CPE
Q_{CPE}	CPE parameter
α_{CPE}	CPE exponent
f	Frequency of the signal

Section 2

$R_{(j,i)}$	Resistance of (j,i) element at each direction
$C_{(j,i)}$	Capacitance of (j,i) element at each direction
ρ	Resistivity
ε	Dielectric constant
ε_0	Permittivity of free space
subscript x	x-direction
subscript z	z-direction

$Z_{(j,i\leftrightarrow j,i+1)}$	Localized impedance at the interface between the (j,i) and the (j,i+1) elements
$Z_{(j,i\leftrightarrow j+1,i)}$	Localized impedance at the interface between the (j,i) and the (j+1,i) elements
ω	Perturbation angular frequency
α	Empirical exponent of the CPE
C_{dl}	Capacitance of the double layer
$R_{ct,int}$	Charge transfer impedance
$Z_{diff,int}$	Diffusion impedance
σ	Warburg coefficient
D	Diffusion coefficient
δ	Thickness of the diffusion layer
i	Electrical current of a closed path
l_x	Length of the system in x-direction
P	Log-normal probability density function
M	Mean of maximum percolation lengths of the electrolyte
V	Variance of maximum electrolyte percolation lengths
σ_p	Standard deviation of the variable’s natural logarithm
μ_p	Mean of the variable’s natural logarithm

Section 3

U	m-dimensional uncorrelated standard normal random vector

ρ_0	Positive definite correlation matrix
Y	Correlated standard normal variables
$\Sigma_\mathrm{Y}/\sigma_Y^2$	Correlation matrix of Y
Σ_U	Covariance matrix of U
F_X	Joint distribution of a m-dimensional random vector X
C	Copula function
X	Correlated design variables
ϕ	Normal PDF
$f_{X_i}(x_i)$	Marginal PDF of X_i
ρ'_{12}	Reduced correlation coefficient between X_1 and X_2
ρ_{12}	Input correlation coefficient between the correlated standard normal variables Y_1 and Y_2
N	Normal distribution
LN	Log-normal distribution
cv	Correlation coefficient
μ	Mean value
ε	Permittivity
σ	Electrical conductivity
subscript *x*	*x*-direction
subscript *z*	*z*-direction
$Z_{(j,i\leftrightarrow j,i+1)}$	Localized impedance at the cell interface between the (j,i) element and the $(j,i+1)$ element

$Z_{(j,i\leftrightarrow j+1,i)}$	Localized impedance at the cell interface between the (j,i) element and the $(j+1,i)$ element
$i_{j,i}$	Electrical current density of the (j,i) loop
l_x	System length in the x-direction
R_{eq}	Equivalent value of electrical resistance
C_{eq}	Equivalent values of capacitance
A	Measurement area for normalization
$l_{thickness}$	Thickness of the designed coating
2a	Maximum length in the x-real axis direction
b	Maximum length in the y-impedance axis direction

Section 4

ρ_s	Electrical resistivity of electrolyte solution
ρ_c	Electrical resistivity of coating
ρ_m	Electrical resistivity of metal substrate
ε_s	Permittivity of electrolyte solution
ε_c	Permittivity of coating
ε_m	Permittivity of metal substrate
C_d	Double-layer capacitor
R_{ct}	Charge transfer resistance
subscripts x	x-direction
subscripts z	z-direction
C	Capacitance

R	Resistance
$Z_{(j,i\leftrightarrow j,i+1)}$	Localized impedance at the cell interface between the (j,i) element and the $(j,i+1)$ element
$Z_{(j,i\leftrightarrow j+1,i)}$	Localized impedance at the cell interface between the (j,i) element and the $(j+1,i)$ element
ω	Angular frequency
i	Electrical current density
V	Relative potential at each node
l_e	Coating length exposed by electrolyte in x-direction
i_0	Input current density
Z_{total}	Total impedance on 2D domain

Section 5

R_f	Resistance of the ZRP film
Q_f	CPE of the ZRP film
R_Ω	Ohmic resistance of cables
j	Current density through an oxide system/metal interface with single diode-like behavior
V_a	Applied voltage powered by the electrochemical analysis machine
ΔV	Voltage drop
q	Elementary charge
k_B	Boltzmann constant

T	Absolute temperature
n	Ideality factor
m^*	Charge carrier effective mass
h	Planck’s constant
Φ_B	Schottky barrier height at the metal/semiconductor interface in volts.

Section 6

R_f	Resistance of the ZRP film
Q_f	CPE of the ZRP film
R_{ct}	Charge transfer resistance
Q_{dl}	CPE for a double layer capacitor
R_e	Electrolyte resistance
$Z_{w\delta}$	Bounded Warburg impedance
Q_{0i}	Constant of CPE
τ_d	Characteristic diffusion time
$R_d/\sqrt{\tau_d}$	Warburg coefficient
$E_1(t)$	OCP for natural degrdation druing cathodic protection periode
t	Immersion time
α_a	Anodic electron transfer coefficient
α_c	Cathodic electron transfer coefficient
E_a^0	Anodic formal potential

E_c^0	Cathodic formal potential
n_a	The number of electrons transferred from anodic reaction
n_c	The number of electrons transferred from cathodic reaction
k_a	Anodic reaction rate constant
k_c	Cathodic reaction rate constant
$[Ox]$	Bulk concentration of the oxidation state of the oxidizer in the electrolyte
z_c	Charge of the oxidation
ϕ_2	Potential at the outer Helmholtz plane
t_c	Initial time for the cathodic protection curve
τ_1	Characteristic time of the degradation on the cathodic protection of the ZRP film
A_1	OCP at t_c
B_1	Increasing potential coefficient for cathodic protection
t_0	First sequence time of electrochemical conditioning test
a_0	Initial OCP at t_0
E_2	OCP due to the charging effect of capacitive behavior
τ_2	Characteristic time of the capacitive charging effect of the ZRP film
B_2	Decreasing potential coefficient for charging
E_{OCP}	Local OCP change on the cyclic conditioning tests

$\lvert Z \rvert_s$	Impedance magnitude of the peak point of the high-frequency capacitive loop at a specific immersion day after full saturation with the electrolyte
$\lvert Z \rvert_{ss}$	Impedance magnitude of the peak point of the high-frequency capacitive loop on the day of full saturation

TABLE OF CONTENTS

Page

LIST OF FIGURES

LIST OF TABLES

Page

1. INTRODUCTION

1.1. Impedance Spectroscopy

Impedance spectroscopy has been used as a powerful tool to solve various electric- and electrochemistry- related problems, which invests transport and dielectric properties of materials [1], measures passive surfaces [2, 3], investigates the properties of organic coatings [4-6], intercalation electrodes [7-9], and characterizes the corrosion process [10-12]. The results obtained from the powerful method, used as a linear technique, are interpreted by Linear Systems Theory (LST) [13]. For use as a linear technique, the amplitude of an alternating excitation signal smaller than 10mV rms is normally proposed for the analysis of electrochemical system [14], as shown in Fig. 1.1. The important constraints of LST on impedance are that the response of the system is represented by linear (differential) equations, the system must be stable and does not generate a response before the perturbation is applied, and the impedance must be finite [15]. The constraint on linear response makes the superposition principle which can be defined by additive property and homogeneous property applicable [16]. Since it is necessary to separate and analyze various overlapping physical processes from this superposition principle, an appropriate transfer function characterizing a constant-parameter linear system must be defined. The transfer function of a linear system, which is independent of excitation amplitude, is the ratio of the Laplace transform of the output functions to the Laplace transform of the input functions. Heaviside, the father of impedance spectroscopy, defined the term of “impedance” as

$$\boldsymbol{Z(s)} = \frac{\boldsymbol{\overline{V}(s)}}{\boldsymbol{\overline{I}(s)}} \tag{1.1}$$

where $\overline{V}(s)$ is the Laplace transform of the voltage and $\overline{I}(s)$ is the Laplace transform of the current [17].

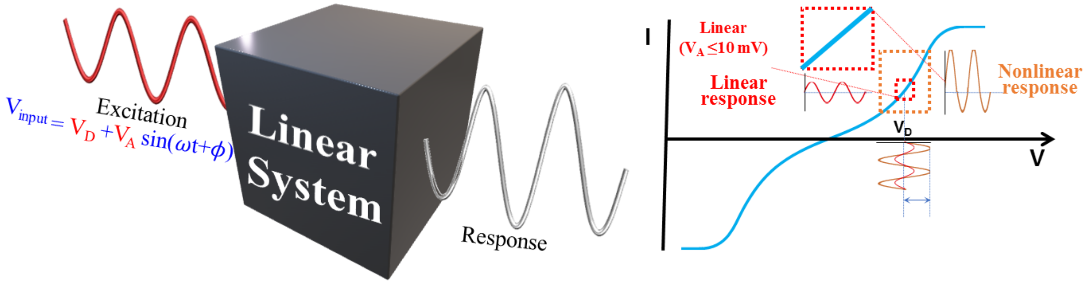

Figure 1.1 Linear and nonlinear response of the system.

If a monochromatic sinusoidal voltage $V(t) = V_A \sin(\omega t)$ is applied to an electrochemical system, then the responding current is $I(t) = I_A \sin(\omega t - \varphi)$. V_A and I_A denote the amplitude of alternating voltage and the electrical current, respectively, and φ is the phase shift between the current and voltage. Then the impedance can be also defined as [18]

$$\boldsymbol{Z} = V(t)/I(t) = |Z(\omega)|e^{j\varphi} = Z' + jZ'' \tag{1.2}$$

where the real and imaginary part of impedance are Z' and Z'', respectively. The magnitude of impedance ($|Z(\omega)|$), which depends on the angular frequency, can be expressed as follows.

$$|Z(\omega)| = \sqrt{(Z')^2 + (Z'')^2} \tag{1.3}$$

The phase shift (φ) as a quality factor can be calculated:

$$\varphi(\omega) = \arctan\,(Z''/Z') \tag{1.4}$$

The impedance as a transfer function enables complex numbers in the frequency domain to be represented in Nyquist domain by plotting Z''as a function of Z'. Nyquist plot can represent the vector response of electrical and electrochemical feedback systems. If a system is considered as a first order transfer function with one time constant (τ), the system can be written as

$$Z(\omega) = \frac{a}{1 + j\omega\tau} = \frac{a}{1 + \omega^2\tau^2}(1 - j\omega\tau) \tag{1.5}$$

The Nyquist image for the system provides a semi-circle going from the origin when angular frequency is in infinity and finishing the (a,0) point when zero angular frequency as described in Fig. 1.2.

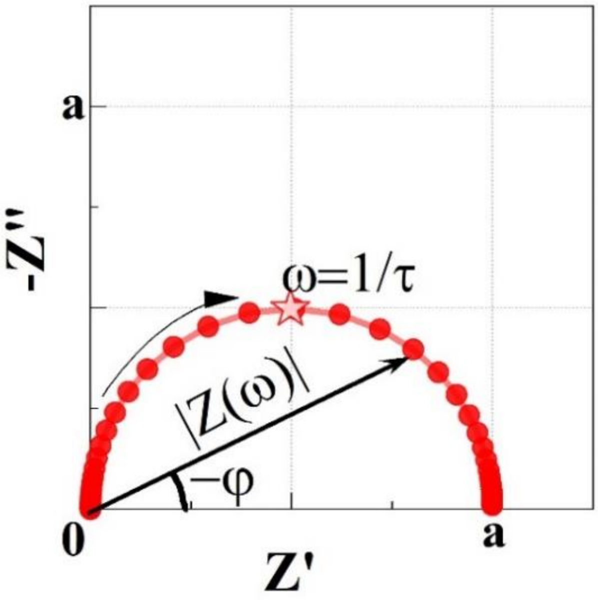

Figure 1.2 Nyquist diagram of the system with first order transfer function and one time constant.

1.2. Operation Calculus in Electrical and Electrochemical System

The electrical system is represented by a series/parallel combination of electrical elements, such as electrical resistors, capacitor, and inductors. For example, the electrical resistance measuring the reverse of the electric current flow is expressed by Laplace transform (by taking $s = j\omega$) [19]:

$$\boldsymbol{\mathcal{L}}\big(\boldsymbol{V(t)}\big) = \boldsymbol{\mathcal{L}}\big(\boldsymbol{RI(t)}\big) \Leftrightarrow \boldsymbol{Z(\omega)} = \frac{\boldsymbol{\bar{V}(\omega)}}{\boldsymbol{\bar{I}(\omega)}} = R \tag{1.6}$$

In a capacitor, the change in charge of the capacitor is proportional to the potential difference between each terminal, and the change in charge over time is defined as the electric current. The impedance for the capacitor is represented by conducting Laplace transform:

$$\boldsymbol{\mathcal{L}}\big(\boldsymbol{I(t)}\big) = \boldsymbol{\mathcal{L}}\left(\frac{\boldsymbol{CdV(t)}}{\boldsymbol{dt}}\right) \Leftrightarrow \boldsymbol{Z(\omega)} = \frac{\boldsymbol{\bar{V}(\omega)}}{\boldsymbol{\bar{I}(\omega)}} = \frac{1}{j\omega C} \tag{1.7}$$

Using the representation of these basic electrical elements, the impedance of the electrical system can be calculated in a circuit consisting of a series-parallel combination of the electrical elements. By applying Kirchhoff's laws, the integro-differential equation in each loop is solved as shown in Fig. 1.3. As shown in Fig. 1.3(a), a straight line parallel to y-imaginary axis in the Nyquist plot can be seen in RC series circuit, and the imaginary value of the impedance increases from zero to infinity by decreasing the angular frequency. For RC parallel circuit in Fig. 1.3(b), the impedance signal shows a perfect semicircle in the Nyquist image. As the angular frequency value decreases from infinity to zero, the impedance converges from the origin to the resistance R value of the real axis. In the case of RC series-parallel combination circuit as shown in Fig. 1.3(c), the similar perfect semi-circle of impedance spectra in the Nyquist plot as shown in Fig. 1.3(b) is observed, but the shift of the overall signal is occurred in the direction of the real axis due to the external resistance in Rs.

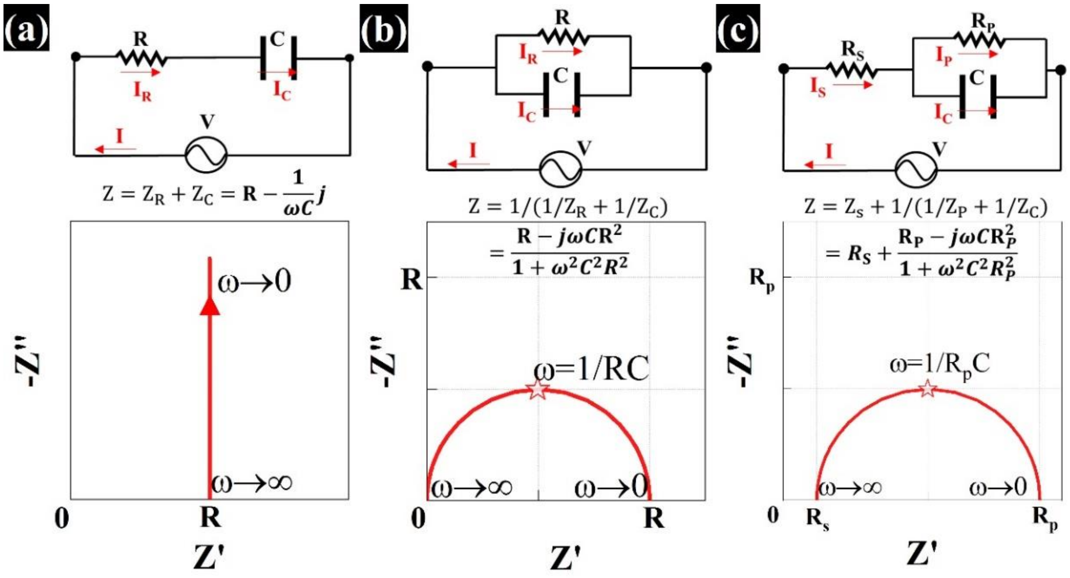

Figure 1.3 Simple electrical systems and Nyquist images: (a) RC series circuit. (b) RC parallel circuit. (c) RC series-parallel circuit.

Electrochemical system always involves an electrochemical reaction at an electrified interface [20].

$$O + ne^- \rightarrow R \tag{1.8}$$

In this equation, *O* is the oxidant, *n* is the number of electrons transferred, and *R* is its reductant. Electrons are transferred across the interface as shown in Fig. 1.4, and the charge transfer results in both non-faradaic and faradaic components.

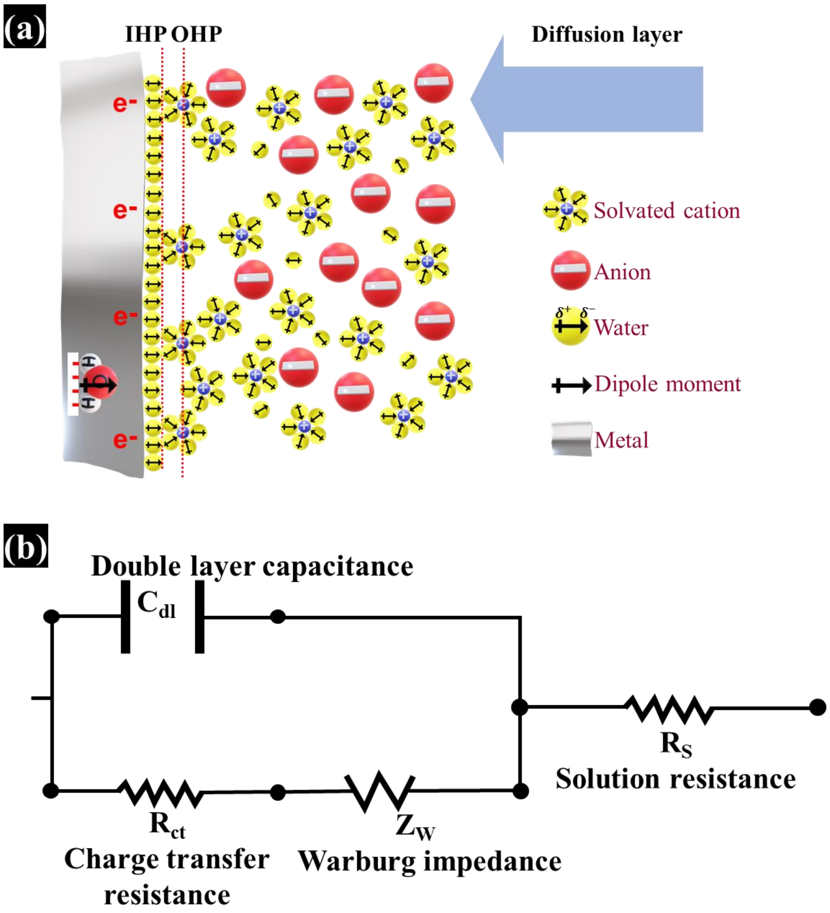

Figure 1.4 Electrochemical System: (a) An electrified interface. (b) An idealized Randles electrical equivalent circuit.

The non-faradaic component occurs at the formation of double-layer capacitor (C_d) induced by charged metal surface. The charging of double-layer capacitor leads non-faradaic current. The faradaic component is due to the electron transfer from the electrified interface through the reaction by exceeding the appropriate activation barrier. If the potential to overcome the activation barrier is in the open circuit condition, the faradaic component is called charge transfer resistance (R_{ct}), and if the potential is applied in any polarized condition, the component is called polarization resistance (R_p). The mass transports of reactant and product, which determine the electron transfer rate at the interface by consuming oxidant and producing reductant, provide diffusion impedance (Z_w), another representation of impedance. R_s is solution resistance. The electrical equivalent circuit of this simple electrochemical system was proposed by Randles as shown in Fig. 1.4(b) [21]. The Randles circuit is commonly known and used to interpret various electrochemistry systems. The complex expression of the Randles circuit is calculated as

$$
\begin{aligned}
Z(\omega) = R_s &+ \frac{R_p + \sigma\omega^{-\frac{1}{2}}}{\left(C_d\sigma\omega^{\frac{1}{2}} + 1\right)^2 + \omega^2 C_d^2\left(R_p + \sigma\omega^{-\frac{1}{2}}\right)^2} \\
&+ j\frac{\left[\omega C_d\left(R_p + \sigma\omega^{-\frac{1}{2}}\right)^2 + \sigma\omega^{-\frac{1}{2}}\left(C_d\sigma\omega^{\frac{1}{2}} + 1\right)\right]}{\left(C_d\sigma\omega^{\frac{1}{2}} + 1\right)^2 + \omega^2 C_d^2\left(R_p + \sigma\omega^{-\frac{1}{2}}\right)^2}
\end{aligned}
\tag{1.9}
$$

1.3. Models and Analogs

Electrochemical impedance spectroscopy (EIS) has been considered as a reliable technique to analyze the characteristics of the electrochemical system [8, 22]. The EIS with a small excitation under steady-state conditions can provide not only electrical information of a bulk system but also detailed electrochemical properties of the interfacial reactions [23]. It is easy to obtain impedance results from experimental measurements, but, the interpretation of the measured results has been considered not to be easy. If the characteristic impedance diagram shows an unusual appearance, the interpretation becomes more difficult [24].

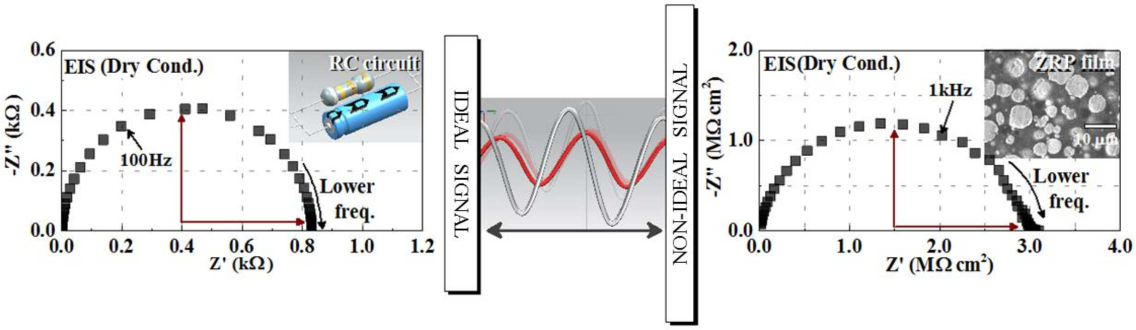

Figure 1.5 Impedance responses of ideal system (RC electrical circuit) and real coating material (ZRP film).

Equivalent electrical circuits have been considered as a viable option to analyze the EIS data by associating bulk system and interfacial processes with electrical analogs [25, 26]. However, one of the critical weaknesses of this equivalent electrical circuit approach arises from the method of selecting the corresponding analytical approach, which provides a physical interpretation of electrochemical system with quantitative parameters. In addition, interpreting the response of an EIS using ideal electrical circuit elements including resistors and capacitors to extract equivalent physicochemical properties of an electrochemical system revealed its limitations [27]. As can be seen in Fig. 1.5, the impedance response in most real material systems has skewed phenomena in impedance spectra, unlike in ideal case. Although the use of ideal electrical circuit elements allowed meaningful interpretation of the experimental results by fitting, most of the cases of fitting contained a large error. Thus, constant phase element (CPE) has been proposed as a method to approximate the experimental results of the characteristic impedance diagram showing a non-ideal shape like a distorted semicircle in Nyquist plot, which is expressed as [28, 29]:

$$Z_{CPE} = \frac{1}{Q_{CPE}(i\omega)^{\alpha_{CPE}}} \tag{1}$$

where Q_{CPE} (F $\mathrm{cm}^{-2} s^{\alpha_{CPE}-1}$) and α_{CPE} are the CPE parameter and exponent, respectively. ω is the angular frequency represented by the expression $2\pi f$ where f is the frequency in hertz. If α_{CPE} is one, CPE is pure capacitor, and if zero, CPE represents pure resistor. Although the fitting quality has been greatly improved through the CPEs over a wide range of experimental results, the physical meaning of impedance spectra has still not fully understood [27]. For a better understanding of the non-ideal response of the impedance spectra, represented by distorted semicircle in a Nyquist domain, the models equipped with physical description and better fitting of the distortion have been suggested. Several potential properties, such as surface roughness [30, 31], porous electrodes [32], and adsorbed intermediates [33] have been reported for such CPE behavior. Models based on the distributions of physical properties in one-dimension also have been proposed to understand the non-ideal impedance spectra of various systems including polymer coating by the distributions of dielectric constant [34], electrical resistivity [35-37], and surface reactivity [38] which attributed to the distributions of time constants.

One-dimensional transmission line modeling has been also widely used to explore the degradation of metal-rich primers or coatings, passive surface, and porous electrodes by partitioning electrochemical interface into the sub-elements with defined scale [39-43]. A one-dimensional transmission line modeling approach is able to explain the relationship between the driving potential, resistance, and corrosion rate of an electrochemical system based on the electrical balance of the electrical circuit network [15]. However, there is still limitation for this approach to consider the effect of localized pore distribution of coating layers on the impedance spectra of the electrochemical system.

1.4. Motivation and Objectives

Impedance spectra have been analyzed to extract various information from coating systems, such as black boxes, but they are still not completely understood. The simple EEC model, the one-dimensional transmission line model, and the one-dimensional electrical elemental distributions including the Voigt measurement model, mentioned above, have limitations in interpreting the physical meaning of superimposed impedance signals. In this study, the author focuses on describing the methodology for analyzing the impedance spectra that simultaneously implies a variety of physical meanings. In particular, theoretical and experimental approaches to interpret impedance spectra that are not ideal or is not conventional will be presented.

In order to understand the response of impedance spectra on physical distribution, it is necessary to analyze in higher dimensions rather than in one-dimension. In this study, author first constructs a two-dimensional impedance model to understand the property distribution effects in space. The various non-ideal impedance spectra are then analyzed using the constructed two-dimensional impedance model. The non-ideal impedance spectra are characterized through local defect by a scratch and distribution of various physicochemical properties.

In addition, it has been taken for granted that the non-destructive techniques do not change the coating materials where the assessment is taken and the future trend of calendrical aging. This belief prevents researchers from considering the direct response of the impedance to the inherent physical properties of the system. However, non-conventional impedance responses are observed in electrical/electrochemical impedance measurements previously considered not to affect the coating system. Thus, the objective of this study is to understand the non-conventional electrical and electrochemical impedance spectra of coated materials which were susceptible to the transfer function signal due to the distribution of certain substances. The outcome of this research is to understand the inside of coating design through impedance spectra and will be an important first step in presenting the direction to the new design.

1.5. References

[1] D. Macdonald, Transient techniques in electrochemistry, Springer Science & Business Media, 2012.

[2] L. Hamadou, A. Kadri, N. Benbrahim, Characterisation of passive films formed on low carbon steel in borate buffer solution (pH 9.2) by electrochemical impedance spectroscopy, Applied Surface Science, 252 (2005) 1510-1519.

[3] J. Pan, D. Thierry, C. Leygraf, Electrochemical impedance spectroscopy study of the passive oxide film on titanium for implant application, Electrochimica Acta, 41 (1996) 1143-1153.

[4] P. Bonora, F. Deflorian, L. Fedrizzi, Electrochemical impedance spectroscopy as a tool for investigating underpaint corrosion, Electrochimica Acta, 41 (1996) 1073-1082.

[5] A.S. Nguyen, N. Causse, M. Musiani, M.E. Orazem, N. Pébère, B. Tribollet, V. Vivier, Determination of water uptake in organic coatings deposited on 2024 aluminium alloy: Comparison between impedance measurements and gravimetry, Progress in Organic Coatings, 112 (2017) 93-100.

[6] F. Mansfeld, Use of electrochemical impedance spectroscopy for the study of corrosion protection by polymer coatings, Journal of Applied Electrochemistry, 25 (1995) 187-202.

[7] A. Metrot, A. Harrach, Electrochemical impedance spectroscopy of intercalated electrodes, Electrochimica Acta, 38 (1993) 2005-2009.

[8] S. Cho, C.-F. Chen, P.P. Mukherjee, Influence of microstructure on impedance response in intercalation electrodes, Journal of the Electrochemical Society, 162 (2015) A1202-A1214.

[9] M. Levi, D. Aurbach, Impedance of a single intercalation particle and of non-homogeneous, multilayered porous composite electrodes for Li-ion batteries, The Journal of Physical Chemistry B, 108 (2004) 11693-11703.

[10] F. Mansfeld, Electrochemical impedance spectroscopy (EIS) as a new tool for investigating methods of corrosion protection, Electrochimica Acta, 35 (1990) 1533-1544.

[11] D. Ribeiro, J. Abrantes, Application of electrochemical impedance spectroscopy (EIS) to monitor the corrosion of reinforced concrete: a new approach, Construction and Building Materials, 111 (2016) 98-104.

[12] V. Encinas-Sánchez, M. de Miguel, M. Lasanta, G. García-Martín, F. Pérez, Electrochemical impedance spectroscopy (EIS): An efficient technique for monitoring corrosion processes in molten salt environments in CSP applications, Solar Energy Materials and Solar Cells, 191 (2019) 157-163.

[13] D.D. Macdonald, M.C. McKubre, Impedance measurements in electrochemical systems, Modern Aspects of Electrochemistry, Springer, (1982) 61-150.

[14] B. Hirschorn, I. Ibrahim, M.E. Orazem, H. Takenouti, B. Tribollet, Effect of large perturbation amplitudes on the impedance response of an electrochemical system, ECS Transactions, 13 (2008) 81.

[15] D.D. Macdonald, Reflections on the history of electrochemical impedance spectroscopy, Electrochimica Acta, 51 (2006) 1376-1388.

[16] J.S. Bendat, A.G. Piersol, Random data: analysis and measurement procedures, John Wiley & Sons, 2011.

[17] S. Goldman, Transformation calculus and electrical transients, Prentice-Hall, 1949.

[18] F. Scholz, Electroanalytical methods, Springer, 2010.

[19] H.H. Girault, Analytical and physical electrochemistry, EPFL press, 2004.

[20] B.-Y. Chang, S.-M. Park, Electrochemical impedance spectroscopy, Annual Review of Analytical Chemistry, 3 (2010) 207-229.

[21] J.E.B. Randles, Kinetics of rapid electrode reactions, Discussions of the Faraday Society, 1 (1947) 11-19.

[22] C. Kim, A.I. Karayan, J. Milla, M.M. Hassan, H. Castaneda, A smart coating embedded with pH-responsive nanocapsules containing a corrosion inhibiting agent, ACS Applied Materials & Interfaces, 12 (2020) 6451-6459.

[23] X. Liu, J. Xiong, Y. Lv, Y. Zuo, Study on corrosion electrochemical behavior of several different coating systems by EIS, Progress in Organic Coatings, 64 (2009) 497-503.

[24] D. Klotz, Negative capacitance or inductive loop?–A general assessment of a common low frequency impedance feature, Electrochemistry Communications, 98 (2019) 58-62.

[25] P. Campestrini, E.P.M. van Westing, J.H.W. de Wit, Influence of surface preparation on performance of chromate conversion coatings on Alclad 2024 aluminium alloy Part II: EIS investigation, Electrochimica Acta, 46 (2001) 2631-2647.

[26] D. Chidambaram, C.R. Clayton, M.W. Kendig, G.P. Halada, Surface pretreatments of aluminum alloy AA2024-T3 and formation of chromate conversion coatings - II. Composition and electrochemical behavior of the chromate conversion coating, Journal of the Electrochemical Society, 151 (2004) B613-B620.

[27] F. Mahdavi, M.Y. Tan, M. Forsyth, Electrochemical impedance spectroscopy as a tool to measure cathodic disbondment on coated steel surfaces: Capabilities and limitations, Progress in Organic Coatings, 88 (2015) 23-31.

[28] M.E. Orazem, B. Tribollet, Electrochemical impedance spectroscopy, John Wiley & Sons, 2017.

[29] E. Barsoukov, J.R. Macdonald, Impedance spectroscopy: theory, experiment, and applications, John Wiley & Sons, 2018.

[30] Z. Kerner, T. Pajkossy, Impedance of rough capacitive electrodes: the role of surface disorder, Journal of Electroanalytical Chemistry, 448 (1998) 139-142.

[31] C.L. Alexander, B. Tribollet, M.E. Orazem, Contribution of surface distributions to constant-phase-element (CPE) behavior: 1. Influence of roughness, Electrochimica Acta, 173 (2015) 416-424.

[32] H.-K. Song, H.-Y. Hwang, K.-H. Lee, L.H. Dao, The effect of pore size distribution on the frequency dispersion of porous electrodes, Electrochimica Acta, 45 (2000) 2241-2257.

[33] C.L. Alexander, B. Tribollet, V. Vivier, M.E. Orazem, Contribution of surface distributions to constant-phase-element (CPE) behavior: 3. Adsorbed intermediates, Electrochimica Acta, 251 (2017) 99-108.

[34] M. Musiani, M.E. Orazem, N. Pébère, B. Tribollet, V. Vivier, Constant-phase-element behavior caused by coupled resistivity and permittivity distributions in films, Journal of the Electrochemical Society, 158 (2011) C424-C428.

[35] B. Hirschorn, M.E. Orazem, B. Tribollet, V. Vivier, I. Frateur, M. Musiani, Constant-phase-element behavior caused by resistivity distributions in films I. Theory, Journal of the Electrochemical Society, 157 (2010) C452-C457.

[36] P. Córdoba-Torres, Relationship between constant-phase element (CPE) parameters and physical properties of films with a distributed resistivity, Electrochimica Acta, 225 (2017) 592-604.

[37] A.S. Nguyen, M. Musiani, M.E. Orazem, N. Pébère, B. Tribollet, V. Vivier, Impedance analysis of the distributed resistivity of coatings in dry and wet conditions, Electrochimica Acta, 179 (2015) 452-459.

[38] J. Li, K. Schuler, S.E. Creager, A Generalized equivalent-circuit model for electroactive monolayers exhibiting a fixed redox potential and a distribution of electron-transfer rate constants I. Square distributions, Journal of the Electrochemical Society, 147 (2000) 4584-4588.

[39] I.D. Raistrick, Impedance studies of porous-electrodes, Electrochimica Acta, 35 (1990) 1579-1586.

[40] K.N. Allahar, D. Battocchi, G.P. Bierwagen, D.E. Tallman, Transmission line modeling of EIS data for a Mg-rich primer on AA 2024-T3, Journal of the Electrochemical Society, 157 (2010) C95-C101.

[41] J. Niu, J.I. Barraza-Fierro, H. Castaneda, Quantification of protective properties of the coating/corrosion product/steel interface by integration of transmission line model with EIS results, Journal of Coatings Technology and Research, 12 (2015) 393-405.

[42] S.G. Real, A.C. Elias, J.R. Vilche, C.A. Gervasi, A. Di Sarli, An electrochemical impedance spectroscopy study of zinc rich paints on steels in artificial sea water by a transmission line model, Electrochimica Acta, 38 (1993) 2029-2035.

[43] H. Marchebois, C. Savall, J. Bernard, S. Touzain, Electrochemical behavior of zinc-rich powder coatings in artificial sea water, Electrochimica Acta, 49 (2004) 2945-2954.

2. DETERMINISTIC-PROBABILISTIC TWO-DIMENSIONAL GLOBAL IMPEDANCE MODEL[*]

In this chapter, 2D impedance model will be discussed by probing the degradation mechanism of a Cr(VI) coating/aluminum alloy 2024-T3 system. Electrochemical impedance spectroscopy (EIS) has been experimentally used to characterize the degradation mechanisms of a multilayered Cr(VI) coating/aluminum alloy 2024-T3 substrate system in 3.5% NaCl solution at low pH. A 2D damage evolution model is proposed to understand the influence of defined elements into the multilayered coating/substrate degradation process. The model was developed assuming steady state conditions, while discretization of the model included multilayered stacks, such as a topcoat, a primer, and a chromate conversion layer as a pretreatment on an aluminum substrate. The modeling technique was deterministic-stochastic in nature. The deterministic approach was based on a transmission line model that was developed to represent the local impedance for small segments of the system to characterize physicochemical properties inherent to the organic coatings and the transport mechanisms. The randomly generated structures including coating pore distributions are illustrated by stochastic modeling with probability density functions. The quantitative understanding of the degradation mechanism from this 2D model is achieved, and the

---

[*] Reprinted with permission from “Probing the degradation mechanism of a Cr(VI) coating/aluminum alloy 2024-T3 system based on dynamic mechanisms and a 2D deterministic-probabilistic approach” by Seongkoo Cho, Yenny Cubides, Homero Castaneda, 2017. *Electrochimica Acta*, 236, 82-96, Copyright © 2017 by Elsevier Ltd.

2D analysis shows consistent results with experimental conditions over various immersion times. The degradation mechanism for the multilayered coating system at low pH can be described as follows: intact condition, electrolyte uptake, lixiviation of Cr(VI) ions/diffusion, and self-healing process that provide repassivation of the Cr(III) oxide layer.

2.1. Introduction

Aluminum alloy 2024-T3 (AA2024-T3) is commonly used in aeronautical applications [1, 2]. It contains intermetallic compound phases (IMC) containing Cu, Mg, or Fe that provide excellent strength and fatigue resistance [3]. Nevertheless, the presence of IMC phases in aluminum substrates reduce the corrosion resistance of the material due to creation of galvanic couples between the different IMC phases and the AA2024-T3 matrix, which leads to localized corrosion and stress corrosion cracking, especially in the presence of chloride ions [4-6].

Organic and composite coatings have been proposed in order to control or mitigate the corrosion processes in aluminum alloys. Cr(VI) coating is a conventional aircraft coating composed of a chromate conversion layer, primer, and topcoat. The chromium conversion coating (CCC) acts as a corrosion protection layer as well as an adhesion promoter between the aluminum substrate and the primer. It has been reported that CCC provides the following benefits: 1) self-healing protection, 2) barrier protection due to the presence of a hydrophobic Cr(III) oxide layer, and 3) inhibition of the oxygen reduction reaction at the aluminum substrate [7, 8]. The primer usually corresponds to an epoxy polyamide coating containing chromate pigments (such as strontium chromate (SrCrO4)) in order to provide active corrosion inhibition to the metallic substrate, in combination with other compounds such as fillers that can enhance the barrier properties of the epoxy coating and additives such as coloring agents [9, 10]. The strontium chromate has low solubility in water; thus, when there is a damage in the coating, the dissolved Cr(VI) ions migrate to the affected area and inhibit additional deterioration of the metal surface. [10, 11]. Kendig et al. [7] reported that the corrosion inhibition afforded by $SrCrO_4$ was related to the following: 1) passivation of active intermetallic phases by the Cr(VI) ions, 2) electrochemical reactions between Cr(VI) ions and the aluminum substrate that inhibit cathodic reactions, such as oxygen reduction reaction and hydrogen evolution reaction, and 3) decrease in the zeta potential of the aluminum substrate by the presence of Cr(VI) ions leading to repulsion of aggressive ionic species, such as chloride ions. In addition, due to the low solubility of Cr(VI) ions, the epoxy coating can provide long-term protection since there is a good balance between ionic transportation for active inhibition and loss of Cr(VI) ions in the binder that increases the porosity of the primer and therefore the permeability of electrolyte. Finally, the topcoat is a polyurethane coating that confers excellent flexibility, UV protection, and chemical resistance to the multilayer system.

Despite of the excellent corrosion resistance of this multilayer system, there is great concern about the toxicity of Cr(VI) ions [7, 12]. Therefore, numerous studies have proposed alternatives to Cr(VI) chromium coatings [13-16]. The corrosion protection mechanisms of chromated coatings can lead to understanding the performance with time and serve as the benchmark for new, chromate-free coating developments. Damage evolution modeling of this coating can be approached by deterministic-probabilistic fundamentals, which represents a new direction in the assessment of corrosion control since several chromate-free coating systems attempt to mimic the inhibition properties of the Cr(VI) ions [9, 17-19].

Electrochemical impedance spectroscopy (EIS) is a non-destructive technique used to characterize the electrochemical performance of corrosion protection coatings [12, 20]. It is a reliable technique because it can provide detailed electrochemical information of the interfacial reactions with a small excitation permitting the system to remain in steady state conditions [20-22]. Equivalent electrical circuits (EECs) underscore the advantage of using linear theory and consider the circuits as a viable option to interpret EIS data [23, 24] by associating interfacial processes with electrical analogs. However, one of the major weaknesses of this analytical approach arises in how to select the corresponding EECs that not only fit the values but also provide a physical interpretation of the studied interface with quantitative parameters, especially when several layers are present in the system. One-dimensional transmission line modeling (TLM) has been used to investigate porous electrodes, iron oxide layers, evolution of magnesium-rich primers, and zinc-rich powder coatings by partitioning and characterizing an electrochemical interface into sub-elements of defined scale as corrosion cells [25-29]. A one-dimensional TLM approach can define the relationship between the resistance, driving potential, and corrosion rate of a degradation system based on the electrical balance of each element of the electrical circuit network [30].

However, it is difficult for this approach to take into account geometrical effects of the corroding systems, such as shape and localized pore distribution of coating layers, which have an impact on the corrosion rate [31].

In this study, the electrochemical behavior of a Cr(VI) coating/ AA2024-T3 substrate system immersed for 260 days in a 3.5% NaCl solution at a pH of 4 has been investigated using an EIS technique as well as morphology analysis. In addition, changes in the electrochemical impedance response over a long-term immersion have been estimated by using a deterministic and probabilistic 2D damage propagation model. This model is based on TLM and is proposed to understand the influence of heterogeneity in material properties and pore distributions of the corroding system by unifying the probability density function of the required property within the coating. Probability density function can describe physical distribution in percolation networks [32, 33]. The distribution of the electrolyte percolation length in the coating system is described by using the probability density function. The degradation mechanism from the 2D modeling is explained by using sensitivity analysis, and the validation of the modeling is considered by using experimental results.

2.2. Experimental Procedure

2.2.1. Materials and Sample Preparation

The epoxy primer Deft 02-Y-40 (Strontium chromate-based primer) was prepared by mixing its respective resin [Bisphenol-A-(epichlorhydrin) epoxy resin based] and cross-linker for one minute in a Flacktek Speedmixer at 1700 rpm. The

Cr(VI) -free polyurethane topcoat (Deft 99GY010) was prepared similarly. An induction time of 20-30 minutes was given to each coating. AA2024-T3 panels (76.2 mm x 152.4 mm x 0.762 mm) with a chemical composition (based on ASM material data sheet) of 0.1 wt% Cr; 0.15 wt% Ti; 0.25 wt% Zn; 0.5 wt% Fe; 0.5 wt% Si; 0.3–0.9 wt.% Mn; 1.2–1.8 wt% Mg; 3.8–4.9 wt% Cu; others 0.15 wt%; Al balance were cleaned with acetone and then mounted vertically on cardboard. Prior to the coating application, the prepared panels were pretreated with Alodine 1600 (Sodium Bichromate-based material). The epoxy primer was applied onto the aluminum panels with the help of a high volume low pressure (HVLP) spray gun to obtain a dry film thickness of approximately 30 μm. A similar procedure was followed for the application of the topcoat. The topcoat dry film thickness was about 40 μm. Finally, the panels were air cured for a week.

2.2.2. Electrochemical Techniques

A glass electrochemical cell (25 mm Inner Diameter, 30 mm Outer Diameter, 76.2 mm length) was sealed onto the coated panel by using an O-ring and a metallic clamp. Approximately 25 ml of 3.5 wt% NaCl solution adjusted to a pH of 4 with a sodium acetate/acetic acid buffer was poured into the cell glass container.

A three-electrode system was used to perform open circuit potential (OCP) and electrochemical impedance spectroscopy (EIS) measurements. The coated panel was used as the working electrode; a saturated calomel electrode was used as the reference electrode; and a Pt/Nb mesh electrode of 2 cm diameter was used as the counter electrode. The electrochemical measurements were performed using Gamry potentiostat/galvanostat /ZRA Reference 600^{TM} and a Faraday cage to avoid electromagnetic interferences. The EIS data were collected over a frequency range from 10 mHz to 20 kHz at open circuit potential with a sinusoidal AC perturbation of 10 mV rms. The data acquisition was controlled by Gamry Framework Version 5.8/EIS 300 software. All the measurements were performed in duplicates at room temperature for 260 days.

2.3. Two-dimensional Damage Propagation Model

2.3.1. Proposal of 2D Substrate/Coating Model

A multilayered system of coatings was designed for studying the electrochemical activities on porous surfaces including the transport mechanisms based on 2D deterministic and probabilistic approach to account for spatial distribution within solid state of a known commercial coating system. One layer system is certainly a simple and initial point to understand the transport and mechanistic analysis of different species. However, we want to present the model that can be utilized in a general integrated system formed by a multi-layer with a defined well known commercial system in this research. The validation is still a challenge because a real time quantitative tool should be used to either monolayer or multilayer. The mechanistic analysis with this developed tool as a further work will be considered in the future.

Based on the system comprising a top coat, a chromate-containing epoxy primer, CCC, and aluminum substrate, we considered a numerical element design by using a layer-by-layer composite coating strategy. Each segment in the designed domain has its own electrical properties including electrical resistivity and a dielectric constant, which can have different values based on the direction. The resistance $R_{(j,i)}$ and the capacitance $C_{(j,i)}$ of (j,i) element at each direction are defined as

$$R_{x(j,i)} = \rho_{x(j,i)} dx_i / dz_j \tag{2.1a}$$

$$R_{z(j,i)} = \rho_{z(j,i)} dz_j / dx_i \tag{2.1b}$$

$$C_{x(j,i)} = \varepsilon_{x(j,i)} \varepsilon_{0(j,i)} dz_j / dx_i \tag{2.1c}$$

$$C_{z(j,i)} = \varepsilon_{z(j,i)} \varepsilon_{0(j,i)} dx_i / dz_j \tag{2.1d}$$

where ρ denotes resistivity, ε is the dielectric constant, ε_0 is the permittivity of free space, and subscripts x and z explain x-direction and z-direction, respectively. In this model, the electrical properties of each segment are assumed to be isotropic. Each localized impedance is calculated with the help of an equivalent circuit analog at the elemental interface, which includes the electrical resistance and constant phase element (CPE) of the segments. The CPEs are used in this analysis instead of ideal capacitors due to the surface conditions or heterogeneous bulk properties of the composite coating systems [23, 34]. Fig. 2.1(a) describes the interfacial impedance between each segment as the physical degradation process of the coating system that is determined by the electrical materials' properties or the water-uptake process. The localized impedance at the interface of the segments is defined by the arithmetic averaged impedance at the cell interface, which is given by the following equation:

$$Z_{(j,i \leftrightarrow j,i+1)} = \frac{R_{x(j,i)}/2}{1 + (j\omega)^{\alpha_{x(j,i)}} C_{x(j,i)} R_{x(j,i)}} + \frac{R_{x(j,i+1)}/2}{1 + (j\omega)^{\alpha_{x(j,i+1)}} C_{x(j,i+1)} R_{x(j,i+1)}} \tag{2.2a}$$

$$Z_{(j,i\leftrightarrow j+1,i)} = \frac{R_{z(j,i)}/2}{1+(j\omega)^{\alpha_{z(j,i)}}C_{z(j,i)}R_{z(j,i)}} + \frac{R_{z(j+1,i)}/2}{1+(j\omega)^{\alpha_{z(j+1,i)}}C_{z(j+1,i)}R_{z(j+1,i)}} \qquad (2.2b)$$

where $Z_{(j,i\leftrightarrow j,i+1)}$ and $Z_{(j,i\leftrightarrow j+1,i)}$ are localized impedances at the interface between the (j,i) and the (j,i+1) elements and at the interface between the (j,i) and (j+1,i) elements, respectively. ω denotes a perturbation frequency, and α is an empirical exponent of the CPE.

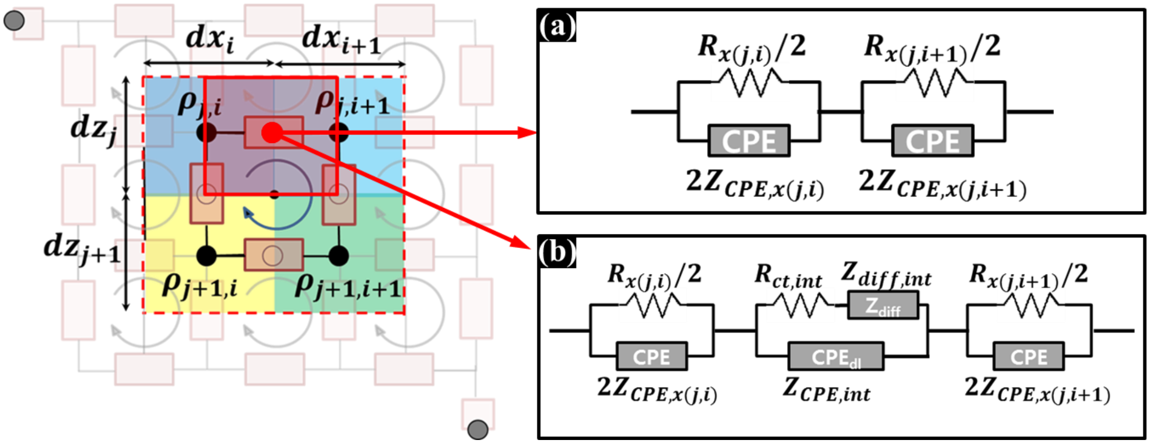

Figure 2.1 The schematic of 2D finite volume grid: (a) Impedance of interfacial elements as physical degradation process. (b) Impedance as electrochemical process at interface between the aluminum substrate and the CCC.

The interfacial impedance between segments that describes electrochemical reactions occurring at the interface is affected by non-faradaic impedance such as electrochemical double layer as well as faradaic impedance, which is composed of the charge transfer impedance induced from the kinetics of the charge transfer reaction and diffusion impedance. If electrochemical control processes such as charge transfer and diffusion phenomenon take place on the localized cell interface between the aluminum substrate and the CCC, impedance at the interface can be represented as shown in Fig. 2.1(b) and is defined by the following expressions.

$$\begin{aligned}\mathrm{Z}_{(\mathrm{j,i}\leftrightarrow\mathrm{j,i+1})} &= \frac{\mathrm{R}_{\mathrm{x(j,i)}}/2}{1+(\mathrm{j}\omega)^{\alpha_{\mathrm{x(j,i)}}}\mathrm{C}_{\mathrm{x(j,i)}}\mathrm{R}_{\mathrm{x(j,i)}}} \\ &+ \frac{1}{(\mathrm{j}\omega)^{\alpha_{\mathrm{x,int}}}\mathrm{C}_{\mathrm{x,dl}}+\dfrac{1}{\mathrm{R}_{\mathrm{ct,x,int}}+\mathrm{Z}_{\mathrm{diff,x,int}}}} \\ &+ \frac{\mathrm{R}_{\mathrm{x(j,i+1)}}/2}{1+(\mathrm{j}\omega)^{\alpha_{\mathrm{x(j,i+1)}}}\mathrm{C}_{\mathrm{x(j,i+1)}}\mathrm{R}_{\mathrm{x(j,i+1)}}}\end{aligned} \tag{2.3a}$$

$$\begin{aligned}\mathrm{Z}_{(\mathrm{j,i}\leftrightarrow\mathrm{j+1,i})} &= \frac{\mathrm{R}_{\mathrm{z(j,i)}}/2}{1+(\mathrm{j}\omega)^{\alpha_{\mathrm{z(j,i)}}}\mathrm{C}_{\mathrm{z(j,i)}}\mathrm{R}_{\mathrm{z(j,i)}}} \\ &+ \frac{1}{(\mathrm{j}\omega)^{\alpha_{\mathrm{z,int}}}\mathrm{C}_{\mathrm{z,dl}}+\dfrac{1}{\mathrm{R}_{\mathrm{ct,z,int}}+\mathrm{Z}_{\mathrm{diff,z,int}}}} \\ &+ \frac{\mathrm{R}_{\mathrm{z(j+1,i)}}/2}{1+(\mathrm{j}\omega)^{\alpha_{\mathrm{z(j+1,i)}}}\mathrm{C}_{\mathrm{z(j+1,i)}}\mathrm{R}_{\mathrm{z(j+1,i)}}}\end{aligned} \tag{2.3b}$$

where C_{dl} is the capacitance of the double layer, $\mathrm{R}_{\mathrm{ct,int}}$ is the charge transfer impedance, and $\mathrm{Z}_{\mathrm{diff,int}}$ is the diffusion impedance. In this work, we assume that the diffusion phenomenon is controlled in a thin layer, which has finite diffusion length of electroactive species from the electrolyte solution to the metal surface. Thus, the impedance response of diffusion can be defined as a modified Warburg impedance, which is given by [35]

$$\mathrm{Z}_{\mathrm{diff,int}} = \frac{\sigma(1-\mathrm{j})}{\sqrt{\omega}}\left[\frac{\sinh\sqrt{\frac{\omega\delta^2}{2D}}\cosh\sqrt{\frac{\omega\delta^2}{2D}}-\mathrm{j}\sin\sqrt{\frac{\omega\delta^2}{2D}}\cos\sqrt{\frac{\omega\delta^2}{2D}}}{\sinh^2\sqrt{\frac{\omega\delta^2}{2D}}+\sin^2\sqrt{\frac{\omega\delta^2}{2D}}}\right] \tag{2.4}$$

where σ is the Warburg coefficient, D is the diffusion coefficient, and δ is the thickness of the diffusion layer. δ^2/D is the characteristic diffusion time, which is assumed as 1 in order to reduce the number of calculation. The characteristic diffusion time value was enough for proposing qualitative variation of Warburg coefficient in this paper.

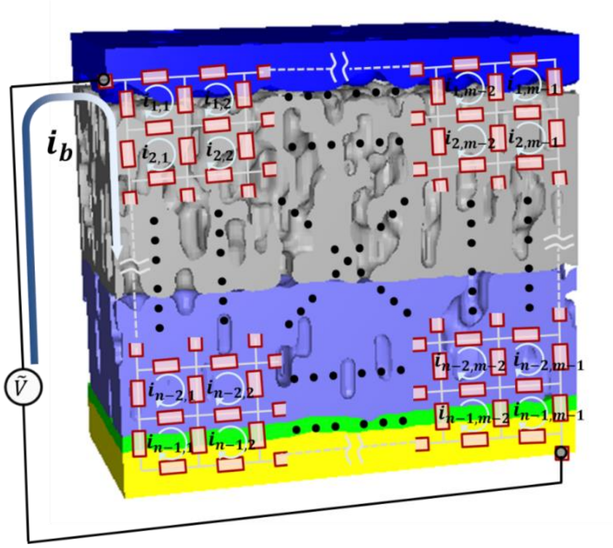

Figure 2.2 The schematic of 2D networks of electrochemical impedance elements for layer-by-layer composite coating system based on charge and energy conservation.

Based on the aforementioned local impedance at the interface of segments, the proposed composite coating system can be described as 2D networks of local electrochemical impedance elements, as shown in Fig. 2.2. The designed layer-by-layer composite coating system is divided into n x m segments. According to the local interfacial impedance of elements and Kirchhoff's law which is based on charge conservation ($\sum \mathrm{i}_{\mathrm{in}} = \sum \mathrm{i}_{\mathrm{out}}$) at a junction and energy conservation ($\sum \Delta \mathrm{V} = 0$) for any closed path, the total impedance of the designed system can be specified as the following:

$$\begin{aligned} Z_{\mathrm{total}}(\omega) = {} & l_x \sum_{k=1}^{n-1} Z_{k,2} + l_x \sum_{l=2}^{m} Z_{n,l} \\ & + l_x Z_{1,1} + l_x Z_{n,m} \\ & - l_x \left(\sum_{k=1}^{n-1} Z_{k,2} \cdot i_{k,1}/i_b + \sum_{l=2}^{m} Z_{n,l} \cdot i_{n-1,l-1}/i_b \right) \end{aligned} \tag{2.5}$$

where i is the electrical current of a closed path, and l_x is the length of the system in the x-direction.

2.3.2. Pore Distribution of Coated System

Previous works have used a probabilistic approach to describe water uptake within a barrier layer [21, 36, 37]. Orazem et al. developed the power-law CPE model, which can describe the insight into the distribution of electrolyte uptake and associated resistivity, and they considered the various volume fractions of electrolyte with respect to the coating thickness by using a power-law approach [37].

Water-uptake fields can also be considered as percolation clusters that are occupied by an electrolyte with a certain probability. If neighboring segments are occupied with an electrolyte, clusters are formed. The water-uptake in porous materials can be described as a random process of merging adjacent segments. Therefore, the number of electrolyte percolation lengths can be assumed to be inversely proportional to the water-uptake length because electrolyte has more possible regions to prevent penetration as the electrolyte propagates. This suggests that the log-normal probability density function (P) can be employed in order to define the distribution of the electrolyte percolation length, which is given by the following [32]:

$$\mathrm{P}(\mathrm{z}, \mu, \sigma) = 1/(\mathrm{z}\sigma\sqrt{2\pi})\exp[-(\ln(\mathrm{z}) - \mu)^2/(\,2\sigma^2)] \tag{2.6}$$

$$\mathrm{M} = \exp(\mu + \sigma^2/2) \tag{2.7}$$

$$\mathrm{V} = \exp(2\mu + \sigma^2)[\exp(\sigma^2) - 1] \tag{2.8}$$

where M is the mean of maximum percolation lengths of the electrolyte, and V is the variance of maximum electrolyte percolation lengths. The mean value M and the variance V can be calculated as functions of σ and μ which are the standard deviation and mean of the variable's natural logarithm, respectively, as shown in Equations (2.7) and (2.8).

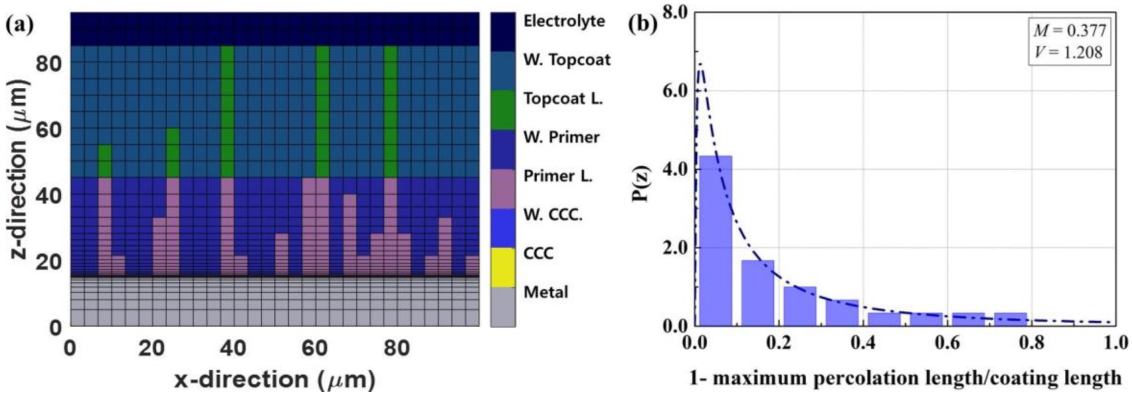

Figure 2.3 Pore distribution of coated system: (a) The pore position distribution based on randomly structured model. (b) Log-normal probability density function for the distribution of maximum electrolyte percolation length.

Fig. 2.3(a) demonstrates that the position distribution of various percolation lengths in the porous system can be generated by using the technique of a randomly structured model. This digitally stochastic model is coupled with specified statistical information such as the mean and variance of the maximum percolation length for electrolyte uptake, as described in Fig. 2.3(b). The mean M and the variance V values are 0.377 and 1.208 in this model, respectively.

2.3.3. The Computation Process of Multilayer System

The first estimation of the material properties for the data analysis with 2d model and the experimental result at dry condition was done by sensitivity analysis. The sensitivity analysis was considered to understand each theoretical parameter from variations in the parameter, which reveals the influence on the impedance of the system [38]. The detail process of calculation for the 2D model of distributed circuit elements is described in Fig. 2.4. The parameters obtained from the process describe the overall goodness of the fitting.

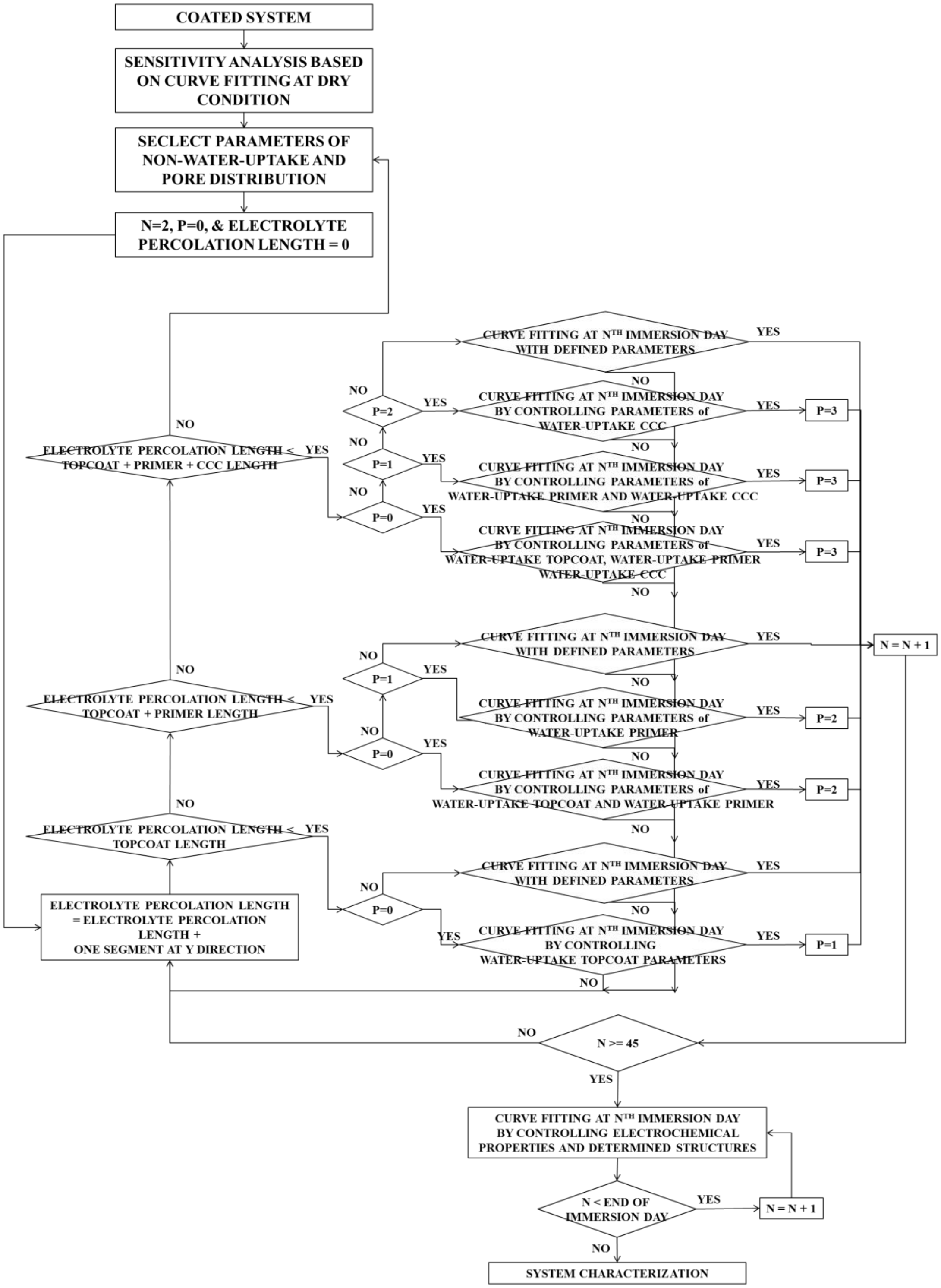

Figure 2.4 Flow diagram for obtaining parameters and characterization of the multilayer system.

2.4. Results and Discussion

Electrochemical impedance spectroscopy was used in order to characterize the interfacial mechanisms of a Cr(VI) coating/ AA2024-T3 substrate system immersed in 3.5 wt.% NaCl solution at a pH of 4.0 over 260 days. The experimental results were described quantitatively by the development of a 2D degradation model, which provides detailed interpretations of the existing mechanisms following exposure time. Different deterioration processes occurring at the multilayered coating composite system are quantified by integrating the localized transfer functions (impedance responses). The cross-section image of the layer-by-layer composite coating system is shown in Fig. 2.5(a). There is a total of three different layers covering the aluminum substrate: two coating layers, including a polyurethane top coat with 40 µm and a chromate-containing epoxy primer with 30 µm; also, a third layer (chromium conversion coating (CCC)) is formed on the aluminum substrate with a thickness between 10 nm to 50 nm, as illustrated in Fig. 2.5(b). Based on the surface morphology of the Cr(VI) coating/ AA2024-T3 substrate system, a layer-by-layer composite coating system was designed for the 2D computational model, as shown in Figures 2.5 (c) and (d). The parameters for the 2D simulation are shown in Tables 2.1 and 2.2. The overall responses of the multilayered system are governed by material properties that are dependent on the localized structures and electrochemical properties influenced by electrochemical reactions of local interfaces between each segment. The electrical resistivities and CPEs of each segment in the designed domain represent the material properties that are affected by the electrolyte transport throughout the coating system.

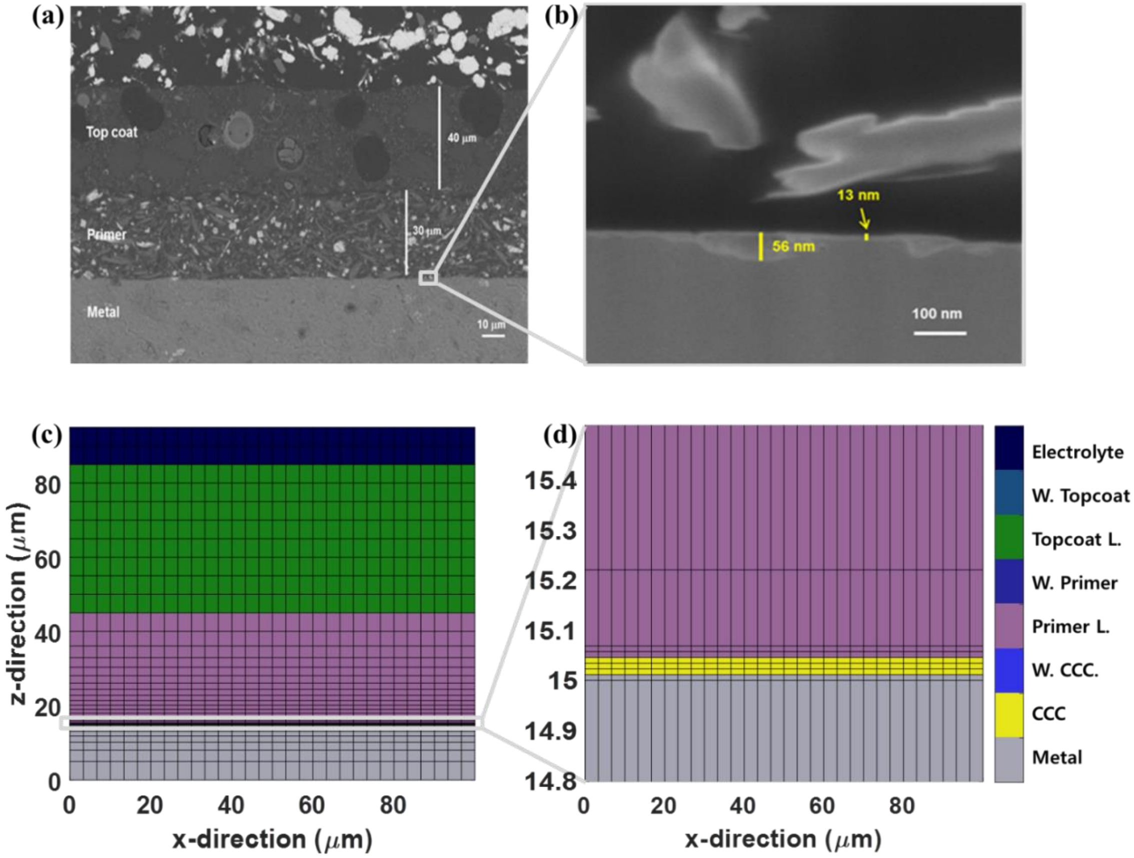

Figure 2.5 Surface morphology of Cr(VI) full military coating/ AA2024-T3 substrate system before immersing in 3.5 wt.% NaCl solution under pH =4.0: (a) Cross-section image of the coating system. (b) Magnified view of image (a) close to the CCC layer between primer layer and metal substrate. (c) Numerical design of layer-by-layer composite coating. (d) Magnified view of image (c) close to the CCC layer between primer layer and metal substrate.

The properties for the dry condition and the water-uptake process of topcoat, primer, and CCC were obtained using experimental results from the 2D model. The electrical resistivity and permittivity for the dry condition of each coating material are in the range of 10^{11}~10^{13} $\Omega \cdot \mathrm{cm}$ and 10^{-11}~10^{-10} $\mathrm{F} \cdot \mathrm{cm}^{-1}$, respectively. Following the water-uptake process of each coating segment, the magnitudes were modified to approximately 10^{7} $\Omega \cdot \mathrm{cm}$ and 10^{-10}~10^{-9} $\mathrm{F} \cdot \mathrm{cm}^{-1}$. From these results, the influence of the electrolyte diffusion on the dielectric properties of the material is clearly shown; resistivity decreased due to the presence of ionic species that created ionic conductive pathways along the material, and permittivity increased as a result of water penetration, which has a large permittivity value ($\varepsilon \sim 80$) compared to the corresponding values for polymeric materials ($\varepsilon \approx 3 - 4$) [39-41].

Table 2.1 Material properties for 2D multilayered microstructure.

Materials	**Designed Thickness** (μm)	**Electrical Resistivity** ($\Omega \cdot$ cm)	$\varepsilon_{(j,i)}\varepsilon_{0(j,i)}$ **Permittivity** ($\mathrm{F} \cdot \mathrm{cm}^{-1}$)	**n-value for CPE**
Electrolyte	N/A	20	0	1
Topcoat	40	1.3E13	1.4E-11	0.91
Primer	30.11	2.4E11	2.0E-11	0.75
CCC	0.034	1.0E11	5.0E-11	0.78
Aluminum	N/A	2.75E-6	0	1
Water-uptake Topcoat	N/A	3.0E7	5.0E-10	0.78
Water-uptake Primer	N/A	2.0E7	1.0E-9	0.78
Water-uptake CCC/ Water-uptake Cr(III) oxide layer	N/A	2.0E7	1.0E-9	0.78

Table 2.2 Electrochemical properties for 2D multilayered microstructure.

Materials	Diffusion Coefficient Factor $(\Omega \cdot \mathrm{cm}^2 \cdot \mathrm{s}^{-1/2})$	Charge Transfer Resistance $(\Omega \cdot \mathrm{cm}^2)$	Double layer Capacitator $(\mathrm{F} \cdot \mathrm{cm}^{-2})$	n-value for CPE
45 days of immersion	30000	18E6	3E-8	0.7
60 days of immersion	35000	8.5E6	6E-8	0.7
100 days of immersion	12000	3.5E5	1.2E-6	0.7
125 days of immersion	12000	6.5E5	1.1E-6	0.7
160 days of immersion	12000	8.5E5	1.0E-6	0.7

The degradation stages with time for this Cr(VI) coating/ AA2024-T3 system at low pH are illustrated in Fig. 2.6. The mechanisms represented the following conditions: intact at stage I, electrolyte-uptake at stage II, lixiviation of Cr(VI) ions at stage III, and the repassivation of the Cr (III) oxide layer at stage IV. The initial degradation mechanism described in stages I and II is developed due to the electrolyte transport through pores and defects of the multilayered coating. The degradation process occurring during stage III is related to the lixiviation of Cr(VI) from the chromate-containing epoxy primer into the electrolyte solution [7, 10, 42-44]. Stage IV involves the dynamic repairing of defects or newly created breaks in the CCC as the protective film. During the fourth stage, the breakdown of the CCC passivate film can occur in the presence of chloride ions. Chromium oxide layer can be de-passivated from complex reactions, which are attributed to the penetration of chloride ions through the chromium oxide layer [8, 45].

$$Cr_2O_3 + 4NaCl(l) + 5/2O_2 \rightarrow 2Na_2CrO_4 + 2Cl_2 \qquad (2.9)$$

$$Cr_2O_3 + 2NaCl(l) + 2O_2 \rightarrow Na_2Cr_2O_7(l) + Cl_2 \qquad (2.10)$$

However, these depassivated regions can be self-healed by the Cr(VI) ions that were dissolved in the electrolyte as a result of the lixiviation process. Cr(VI) ions diffused to the defect sites and reacted with the aluminum substrate in order to form $Cr(OH)_3$(s) and Cr_2O_3(s) [44].

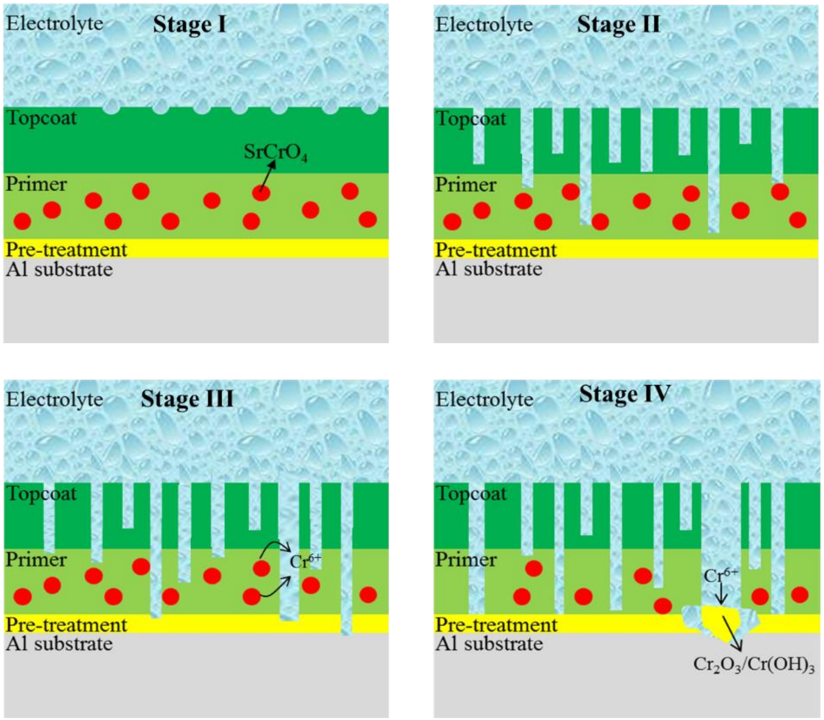

Figure 2.6 Schematic illustration diagrams of degradation mechanism of Cr(VI) coating/AA2024-T3 system – Stage I: intact, Stage II: electrolyte uptake, Stage III: lixiviation of Cr(VI), Stage IV: self-healing/stable Cr(III) oxide layer.

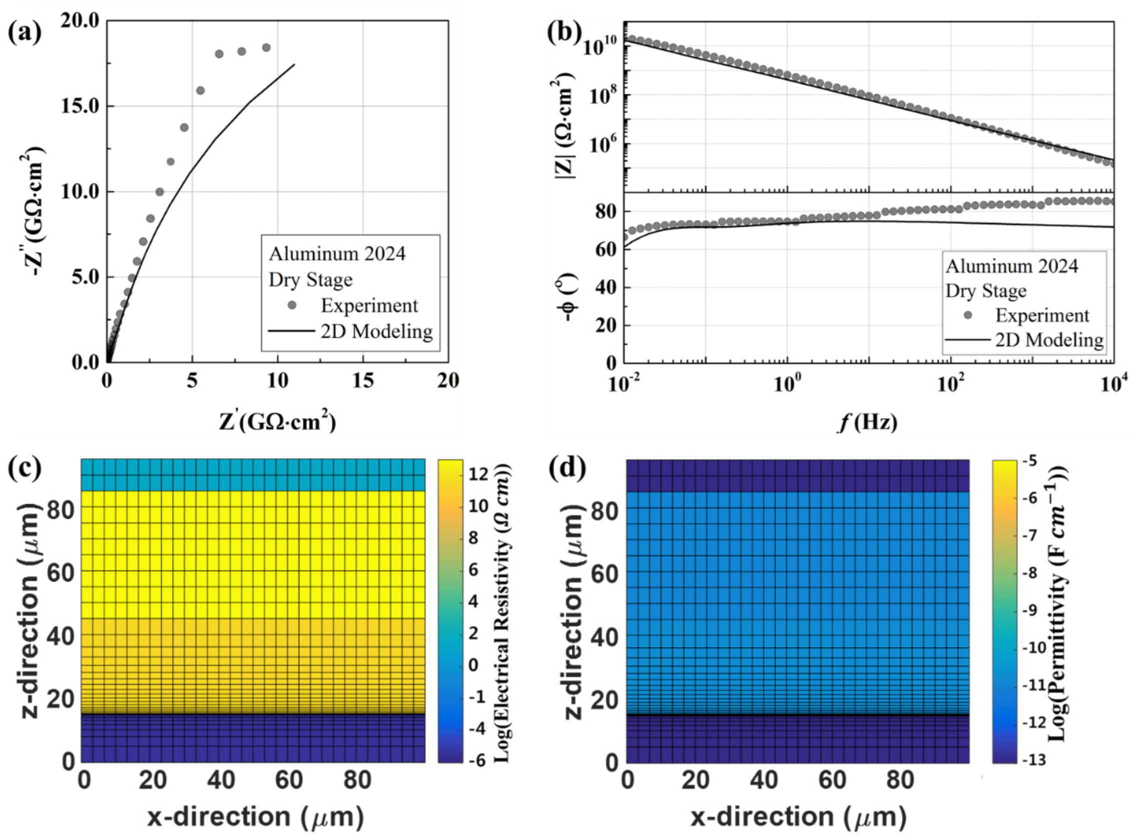

Figure 2.7 Impedance spectra of experiment and 2D modeling for Cr(VI) coating/ AA2024-T3 system immersed in 3.5 wt.% NaCl solution under pH =4.0 in the first day of immersion: (a) Nyquist diagram. (b) Bode diagram. (c) Resistivity plot. (d) Permittivity plot.

2.4.1. Stage I and II Intact and Water Uptake Conditions

The impedance response for the Cr(VI) coating/ AA2024-T3 substrate system at its initial stage when immersed in an acid electrolyte is shown in Fig. 2.7. The impedance response of the coating/aluminum system exhibits the characteristic of a capacitive behavior at a large impedance modulus of 0.01 Hz and a phase angle close to -90° along the frequency range. Since the coated layer is considered dry, water uptake and any other subsisting free ions within the polyurethane topcoat is minimum or negligible. Thus, the topcoat, which has the distribution of high resistance segments of around 10^{13} ohm cm^2, as indicated in Fig. 2.7, can electronically act as a good insulated layer. This high capacitive behavior considers the intact polymer layer influencing the space-charge-polarization region in the composite coating system [46].

With time, water uptake in the form of electrolyte transportation occurs through the topcoat and reaches the chromate-containing epoxy primer following the chromate conversion coating on the metal surface. This composite coating layer is not homogeneous due to pore distribution and different properties conferred to the material during synthesis, which produces heterogeneous or random-uptake processes. Nyquist and Bode representations during the degradation mechanism between the 2nd and 35th immersion day are described in Fig. 2.8. The presence or formation of pores in each layer gives rise to significant differences in the impedance response due to the electrical properties of the electrolyte solution that fills pores. Following the first day of exposure, Fig. 2.8(a) shows that the magnitude of impedance decreases rapidly because the electrolyte uptake through the outermost layer of the coating system, which is the polyurethane topcoat, is very rapid. Water-uptake is considered as a dominant process for damage evolution of coating at the very beginning of immersion. During this process, as illustrated in Figs. 2.8(b) and (c), the insulating structure of the polymer composed of organic compounds is locally changed and modifies the characteristics of the overall impedance, which is considered as ionic transport and subsequent substrate activation [46]. The basic purpose of the polyurethane topcoat is functionally used for UV protection, but there can be the polyurethane topcoat not to provide an effective barrier

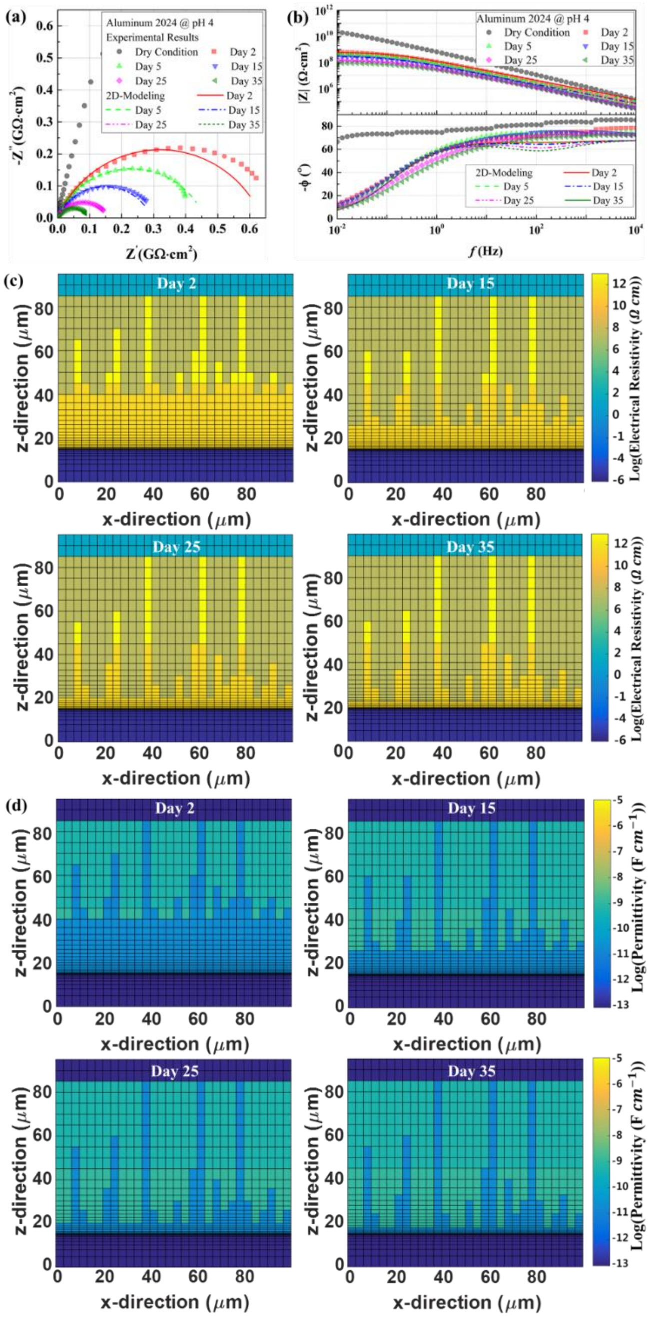

Figure 2.8 Effect of electrolyte penetration on the impedance response of Cr(VI) coating/ AA2024-T3 system immersed in 3.5 wt.% NaCl solution under pH =4.0 between the 2nd and 35th immersion day: (a) Nyquist diagram and (b) Bode diagram with experimental and 2D modeling results. The distributions of (c) electrical resistivities and (d) permittivities of each segment dependent on electrolyte penetration process for damage evolution mechanism of the multilayered coating system with various time periods.

against solution [47]. Thus, the electrolyte penetrates quickly through the topcoat at the 2nd day of immersion, as shown in Figs. 2.8(b) and (c). At this time, the epoxy primer layer functions as an electrical insulating barrier of the composite coating system because electrolyte penetrates inside the topcoat. The highest resistivity segments for electrical insulating (about $10^{11}\ \Omega \cdot \text{cm}$ indicated in Fig. 2.8(b)) are distributed in the epoxy primer layer, and the capacitive loop displayed in the complex format represents the combining effect of the resistance and CPE behavior. At longer exposure times, the radius of the capacitive loop in the complex representation is continuously decreasing due to higher penetration of water and ionic species along the composite coatings, and the total impedance decreases.

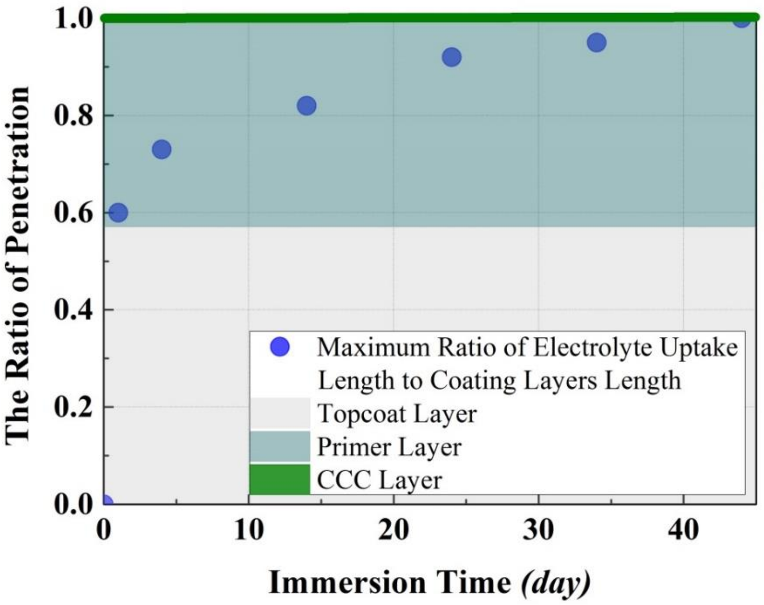

Figure 2.9 The electrolyte penetration ratio of the maximum penetration length of electrolyte to the length of coating layers dependent on immersion time.

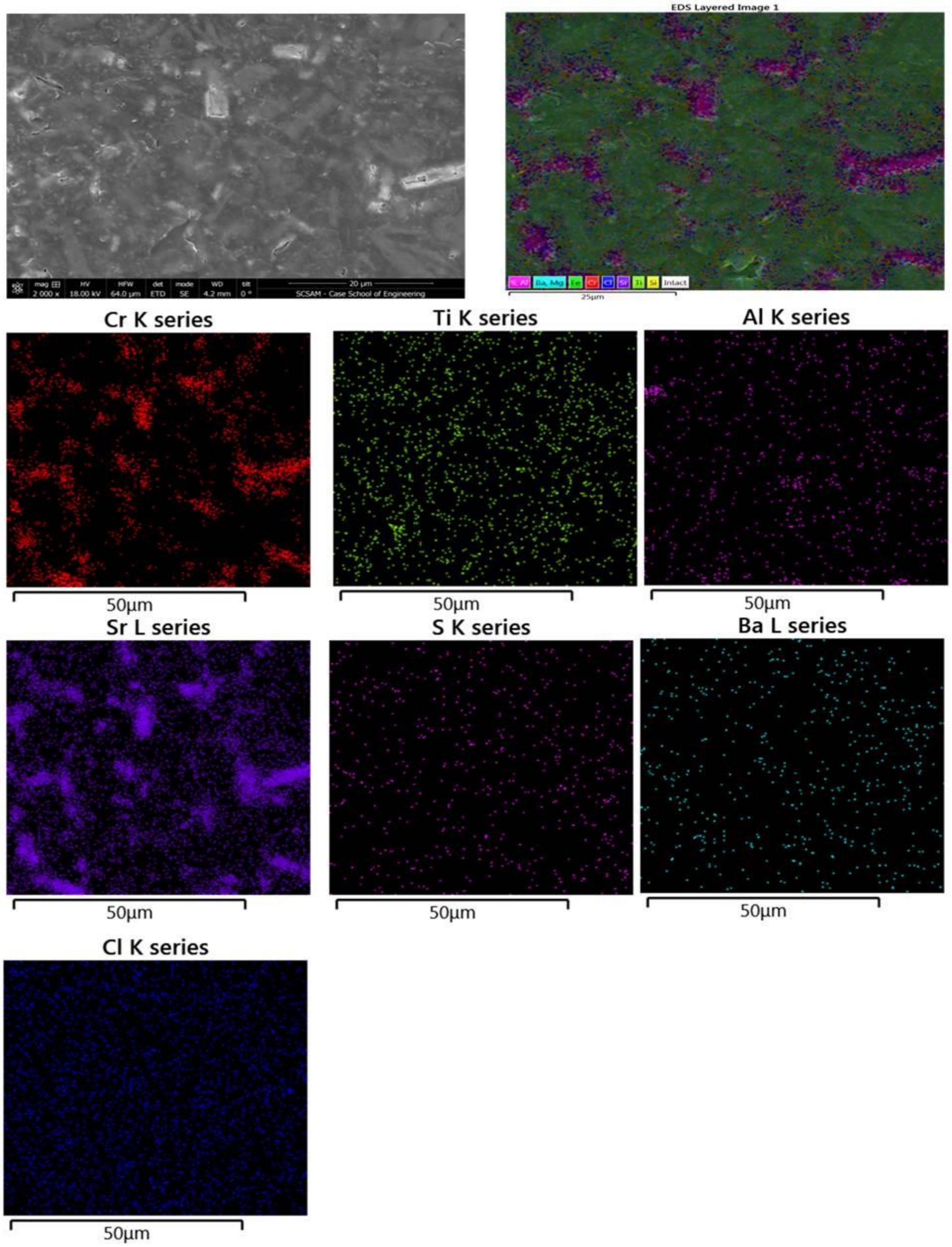

Figure 2.10 EDS mapping of Cr(VI) coating/ AA2024-T3 system immersed in 3.5 wt.% NaCl solution under pH =4.0 over 260 days.

The impedance response of the porous composite coating system and the effect of electrolyte penetration ratio can be useful to understand the barrier protection behavior of the system. The length ratio of electrolyte penetration, which is defined as the ratio of the maximum uptake length in a direction perpendicular to the sample surface to the length of the multilayers of the coating, is estimated by immersion time, as illustrated in Fig. 2.9. The trend of electrolyte penetration ratio versus immersion time is assumed to demonstrate approximately square-root behavior, which means the primer layer is a better protection barrier for electrolyte uptake than the topcoat. As shown in Fig. 2.10, the epoxy primer is a heterogeneous material comprising a number of inorganic phases such as titanium dioxide (TiO_2), strontium chromate ($SrCrO_4$), and barite ($BaSO_4$) incorporated into the organic matrix [10]. These pigments in the primer would reduce the existence of pores and improve the barrier protection for electrolyte penetration as well as provide active corrosion protection to the metallic substrate.

2.4.2. Stage III Lixiviation Stage

Following 45 days of immersion, the electrolyte reaches the surface of the aluminum substrate through the pores of the primer and inert CCC, as illustrated in Fig. 2.11(c-d). From this stage III, the electrochemical behavior of the whole system is affected by not only local physical degradation such as electrolyte-uptake but also localized electrochemical processes such as charge transfer and diffusion. At the substrate/electrolyte interface, mass and charge transfer influence appears in parameters illustrated in Table 2.2.

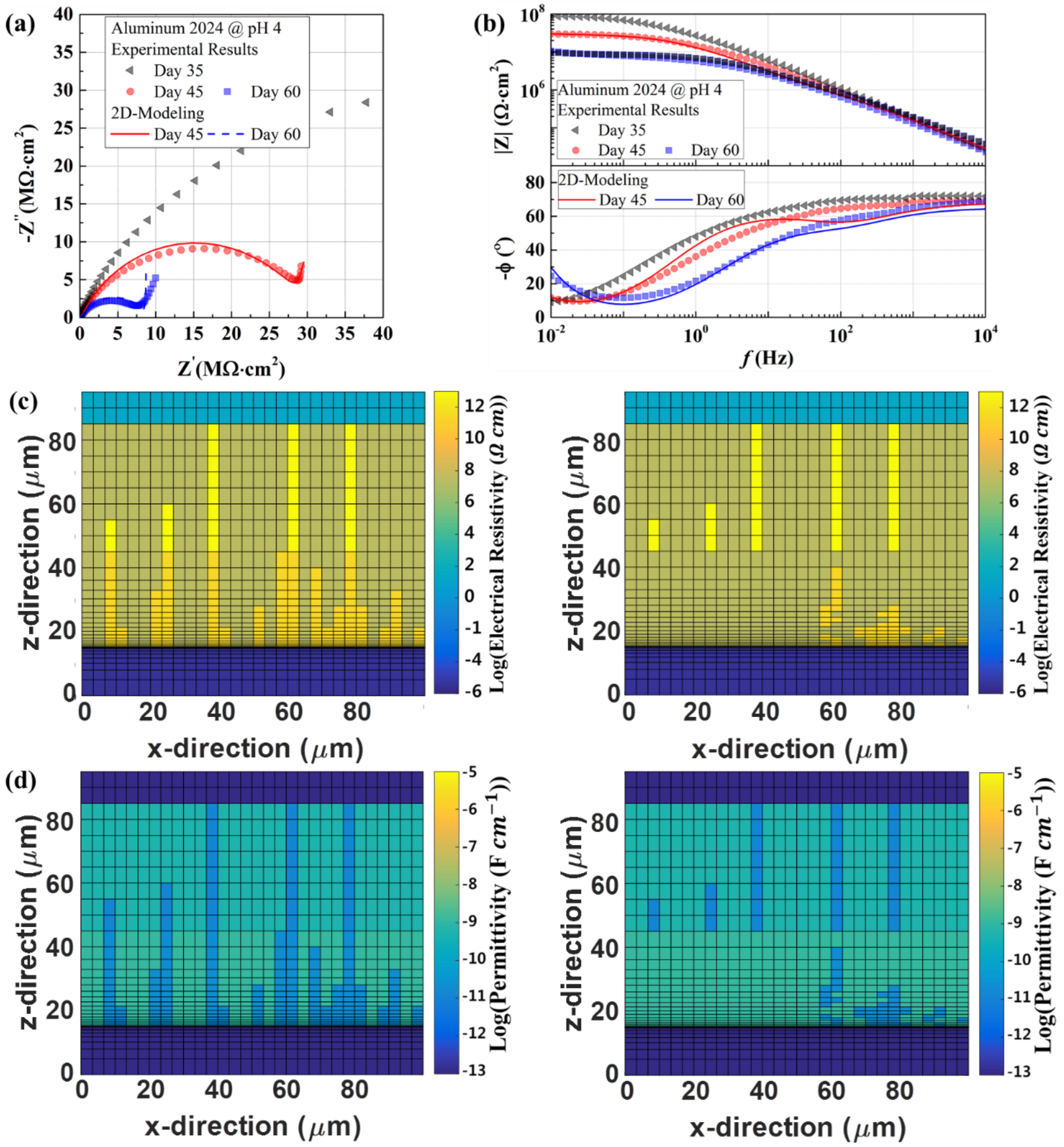

Figure 2.11 Effect of electrolyte penetration on the impedance response of Cr(VI) coating/ AA2024-T3 system immersed in 3.5 wt.% NaCl solution under pH =4.0 at the 45th and 60th day of immersion: (a) Nyquist diagram with experimental and 2D modeling results. (b) Bode diagram. (c) Electrical resistivities and (d) permittivities of each segment due to lixiviation process for damage evolution mechanism of the multilayered coating system with various time periods.

As shown in Fig. 2.11(a), diffusion characteristic behavior at low frequency regime is detected in complex impedance plane, but this behavior does not obey linear Warburg behavior, which considers an ideal infinite-length diffusion from the electrolyte to the metal surface [46]. This is because local aluminum elements for the dissolution and diffusion as the anodic reaction from the local pores of CCC occupied with electrolyte are finite in dimensions, so modified Warburg behaviors, which describe the proper finite-length diffusion processes, are observed.

The equivalent area of the electrolyte-uptake primer (about $10^7 \ \Omega \cdot \mathrm{cm}$ resistivity) at day 60 is extended more than the area at day 45, as described in Fig. 2.11(c). There can be a possibility to attribute to this increased area due to the delamination of the paint film, but the visual inspection of the samples did not indicate any delamination processes during experiment. Thus, to explain and describe the higher equivalent area of the electrolyte uptake primer, the only major phenomenon for designing a simple model was only considered by using chromate pigments. The chromium species added in the epoxy primer are electrolyte-soluble, so the $SrCrO_4$ compound could be lixiviated into the bulk solution when it is exposed to the electrolyte solution [48]. The dissolution of $SrCrO_4$ modifies pores in the epoxy primer, and these modified pores are filled with the electrolyte. The more areas of the electrolyte-uptake epoxy primer create more conducting paths, as shown in Fig. 2.11(c). This latter can be followed by the smaller radius evolution of the semi-circle of impedance response in the complex plane of Fig. 2.11(a). At day 60, the behavior of the charge transfer phenomenon is more predominant than the charge transfer phenomenon at day 45 because the area of the electrolyte-uptake epoxy primer increases at day 60, the primer has higher possibilities to create connected paths of pores within the primer and the pores in CCC, and the electroactive surface area between aluminum substrate and electrolyte is increased.

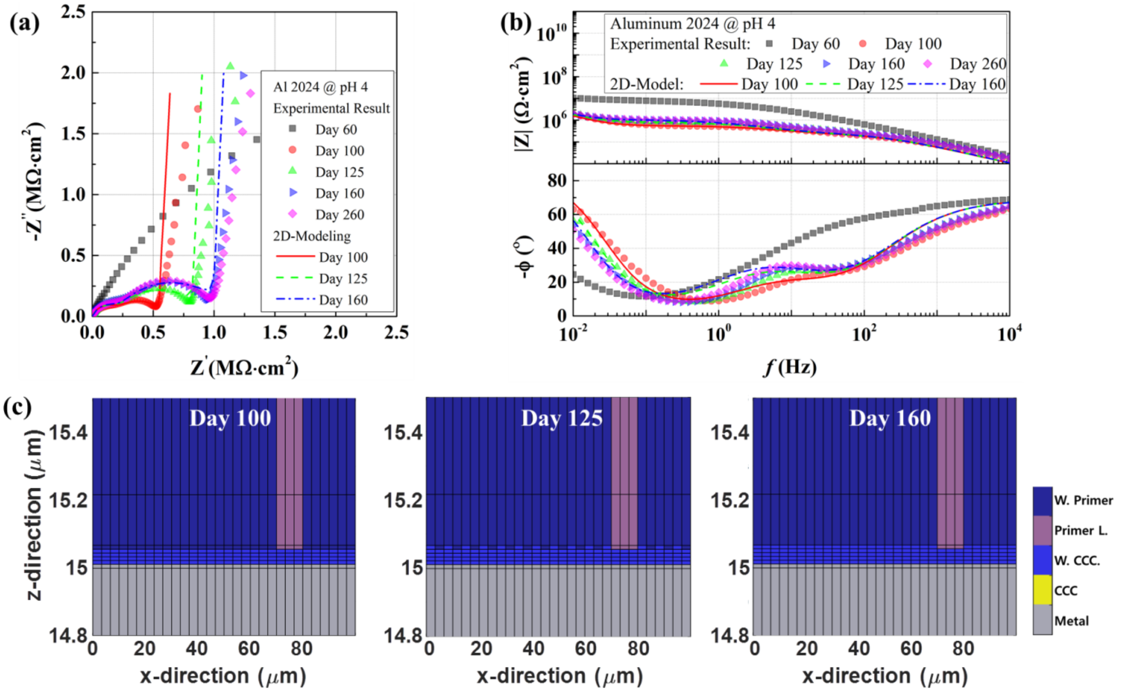

Figure 2.12 Effect of electrolyte penetration on the impedance response of Cr(VI) coating/AA2024-T3 system immersed in 3.5 wt.% NaCl solution under pH =4.0 at the 100th, 125th, and 160th day of immersion: (a) Nyquist diagram with experimental and 2D modeling results. (b) Bode diagram. (c) Self-healing process of the multilayered coating system with various time periods.

2.4.3. Stage IV Self-healing/Stable Cr(III) Oxide Layer

Following 100 days of immersion, the impedance plot showed a significant change in the electrochemical mechanism, as described in Fig. 2.12. This time period demonstrates the influence of stage IV is in the damage evolution. From the Nyquist diagram, the presence of two impedance loops from high to intermediate frequencies and a quasi-vertical straight line at the low frequency range are shown. The capacitive loop at the high frequency regime represents the electrical resistance of the composite coatings, which are mainly affected by the electrolyte-uptake in the topcoat and primer regions with a magnitude about 10^7 ($\Omega \cdot$ cm). As shown in Fig. 2.12 (b), the time constant at intermediate frequencies describes electrical resistance of Cr(III) oxide layer and the charge transfer process between the aluminum substrate/oxide layer and the electrolyte (i.e., anodic dissolution of the aluminum substrate and reduction reaction of the Cr(VI) ions to form insoluble hydrated chromium oxide) [44]. The quasi-vertical straight line at low frequency region can be attributed to the presence of a diffusion phenomenon due to the reactions occurring at the metal surface [49]. Furthermore, the magnitude at high frequencies remained nearly constant; this indicates that the organic layer was completely saturated with the electrolyte after 100 days of immersion. In contrast, the capacitive loop formed at medium frequencies, and the charge transfer mechanism was favored due to the self-healing process provided by the Cr(VI) ions, assuming that these ions were previously dissolved in the electrolyte solution during the lixiviation process taking place in stage II. The self-healing process is observed due to the leaching of Cr(VI) ions from the epoxy primer into the electrolyte solution that is subsequently transported to the aluminum substrate leading to repassivation of the chromium oxide layer on the active sites [10, 50]. According with the chromium oxide layer, which is formed at the aluminum surface, several steps are involved in the corrosion protection mechanism of this thin oxide layer; this explains its excellent performance in the protection of the metal substrate during Stage IV [7, 51-53]. The first step is where the aluminum surface is oxidized:

$$\mathrm{Al} \rightarrow \mathrm{Al}^{3+} + 3\mathrm{e}^{-} \tag{2.11}$$

Meanwhile the chromium conversion coating is formed due to electrochemical reactions at the AA2024-T3 substrate where the Cr(VI) is reduced to Cr(III) [7]:

$$\mathrm{Cr_2O_7^{2-}} + 8\mathrm{H}^{+} + 6\mathrm{e}^{-} \rightarrow 2\mathrm{Cr(OH)_3} + \mathrm{H_2O} \tag{2.12}$$

This Cr(III) oxide layer provides good barrier protection due to its hydrophobic nature, good adhesion, and inhibition of the oxygen reduction reaction and metal dissolution [7]. In addition, the residual Cr(VI) ions can also provide self-healing to the damage areas and repassivation of the oxide layer similar to the chromate pigments in the epoxy primer by leaching from the CCC and transport to the corrosion sites by diffusion and/or migration processes [51].

During the self-healing process, the rate of electrochemical interfacial reaction controls the growth of the Cr(III) oxide layer. As shown in Fig. 2.12 (c), the Cr(III) oxide layer grows over longer immersion times. Also, Fig. 2.13 experimentally shows the thickness change of the Cr(III) oxide layer. The thickness of the CCC before exposure is in the range of 10 nm to 50 nm. However, after 260 days of immersion, the average thickness (over 50 nm) of CCC increases (shown in Fig. 2.13(d)). This growth of the Cr(III) oxide layer results in the increase of the capacitive loop formed at medium frequencies, as described in Figs. 2.12 (a) and (b). This is due to the fact that the formation of the Cr(III) oxide layer can play a role in the insulator and decrease charge transfer areas.

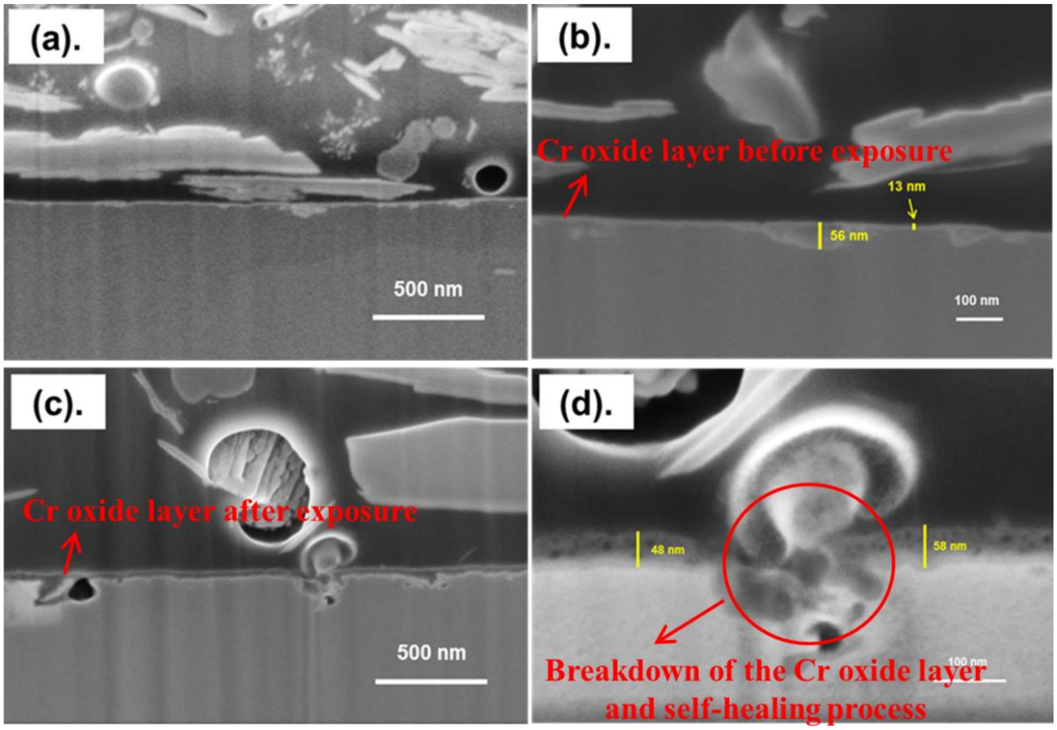

Figure 2.13 SEM morphology of CCC in the interface of primer/substrate before (a-b) and after (c-d) exposure for 260 days.

The Warburg coefficient, which expresses a mass transfer process including ionic diffusion [54], can also be used to explain the degradation mechanism based on the activation process occurring at the interface. As shown in Fig. 2.14, the Warburg coefficient based on the activation process was shown to increase up to $35000\ \Omega \cdot \mathrm{cm}^2 \cdot \mathrm{s}^{-1/2}$ at stage III as an activation period, but a constant value ($11000\ \Omega \cdot \mathrm{cm}^2 \cdot \mathrm{s}^{-1/2}$) was obtained at stage IV due to forming the stable oxide layer through the self-healing process. This explains that the Cr(III) oxide layer can play a role as a barrier to delay corrosion phenomenon in the multilayered composite system.

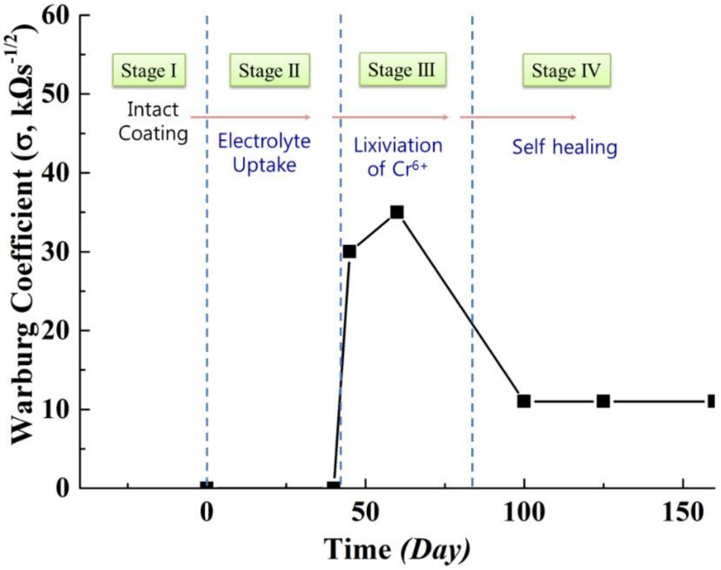

Figure 2.14 Degradation mechanism of Cr(VI) coating/ AA2024-T3 system based on Warburg constant for diffusion phenomenon.

2.5. Summary

- In this work, the degradation mechanism of a composite Cr(VI) coating/aluminum alloy 2024-T3 system was studied by EIS in 3.5% NaCl solution at low pH. Following exposure for 260 days in 3.5 NaCl, the composite coating shows four different stages marked as 1) intact coating, 2) water-uptake, 3) lixiviation of Cr $^{6+}$, and 4) the self-healing.
- A 2D damage propagation model is proposed to characterize and quantify each stage in the degradation mechanism of a multilayered coating/aluminum substrate system. The 2D damage evolution technique is assumed to be based on a deterministic approach and stochastic modeling for coating pore distributions. The physical (electrolyte-uptake) and electrochemical degradation processes are explained by using the spatial distribution of electrical material properties such as electrical

resistivity and permittivity as well as the interfacial distribution for electrochemical properties including diffusion and charge transfer parameters.

- To quantitatively understand the mechanism of physical degradation through electrolyte-uptake, the 2D model was developed by distributing and integrating electrical resistivity (10^{6}~10^{10} $\Omega \cdot \mathrm{cm}$) and permittivity (10^{-10}~10^{-7} $\mathrm{F} \cdot \mathrm{cm}^{-1}$) of each segment based on composite coating materials and water-uptake processes over various immersion times at stages I and II. The computational results showed that the overall magnitude of impedance response at 0.01 Hz decreases from around 10^{10} $\Omega \cdot \mathrm{cm}^{2}$ to 10^{7} $\Omega \cdot \mathrm{cm}^{2}$, which represents compatible results with experimental condition.
- By using the integration of local electrochemical impedances at each segment interface, the electrochemical behaviors of a self-healing process provided by the chromium (VI) dissolved in the electrolyte solution are validated with experimental results. A stable Warburg coefficient at stage IV can be obtained through the self-healing process.

2.6. References

[1] Z. Huda, N.I. Taib, T. Zaharinie, Characterization of 2024-T3: An aerospace aluminum alloy, Materials Chemistry and Physics, 113 (2009) 515-517.

[2] M. Nakai, T. Eto, New aspect of development of high strength aluminum alloys for aerospace applications, Materials Science and Engineering: A, 285 (2000) 62-68.

[3] J.E. Hatch, A. Association, Aluminum: properties and physical metallurgy, ASM International, 1984.

[4] R. Buchheit, R. Grant, P. Hlava, B. McKenzie, G. Zender, Local dissolution phenomena associated with S phase (Al2CuMg) particles in aluminum alloy 2024-T3, Journal of the Electrochemical Society, 144 (1997) 2621-2628.

[5] G.S. Chen, M. Gao, R.P. Wei, Microconstituent-induced pitting corrosion in aluminum alloy 2024-T3, Corrosion, 52 (1996) 8-15.

[6] G. Ilevbare, O. Schneider, R. Kelly, J. Scully, In situ confocal laser scanning microscopy of AA 2024-T3 corrosion metrology I. Localized corrosion of particles, Journal of the Electrochemical Society, 151 (2004) B453-B464.

[7] M. Kendig, S. Jeanjaquet, R. Addison, J. Waldrop, Role of hexavalent chromium in the inhibition of corrosion of aluminum alloys, Surface and Coatings Technology, 140 (2001) 58-66.

[8] J. Zhao, G. Frankel, R.L. McCreery, Corrosion protection of untreated AA-2024-T3 in chloride solution by a chromate conversion coating monitored with Raman spectroscopy, Journal of the Electrochemical Society, 145 (1998) 2258-2264.

[9] R.L. Twite, G.P. Bierwagen, Review of alternatives to chromate for corrosion protection of aluminum aerospace alloys, Progress in Organic Coatings, 33 (1998) 91-100.

[10] F.H. Scholes, S.A. Furman, A.E. Hughes, T. Nikpour, N. Wright, P.R. Curtis, C.M. Macrae, S. Intem, A.J. Hill, Chromate leaching from inhibited primers: Part I. Characterisation of leaching, Progress in Organic Coatings, 56 (2006) 23-32.

[11] J. Sinko, Challenges of chromate inhibitor pigments replacement in organic coatings, Progress in Organic Coatings, 42 (2001) 267-282.

[12] G.M. Treacy, G.D. Wilcox, M.O.W. Richardson, Monitoring the corrosion behaviour of chromate-passivated aluminium alloy 2014 A-T6 by electrochemical impedance spectroscopy during salt fog exposure, Surface and Coatings Technology, 114 (1999) 260-268.

[13] M. Kendig, R. Buchheit, Corrosion inhibition of aluminum and aluminum alloys by soluble chromates, chromate coatings, and chromate-free coatings, Corrosion, 59 (2003) 379-400.

[14] H. Shi, F. Liu, E. Han, Corrosion behaviour of sol–gel coatings doped with cerium salts on 2024-T3 aluminum alloy, Materials Chemistry and Physics, 124 (2010) 291-297.

[15] J. Tang, Z. Han, Y. Zuo, Y. Tang, A corrosion resistant cerium oxide based coating on aluminum alloy 2024 prepared by brush plating, Applied Surface Science, 257 (2011) 2806-2812.

[16] I.A. Kartsonakis, A.C. Balaskas, G.C. Kordas, Influence of cerium molybdate containers on the corrosion performance of epoxy coated aluminium alloys 2024-T3, Corrosion Science, 53 (2011) 3771-3779.

[17] H.D. Johansen, C.M.A. Brett, A.J. Motheo, Corrosion protection of aluminium alloy by cerium conversion and conducting polymer duplex coatings, Corrosion Science, 63 (2012) 342-350.

[18] M. Schem, T. Schmidt, J. Gerwann, M. Wittmar, M. Veith, G.E. Thompson, I.S. Molchan, T. Hashimoto, P. Skeldon, A.R. Phani, S. Santucci, M.L. Zheludkevich, CeO2-filled sol–gel coatings for corrosion protection of AA2024-T3 aluminium alloy, Corrosion Science, 51 (2009) 2304-2315.

[19] R.G. Buchheit, H. Guan, S. Mahajanam, F. Wong, Active corrosion protection and corrosion sensing in chromate-free organic coatings, Progress in Organic Coatings, 47 (2003) 174-182.

[20] F. Mansfeld, M. Kendig, Electrochemical impedance spectroscopy of protective coatings, Materials and Corrosion, 36 (1985) 473-483.

[21] S. Amand, M. Musiani, M.E. Orazem, N. Pébère, B. Tribollet, V. Vivier, Constant-phase-element behavior caused by inhomogeneous water uptake in anti-corrosion coatings, Electrochimica Acta, 87 (2013) 693-700.

[22] S. Mirabedini, G. Thompson, S. Moradian, J. Scantlebury, Corrosion performance of powder coated aluminium using EIS, Progress in Organic Coatings, 46 (2003) 112-120.

[23] P. Campestrini, E.P.M. van Westing, J.H.W. de Wit, Influence of surface preparation on performance of chromate conversion coatings on Alclad 2024 aluminium alloy Part II: EIS investigation, Electrochimica Acta, 46 (2001) 2631-2647.

[24] D. Chidambaram, C.R. Clayton, M.W. Kendig, G.P. Halada, Surface pretreatments of aluminum alloy AA2024-T3 and formation of chromate conversion coatings - II. Composition and electrochemical behavior of the chromate conversion coating, Journal of the Electrochemical Society, 151 (2004) B613-B620.

[25] I.D. Raistrick, Impedance studies of porous-electrodes, Electrochimica Acta, 35 (1990) 1579-1586.

[26] K.N. Allahar, D. Battocchi, G.P. Bierwagen, D.E. Tallman, Transmission line modeling of EIS data for a Mg-rich primer on AA 2024-T3, Journal of the Electrochemical Society, 157 (2010) C95-C101.

[27] J. Niu, J.I. Barraza-Fierro, H. Castaneda, Quantification of protective properties of the coating/corrosion product/steel interface by integration of transmission line model with EIS results, Journal of Coatings Technology and Research, 12 (2015) 393-405.

[28] S.G. Real, A.C. Elias, J.R. Vilche, C.A. Gervasi, A. Di Sarli, An electrochemical impedance spectroscopy study of zinc rich paints on steels in artificial sea water by a transmission line model, Electrochimica Acta, 38 (1993) 2029-2035.

[29] H. Marchebois, C. Savall, J. Bernard, S. Touzain, Electrochemical behavior of zinc-rich powder coatings in artificial sea water, Electrochimica Acta, 49 (2004) 2945-2954.

[30] D.D. Macdonald, Reflections on the history of electrochemical impedance spectroscopy, Electrochimica Acta, 51 (2006) 1376-1388.

[31] J.X. Jia, G.L. Song, A. Atrens, Influence of geometry on galvanic corrosion of AZ91D coupled to steel, Corrosion Science, 48 (2006) 2133-2153.

[32] J. Hicks, A. Behnam, A. Ural, Resistivity in percolation networks of one-dimensional elements with a length distribution, Physical Review E, 79 (2009).

[33] R. Hilfer, Local-porosity theory for flow in porous-media, Physical Review B, 45 (1992) 7115-7121.

[34] P. Campestrini, H. Terryn, J. Vereecken, J.H.W. de Wit, Chromate conversion coating on aluminum alloys - III. Corrosion protection, Journal of the Electrochemical Society, 151 (2004) B370-B377.

[35] H.H. Girault, Analytical and physical electrochemistry, EPFL press, 2004.

[36] Y. Ben Amor, E.M.M. Sutter, H. Takenouti, M.E. Orazem, B. Tribollet, Interpretation of electrochemical impedance for corrosion of a coated silver film in terms of a pore-in-pore model, Journal of the Electrochemical Society, 161 (2014) C573-C579.

[37] M.E. Orazem, B. Tribollet, V. Vivier, D.P. Riemer, E. White, A. Bunge, On the use of the power-law model for interpreting constant-phase-element parameters, Journal of the Brazilian Chemical Society, 25 (2014) 532-539.

[38] H. Castaneda, M. Urquidi-Macdonald, Detecting external failures in coated, buried pipelines: Theoretical model and experimental verification, Corrosion, 60 (2004) 538-547.

[39] J.H. Park, G.D. Lee, H. Ooshige, A. Nishikata, T. Tsuru, Monitoring of water uptake in organic coatings under cyclic wet–dry condition, Corrosion Science, 45 (2003) 1881-1894.

[40] W.-G. Ji, J.-M. Hu, J.-Q. Zhang, C.-N. Cao, Reducing the water absorption in epoxy coatings by silane monomer incorporation, Corrosion Science, 48 (2006) 3731-3739.

[41] M.-Y. Jiang, L.-K. Wu, J.-M. Hu, J.-Q. Zhang, Silane-incorporated epoxy coatings on aluminum alloy (AA2024). Part 1: Improved corrosion performance, Corrosion Science, 92 (2015) 118-126.

[42] M. Kendig, A.J. Davenport, H. Isaacs, The mechanism of corrosion inhibition by chromate conversion coatings from X-ray absorption near edge spectroscopy (XANES), Corrosion Science, 34 (1993) 41-49.

[43] J. Zhao, L. Xia, A. Sehgal, D. Lu, R. McCreery, G.S. Frankel, Effects of chromate and chromate conversion coatings on corrosion of aluminum alloy 2024-T3, Surface and Coatings Technology, 140 (2001) 51-57.

[44] P. Campestrini, E.P.M. van Westing, A. Hovestad, J.H.W. de Wit, Investigation of the chromate conversion coating on Alclad 2024 aluminium alloy: effect of the pH of the chromate bath, Electrochimica Acta, 47 (2002) 1097-1113.

[45] Y.S. Li, M. Spiegel, S. Shimada, Corrosion behaviour of various model alloys with NaCl-KCl coating, Materials Chemistry and Physics, 93 (2005) 217-223.

[46] C. Fernández-Sánchez, C.J. McNeil, K. Rawson, Electrochemical impedance spectroscopy studies of polymer degradation: application to biosensor development, TrAC Trends in Analytical Chemistry, 24 (2005) 37-48.

[47] S.S. Pathak, A. Sharma, A.S. Khanna, Value addition to waterborne polyurethane resin by silicone modification for developing high performance coating on aluminum alloy, Progress in Organic Coatings, 65 (2009) 206-216.

[48] S.A. Furman, F.H. Scholes, A.E. Hughes, D. Lau, Chromate leaching from inhibited primers - Part II: Modelling of leaching, Progress in Organic Coatings, 56 (2006) 33-38.

[49] K. Bonnel, C. Le Pen, N. Pébère, E.I.S. characterization of protective coatings on aluminium alloys, Electrochimica Acta, 44 (1999) 4259-4267.

[50] S. Sellaiyan, A.E. Hughes, S.V. Smith, A. Uedono, J. Sullivan, S. Buckman, Leaching properties of chromate-containing epoxy films using radiotracers, PALS and SEM, Progress in Organic Coatings, 77 (2014) 257-267.

[51] W. Zhang, Formation and corrosion inhibition mechanisms of chromate conversion coatings on aluminum and AA2024-T3, PhD thesis, The Ohio State University, 2002.

[52] R. Grilli, M.A. Baker, J.E. Castle, B. Dunn, J.F. Watts, Corrosion behaviour of a 2219 aluminium alloy treated with a chromate conversion coating exposed to a 3.5% NaCl solution, Corrosion Science, 53 (2011) 1214-1223.

[53] G.M. Brown, K. Shimizu, K. Kobayashi, G.E. Thompson, G.C. Wood, The morphology, structure and mechanism of growth of chemical conversion coatings on aluminium, Corrosion Science, 33 (1992) 1371-1385.

[54] K. Hladky, L.M. Callow, J.L. Dawson, Corrosion rates from impedance measurements: an introduction, British Corrosion Journal, 15 (1980) 20-25.

3. NON-IDEAL IMPEDANCE RESPONSE INFLUENCED BY THE VARIABILITY OF THE RANDOM DISTRIBUTION OF PHYSICAL PROPERTIES FOR COATED MATERIALS IN TWO-DIMENSIONAL SPACE

The impedance response in the real electrochemical system typically shows a depressed semicircle in the Nyquist plot compared to the response in an ideal electrical circuit. The behaviors of the distorted semicircle may be attributed to the surface roughness, heterogeneous bulk properties of composite coating systems, or various reaction rates on an electrolyte/metal interface. In this research, the two-dimensional impedance model incorporating with the distribution of physical properties was proposed to understand the non-ideal responses of dry coatings. Steady-state conditions were assumed in this model and the coefficient of variation (CV) of physical variables including electrical conductivity and permittivity were considered in the system consisting of a thin film on a metal surface. The probabilistic approach technique known as Copula has been employed to simulate a wide range of electrical properties of the coated material. The results indicated how the varied distributions of local impedance segments, formed by inter-correlated physical properties, result in the non-ideal impedance response. The quantitative understanding of the impedance signal changes triggered by normally or log-normally correlated variables was achieved by aspect ratio and characteristic frequency of impedance spectra. According to the 2D Impedance model, log-normally distributed electrical properties well-represented the distorted semicircle of impedance response compared to the normally distributed one. The aspect ratio and characteristic frequency of impedance spectra based on various CV values responded more sensitively to log-normal permittivity than to log-normal electrical conductivity. Additionally, more positive linear correlation between log-normal electrical conductivity and log-normal permittivity was observed in a greater value range of aspect ratio, resulted in more ideal impedance spectra. Lastly, the heterogeneity in electrical properties was represented not only by CV values of each electrical property, but also from correlation coefficients between electrical conductivity and z-direction position, and the highest aspect ratio of impedance spectra was obtained at 0 correlation coefficient which meant that the electrical conductivity was randomly distributed over the z-direction space. This research will not only be used as a novel method to interpret the various physical meanings of coating systems such as black boxes through impedance spectra, but also as an important guideline for optimal design of coating materials through the analysis.

3.1. Introduction

In order to further extract and interpret the superimposed meaning of impedance spectra through the physical distributions such as electrical properties and pore fraction in space, more than one-dimensional analysis was required. In chapter 2, the author proposed a deterministic and probabilistic 2D impedance model to understand the overall electrochemical activities and the influence of pore distribution to the corroding system by incorporating the probability density function on a multilayered composite coating system [1]. The various degradation mechanisms such as electrolyte-uptake process and self-healing process providing repassivation of an oxide layer that can be obtained from impedance spectra were analyzed through the developed 2D impedance model. For simplicity, the firstly developed 2D impedance model was assumed to have the homogeneous electrical properties for local elements, such as material segments and CPEs, and such assumption did not allow an interpretation of impedance spectra response by varied local distribution of electrical properties in 2D domain.

Since the material's local physical properties influence the impedance responses at various frequencies, this implies that the complex impedance values over a wide frequency range could be considered as the statistically correlated random variables between physical properties. Thus, a system that can control multivariable is needed to describe the dependence between random variables, such as electrical conductivity and permittivity, and to show various distribution effects of the parameters, which could be represented as a multi-dimensional joint cumulative distribution function, Copula. The use of copula to estimate non-normally distributed random multivariable has been considered as a feasible method for many real world problems such as risk assessment in finance studies [2, 3], hydrology [4-6], climate [7], reliability [8, 9], and fuel cell [10]. The application of copula concept on 2D domain of a material has a practical merit which can be observed in a probabilistic manner on a particular impedance characteristic as the copula function itself is a cumulative distribution function. This approach is a pioneering attempt to apply jointly multivariate physical properties to the field of research for analytical impedance response.

This paper is organized to generate the correlated random variables for the distribution of local segment properties on a 2D coating material and to discuss the response of complex impedance values by using statistical probability distributions of electrical properties. We will understand the response of non-ideal impedance through the probabilistically distributed electrical properties on the 2D dry coating.

3.2. Control Process of Two-dimension Impedance Model with Multivariate Random Variables

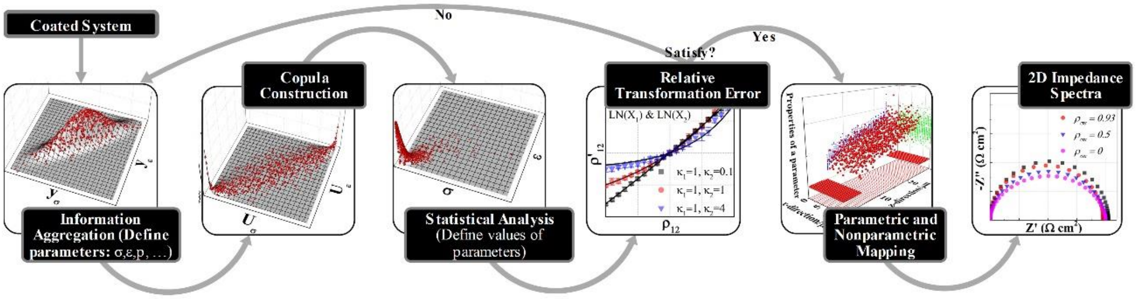

Figure 3.1 Schematic representation of the complete 2D impedance model and multivariate control process.

Three important points can be considered in carrying out this research. The first is to design the heterogeneously distributed physical properties to researcher's intention, then put the information of the properties into the two-dimensional plane, and finally interpret the impedance spectra through the plane with the given information. A methodological summary of the study is shown in Fig. 3.1. The information of the variables including electrical and spatial properties need to be defined in order to provide the localized information of the designed coating system. To assemble the given information of the variables, the information of each local segment of the coated material has to be given through correlating between each property pair. The aggregated information is then transformed into the desired real value domain and the error of the transformation is measured. After transformation, the parametric properties including electrical conductivity and permittivity are mapped to non-parametric properties with spatial information. The two-dimensional impedance response is calculated and interpreted with the coated material domain where each information is stored and designed.

3.2.1. Distribution of Physical Properties

3.2.1.1. Information Aggregation

It is important to define localized electrical properties and corresponding spatial information to interpret non-ideal impedance spectra. In this study, the electrical properties are considered as electrical conductivity and permittivity that are directly related to the impedance response. Pore fraction can also be defined as another variable, with an assumption that the distribution of electrical conductivity has a direct impact on the distribution of pores at each local segment in the organic coating. A variety of pores can be introduced in polymeric matrix due to application speed of coating, curing time and temperature, and additive concentration [11]. Considering this situation of pore generation in two-dimensional coating design, various pores that correlated to the distributed electrical properties can also be placed in space accordingly. For example, in a non-conductive polymeric matrix, the greater the amount of pore in a particular localized region, the lower the effective conductivity is expected to be. However, because this study observes changes in the impedance signal that reacts in a dry coating condition, the pore fraction as a variable of 2D impedance model, which may directly related to the electrolyte uptake process, is not addressed.

Finally, the location parameters of *x* and *z* as the spatial information are defined for forming the 2D domain. Each electrical property data symbolized a localized segment of the coated material and formed a set together with specific spatial information. Meanwhile, a representative control technique is required for the set. In this study, we use the standard normal distribution, which is easy to control and define variables. The variables of each other can be correlated or randomly matched. A mathematical approach is attempted to analyze the response of the impedance using correlated physical parameters, resulting in a better understanding of its physical meaning.

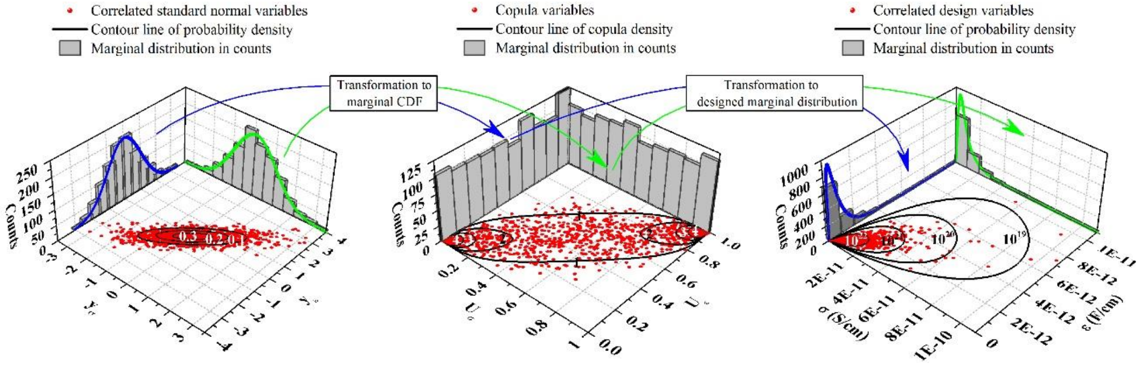

Figure 3.2 Gaussian copula approach using inverse Nataf transformation.

3.2.1.2. Inverse Nataf Transformation

Designing multivariate random variables in 2D domain is carried out using the inverse Nataf transformation which applies 1) linear transformation to transform independent standard normal variables into correlated standard normal variables and 2) the Gaussian copula to transform the correlated standard normal variables into correlated design variables as described in Fig. 3.2. To begin with, we assume a m-dimensional uncorrelated standard normal random vector $\mathbf{U}$ with domain $\mathbf{R}$ and a positive definite correlation matrix $\boldsymbol{\rho}_\mathbf{0}$ of the correlated standard normal variables $\mathbf{Y}$. Linear transformation from $\mathbf{U}$ to $\mathbf{Y}$ using $\boldsymbol{\rho}_\mathbf{0}$ can be performed by following linear equation [8].

$$\mathbf{Y} = \mathbf{L_0 U} + \mathbf{L_1} \tag{3.1}$$

Since both $\mathbf{Y}$ with the correlation matrix $\boldsymbol{\Sigma}_\mathbf{Y}/\boldsymbol{\sigma}_{\boldsymbol{Y}}^{\mathbf{2}} = \boldsymbol{\rho}_\mathbf{0}$ and $\mathbf{U}$ with covariance matrix $\boldsymbol{\Sigma}_\mathbf{U} = \boldsymbol{I}$ follow $\boldsymbol{N}(\mathbf{0}, \boldsymbol{I})$, the $\mathbf{L_1}$ can be obtained from the mean of $\mathbf{Y}$, $\mathbf{E}[\mathbf{Y}]$.

$$\mathbf{E}[\mathbf{Y}] = \mathbf{L_0 E}[\mathbf{U}] + \mathbf{L_1} = \mathbf{L_1} = \mathbf{0} \tag{3.2}$$

Correlation matrix of $\mathbf{Y}$ can be also calculated as

$$\boldsymbol{\rho}_\mathbf{0} = \boldsymbol{\Sigma}_\mathbf{Y}/\boldsymbol{\sigma}_{\boldsymbol{Y}}^{\mathbf{2}} = \mathbf{cov}[\mathbf{Y}, \mathbf{Y}] = \mathbf{E}[(\mathbf{L_0 U})(\mathbf{L_0 U})^\mathbf{T}] = \mathbf{L_0} \boldsymbol{\Sigma}_\mathbf{U} \mathbf{L}_\mathbf{0}^\mathbf{T} = \mathbf{L_0} \mathbf{L}_\mathbf{0}^\mathbf{T} \tag{3.3}$$

$\mathbf{L_0}$ can be determined as a the lower triangular matrix from Cholesky factorization which decomposes into the upper and lower triangular matrix since the $\boldsymbol{\rho}_\mathbf{0}$ is positive definite as below [12].

$$\boldsymbol{\rho_0} = \boldsymbol{L_0}\boldsymbol{L_0^T} = \begin{bmatrix} l_{11} & 0 & \cdots & 0 \\ l_{12} & l_{22} & & 0 \\ \vdots & \vdots & \ddots & \vdots \\ l_{1m} & l_{2m} & \cdots & l_{mm} \end{bmatrix} \begin{bmatrix} l_{11} & l_{12} & \cdots & l_{1m} \\ 0 & l_{22} & & l_{2m} \\ \vdots & \vdots & \ddots & \vdots \\ 0 & 0 & \cdots & l_{mm} \end{bmatrix} = \begin{bmatrix} 1 & \rho_{12} & \cdots & \rho_{1m} \\ \rho_{12} & 1 & & \rho_{2m} \\ \vdots & \vdots & \ddots & \vdots \\ \rho_{1m} & \rho_{2m} & \cdots & 1 \end{bmatrix} \tag{3.4}$$

Second, a link is needed to change the correlated standard normal values to correlated design variables, which is the copula. The copula is defined as a multivariate cumulative distribution function (CDF) with standard marginal distributions. According to Sklar's theorem [13, 14], there exists a copula function C if we assume that random variables have marginal cumulative distributions. The joint distribution F_X of a m-dimensional random vector X can be expressed as a function of its nondecreasing cumulative marginal distribution functions $F_{X_1}(x_1), \dots, F_{X_m}(x_m)$, which can be defined as

$$F_X(x_1, \dots, x_m) = C\left(F_{X_1}(x_1), \dots, F_{X_m}(x_m)\right) \tag{3.5}$$

Where if $F_{X_i}(x_i)$ is continuous, C is unique. By using Sklar's theorem, the Gaussian copula, which is one of the most universal elliptical copulas and is also called as Nataf transformation, can be written as

$$F_X(x_1, \dots, x_m) = \Phi\left(\Phi^{-1}[F_{X_1}(x_1)], \dots, \Phi^{-1}[F_{X_m}(x_m)]\right) \tag{3.6}$$

Marginal transformation as the next step of inverse Nataf transformation is considered to transfer the margin of **Y** into the correlated design variables **X** by using

$$x_i = F_{X_i}^{-1}[\Phi(y_i)], i = 1, \dots, m \tag{3.7}$$

Therefore, using Equations (3.1) and (3.7), the relationship between the correlated design variables **X** and the uncorrelated standard normal random vector **U** can be calculated as

$$
\begin{aligned}
x_1 &= F_{X_1}^{-1}[\Phi(l_{11}u_1)] \\
x_2 &= F_{X_2}^{-1}[\Phi(l_{12}u_1 + l_{22}u_2)] \\
&\vdots \\
x_m &= F_{X_m}^{-1}[\Phi(l_{1m}u_1 + l_{2m}u_2 + \cdots + l_{mm}u_m)]
\end{aligned}
\tag{3.8}
$$

3.2.1.3. Design Guideline of the Gaussian Copula for Applicability

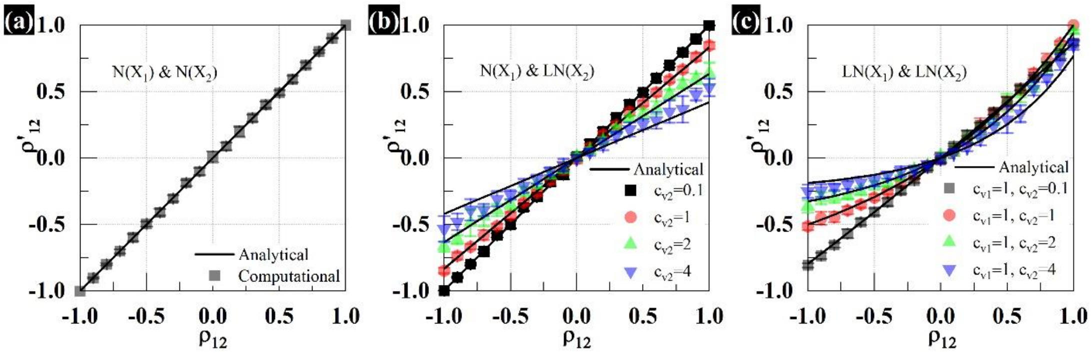

Figure 3.3 Relative error of inverse Nataf transformation between input correlation coefficient and reduced correlation coefficient according to the distribution types: (a) Normal and normal distributions. (b) Normal and log-normal distributions. (c) Log-normal and log-normal distributions.

A benefit of the Nataf transformation is that it can produce a joint CDF for various kinds of correlated desirable variables by accompanying a Gaussian copula. As a result, it is possible to solve the problem of 2D impedance with various types of correlated electrical properties as the variables. However, since the Gaussian copula can approximate more accurately the joint normal or lognormal CDFs compared to the other joint non-normal CDFs, the normal and log-normal distributions are used in this study to design the correlated desirable variables of electrical properties.

As the first case, consider two normal variables as $X_1 \sim N(\mu_1, \sigma_1^2)$ and $X_2 \sim N(\mu_2, \sigma_2^2)$. The exact joint normal PDF is given as

$$f_{X_1,X_2}(x_1, x_2) = \frac{1}{2\pi\sigma_1\sigma_2\sqrt{1-\rho_{12}'^2}} \times \exp\left\{-\frac{y_1^2 - 2\rho_{12}' y_1 y_2 + y_1^2}{2(1-\rho_{12}'^2)}\right\} \tag{3.9}$$

where $y_1 = \frac{x_1-\mu_1}{\sigma_1}$ and $y_2 = \frac{x_2-\mu_2}{\sigma_2}$. Differentiating the Gaussian copula described in Eq. (3.6) allows to obtain the approximate bivariate PDF:

$$\begin{aligned} \tilde{f}_X(x_1, x_2) &= \frac{\partial^2 C_\Phi}{\partial x_1 \partial x_2} = \frac{\partial^2 C_\Phi}{\partial y_1 \partial y_2} \cdot \frac{\partial y_1}{\partial x_1} \cdot \frac{\partial y_2}{\partial x_2} \\ &= \phi(y_1, y_2, \rho_{12}) \cdot \frac{f_{X_1}(x_1) f_{X_2}(x_2)}{\phi(y_1)\phi(y_2)} \end{aligned} \tag{3.10}$$

where $\frac{\partial^2 C_\Phi}{\partial y_1 \partial y_2} = \phi(y_1, y_2, \rho_{12})$ which is the joint normal PDF of Y_1 and Y_2, $\frac{\partial y_i}{\partial x_i} = \frac{f_{X_i}(x_i)}{\phi(y_i)}$, $\phi(y_i)$ is the normal PDF of Y_i, and $f_{X_i}(x_i)$ is the marginal PDF of X_i for $i = 1,2$. The $f_{X_1}(x_1)$ and $f_{X_2}(x_2)$ are given as

$$\begin{aligned} f_{X_1}(x_1) &= \frac{1}{\sigma_1\sqrt{2\pi}} \times \exp\left\{-\frac{1}{2}\left(\frac{x_1-\mu_1}{\sigma_1}\right)^2\right\} \\ f_{X_2}(x_2) &= \frac{1}{\sigma_2\sqrt{2\pi}} \times \exp\left\{-\frac{1}{2}\left(\frac{x_2-\mu_2}{\sigma_2}\right)^2\right\} \end{aligned} \tag{3.11}$$

The reduced correlation coefficient ρ_{12}' between X_1 and X_2 can be calculated from the input correlation coefficient ρ_{12} between the correlated standard normal variables Y_1 and Y_2

$$\rho'_{12} = \rho_{12} \tag{3.12}$$

There is no relative error of inverse Nataf transformation between ρ_{12} and ρ'_{12} as shown in Fig. 3.3(a). It is shown that the computational results generated in random manner are almost identical to the analytical result between tow normal variables in Eq. (3.12).

As a second case, when normal $X_1 \sim N(\mu_1, \sigma_1^2)$ and log-normal $X_2 \sim LN(\lambda_2, \xi_2^2)$ desirable random variables are given, the exact joint PDF of the mixed variables is expressed as

$$f_{X_1,X_2}(x_1, x_2) = \frac{1}{2\pi\sigma_1\xi_2\sqrt{1-\rho'_{12}}x_2} \times \exp\left\{-\frac{y_1^2 - 2\rho'_{12}y_1y_2 + y_1^2}{2(1-\rho'^2_{12})}\right\} \tag{3.13}$$

where $y_1 = \frac{x_1-\mu_1}{\sigma_1}$, $y_2 = \frac{\ln x_2 - \lambda_2}{\xi_2}$, $\xi_2 = \sqrt{\ln(1+(\sigma_2/\mu_2)^2)} = \sqrt{\ln(1+C_{v2}^2)}$, and $\lambda_2 = \ln\mu_2 - \frac{1}{2}\xi_2^2$. As explained in Eq. (3.10), the approximate normal-lognormal bivariate PDF can be calculated:

$$\begin{aligned} \tilde{f}_X(x_1, x_2) &= \phi(y_1, y_2, \rho_{12}) \cdot \frac{f_{X_1}(x_1) f_{X_2}(x_2)}{\phi(y_1)\phi(y_2)} \\ &= \frac{1}{2\pi\sigma_1\xi_2\sqrt{1-\rho_{12}^2}x_2} \times \exp\left\{-\frac{y_1^2 - 2\rho_{12}y_1y_2 + y_1^2}{2(1-\rho_{12}^2)}\right\} \end{aligned} \tag{3.14}$$

The $f_{X_1}(x_1)$ and $f_{X_2}(x_2)$ are given as

$$\begin{aligned} f_{X_1}(x_1) &= \frac{1}{\sigma_1\sqrt{2\pi}} \times \exp\left\{-\frac{1}{2}\left(\frac{x_1-\mu_1}{\sigma_1}\right)^2\right\} \\ f_{X_2}(x_2) &= \frac{1}{\xi_2 x_2\sqrt{2\pi}} \times \exp\left\{-\frac{1}{2}\left(\frac{\ln x_2 - \lambda_2}{\xi_2}\right)^2\right\} \end{aligned} \tag{3.15}$$

The reduced correlation coefficient between the normal and log-normal variables is obtained as below [8].

$$\rho'_{12} = \frac{\sqrt{\ln(1 + c_{v2}^2)}}{\kappa_2} \rho_{12} \tag{3.16}$$

Thus, the Gaussian copula can allow for a comparison between the exact joint PDF of normal-lognormal variables and the approximate normal-lognormal bivariate PDF in the 2D case. Depending on the c_{v2} value, the value of the correlation coefficient changes during the inverse Nataf transformation. As the c_{v2} value gets smaller, the values of reduced correlation coefficient and the input correlation coefficient become similar as shown in Fig. 3.3(b).

In the last case, when the two log-normal variables, $X_1 \sim LN(\lambda_1, \xi_1)$ and $X_2 \sim LN(\lambda_2, \xi_2)$, are considered, the exact joint lognormal PDF is given as

$$f_{X_1,X_2}(x_1, x_2) = \frac{1}{2\pi\xi_1\xi_2\sqrt{1 - \rho_{12}^2}x_1x_2} \times \exp\left\{-\frac{y_1^2 - 2\rho_{12}y_1y_2 + y_2^2}{2(1 - \rho_{12}^2)}\right\} \tag{3.17}$$

where $y_i = \frac{\ln x_i - \lambda_i}{\xi_i}$, $\xi_i = \sqrt{\ln(1 + c_{vi}^2)}$ and $\lambda_i = \ln \mu_i - \frac{1}{2}\xi_i^2$ for $i = 1,2$. The approximate joint PDF of the two log-normal variables can be determined by differentiating the Gaussian copula

$$\begin{aligned} \tilde{f}_X(x_1, x_2) &= \frac{f_{X_1}(x_1) \cdot f_{X_2}(x_2)}{\phi(y_1) \cdot \phi(y_2)} \phi(y_1, y_2, \rho'_{12}) \\ &= \frac{1}{2\pi\xi_1\xi_2\sqrt{1 - \rho_{12}'^2}x_1x_2} \times \exp\left\{-\frac{y_1^2 - 2\rho'_{12}y_1y_2 + y_2^2}{2(1 - \rho_{12}'^2)}\right\} \end{aligned} \tag{3.18}$$

The relationship between the reduced correlation coefficient and input correlation coefficient for the log-normal variables is expressed as follows.

$$\rho'_{12} = \frac{-1 + \exp\left\{\rho_{12}\sqrt{ln(1 + c_{v1}^2) \cdot ln(1 + c_{v2}^2)}\right\}}{c_{v1}c_{v2}} \tag{3.19}$$

As described in Fig. 3.3(c), it shows that there is a limitation in design during the inverse Nataf transformation between the two log-normal distributions. It is recommended that the correlation value is converted to bijective response between desirable correlation value ranges. However, for negative input correlation coefficient between -1 and 0, as the c_{v2} value increases, the design limit of the reduced correlation coefficient increases. For example, if the c_{v1} value is 1 and the c_{v2} value is 1, the reduced correlation coefficient, which is actually designed by transformation, is about -0.5 when input correlation coefficient is -1. This states that the reduced correlation coefficient value less than -0.5 cannot be designed under the aforementioned conditions, and it also implies that the negative correlation relationship by inverse Nataf transformation may indicate that there is a limit for designing the electrical properties. From the perspective of designing the properties of coating material, when a high electrical conductivity electrolyte solution penetrates into the coating, the electrical resistance of wet coating generally decreases, and the capacitance tends to rise [15]. Two electrical properties such as electrical resistivity and permittivity is apt to have a negative correlation. In order to design the desired correlation value through the inverse Nataf transformation, it is necessary to define variables with positive correlation relationship. Therefore, in this study, the electrical conductivity that inversely related to electrical resistivity is defined as the electrical property of the local segment on behalf of the electrical resistivity.

As shown in Fig. 3.4, the transformation relationship is explored in more detail according to the various c_{v1} and c_{v2} values following the log-normal distribution in the positive correlation. The range of c_{v1} and c_{v2} values for designing a desirable correlation value from 0 to 0.99 or higher with latter highlighted as yellow area, where the zone represents the more successful bijective responses. Correlation of 0 can be designed by the inverse Nataf transformation, regardless of c_{v1} and c_{v2} values, but the values close to correlation of 1 can be obtained only at certain c_{v1} and c_{v2} values. As described in Fig. 3.4, the closer the ratio of c_{v1} to c_{v2} is to 1, the less loss of information is found through the inverse Nataf transformation. In addition, when the c_v value is less than 1, there is less information loss due to the transformation than when the c_v value is greater than 1.

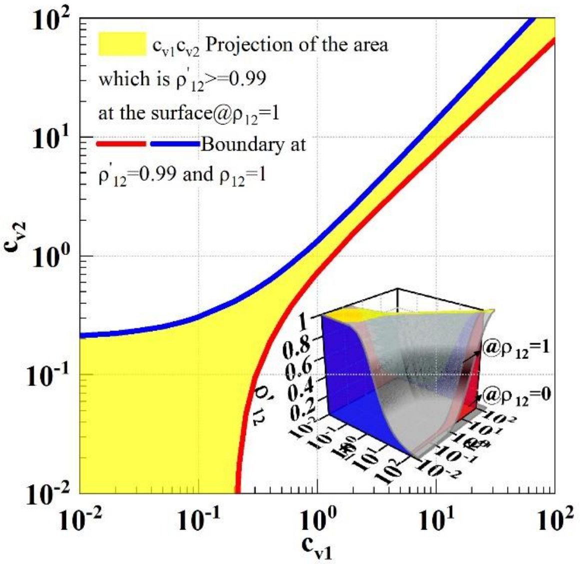

Figure 3.4 Orthographic projection plot on c_{v1} c_{v2}-plane for bijective conversion designing variable values by lognormal distributions.

3.2.2. Non-parametric Mapping

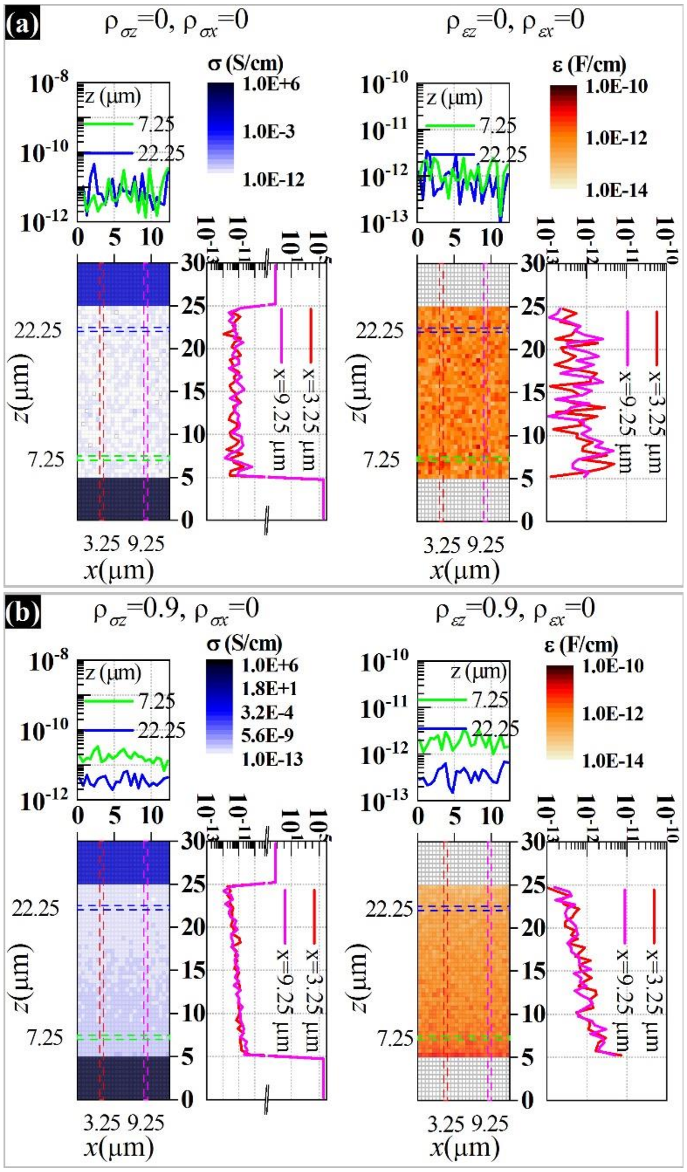

Figure 3.5 Two-dimensional non-parametric mapping by correlation: (a) The random distributions of σ and ε in all directions. (b) The random distribution of σ and ε in the x-direction and the distribution according to size of σ and ε in the z-direction.

The variables with physicoelectrical properties are transformed into a distribution with real values through the inverse Nataf transformation. Non-parametric mapping, which maps spatial information to a 2D plane, should be performed to distribute the physicoelectrical values into the coated domain. The spatial information does not have a specific distribution like the distribution of parametric properties in the real values but it has a one-to-one correspondence with the coordinate information in the coated domain. The one-to-one matching is performed using cumulative distribution data arranged in the copula densities of x and z. Fig. 3.5 shows the distributions of electrical conductivity and permittivity correlated with x and z positions through non-parametric mapping. A correlation value between spatial information and physical property of 0 means a random distribution of properties in Fig. 3.5(a). The closer the correlation value is to 1 or -1, the more linear change of the physical properties according to the position change is found. As described 0.9 correlation between electrical properties and z position in Fig. 3.5(b), the electrical properties tend to decrease with the increase in the z direction.

3.2.3. Two-dimensional Impedance Calculation

A single-layered system comprising electrolyte, coating, and metal substrate is designed for studying the impedance response by distribution of electrical properties in a probabilistically 2D space. A numerical element design is considered by using a single coating strategy. Each local segment of the designed domain with its own electrical conductivity and dielectric constant, is assumed to have isotropic electrical properties and steady state condition in this model. The capacitances and the resistances of local (j, i) element at z and x direction are defined as

$$C_{x(j,i)} = \varepsilon_{(j,i)} dz_j / dx_i \tag{3.20a}$$

$$C_{z(j,i)} = \varepsilon_{(j,i)} dx_i / dz_j \tag{3.20b}$$

$$R_{x(j,i)} = 1/\sigma_{(j,i)} \cdot dx_i / dz_j \tag{3.20c}$$

$$R_{z(j,i)} = 1/\sigma_{(j,i)} dz_j / dx_i \tag{3.20d}$$

where ε is permittivity, which is the product of dielectric constant and the free space permittivity, σ is electrical conductivity, and subscripts x and z describe x- and z-directions, respectively. An equivalent circuit analog at the elemental interface including the capacitance and electrical resistance of the segments is used to define for each local impedance. Fig. 3.6 illustrates the local impedance at the interface of the segments as physical property distribution of the coating system. The interfacial impedance between each segment is defined by the arithmetic-averaged impedance at the interface, which is expressed by the following equation:

$$Z_{(j,i\leftrightarrow j,i+1)} = \frac{R_{x(j,i)}/2}{1 + j\omega C_{x(j,i)} R_{x(j,i)}} + \frac{R_{x(j,i+1)}/2}{1 + j\omega C_{x(j,i+1)} R_{x(j,i+1)}} \tag{3.21a}$$

$$Z_{(j,i\leftrightarrow j+1,i)} = \frac{R_{z(j,i)}/2}{1 + j\omega C_{z(j,i)} R_{z(j,i)}} + \frac{R_{z(j+1,i)}/2}{1 + j\omega C_{z(j+1,i)} R_{z(j+1,i)}} \tag{3.21b}$$

where $Z_{(j,i\leftrightarrow j,i+1)}$ denotes localized impedance at the cell interface between the (j, i) element and the $(j, i + 1)$ element, and $Z_{(j,i\leftrightarrow j+1,i)}$ is localized impedance at the cell interface between the (j, i) element and the $(j + 1, i)$ element.

The 2D networks of local impedance at the interface of segments can be designed for the proposed coating system as shown in Fig. 3.6. The designed single layer coating system is divided into 60 x 25 segments. Each segment has 0.5 μm x 0.5 μm, and it is designed with 5, 20, and 5 μm thickness of the electrolyte, coating, and substrate, respectively. If it is assumed that there is no energy loss around a closed loop and no charge loss at a junction in a circuit, the Kirchhoff's laws which are based on energy conservation for any closed path ($\sum_{\circlearrowright} \Delta V = 0$) and charge conservation at any junction ($\sum i_{in} = \sum i_{out}$) can be applied on the 2D networks of local interfacial impedance. According to the boundary condition of the coating system, using local interfacial impedance and current density can then describe the sum of the potential difference in each closed path, which is achieved by Eq. (3.22)

$$\begin{pmatrix} \vdots & \vdots & \vdots & \vdots & \vdots & \vdots & \vdots & \vdots & \vdots & \vdots & \vdots & \vdots & \vdots & \vdots \\ 0 & \cdots & -Z_{1(j,i)} & \cdots & -Z_{2(j,i)} & Z_{(j,i)} & -Z_{3(j,i)} & \cdots & -Z_{4(j,i)} & \cdots & 0 & \cdots & 0 & 0 \\ \vdots & \vdots & \vdots & \vdots & \vdots & \vdots & \vdots & \vdots & \vdots & \vdots & \vdots & \vdots & \vdots & \vdots \\ 0 & \cdots & 0 & \cdots & 0 & 0 & 0 & \cdots & \cdots & \cdots & -Z_{1(n-1,m-1)} & \cdots & -Z_{2(n-1,m-1)} & Z_{(n-1,m-1)} \end{pmatrix} \begin{pmatrix} i_{1,1} \\ \vdots \\ i_{j-1,i} \\ \vdots \\ i_{j,i-1} \\ i_{j,i} \\ i_{j,i+1} \\ \vdots \\ i_{j+1,i} \\ \vdots \\ i_{n-2,m-1} \\ \vdots \\ i_{n-1,m-2} \\ i_{n-1,m-1} \end{pmatrix} = i_b \begin{pmatrix} \vdots \\ 0 \\ \vdots \\ Z_{4(n-1,m-1)} \end{pmatrix} \tag{3.22}$$

$$Z_{(j,i)} = Z_{(j,i\leftrightarrow j,i+1)} + Z_{(j,i+1\leftrightarrow j+1,i+1)} + Z_{(j+1,i\leftrightarrow j+1,i+1)} + Z_{(j,i\leftrightarrow j+1,i)} \tag{3.22a}$$

$$Z_{1(j,i)} = Z_{(j,i\leftrightarrow j,i+1)}$$

$$Z_{2(j,i)} = Z_{(j,i\leftrightarrow j+1,i)}$$

$$Z_{3(j,i)} = Z_{(j,i+1\leftrightarrow j+1,i+1)}$$

$$Z_{4(j,i)} = Z_{(j+1,i\leftrightarrow j+1,i+1)}$$

where $i_{j,i}$ denotes the electrical current density of the *(j,i)* loop. After the current density for each closed path is obtained from Eq. (3.22), a total impedance on 2D domain from the boundary loop ($\circlearrowright i_b$) could be given by

$$\begin{aligned} \mathrm{Z}_{total}(\omega) = l_x \Bigg\{ & \sum_{j=1}^{n-1} Z_{(j,1\leftrightarrow j+1,1)} + \sum_{i=1}^{m-1} Z_{(n,i\leftrightarrow n,i+1)} + Z_{b1} + Z_{b2} \\ & - \left(\sum_{j=1}^{n-1} Z_{(j,1\leftrightarrow j+1,1)} \cdot i_{j,1}/i_b + \sum_{i=1}^{m-1} Z_{(n,i\leftrightarrow n,i+1)} \cdot i_{n-1,i}/i_b \right) \Bigg\} \end{aligned} \tag{3.23}$$

$$Z_{b1} = \frac{R_{x(1,1)}/2}{1 + j\omega C_{x(1,1)} R_{x(1,1)}} \tag{3.23a}$$

$$Z_{b2} = \frac{R_{z(n,m)}/2}{1 + j\omega C_{z(n,m)} R_{z(n,m)}} \tag{3.23b}$$

where l_x is the system length in the x-direction.

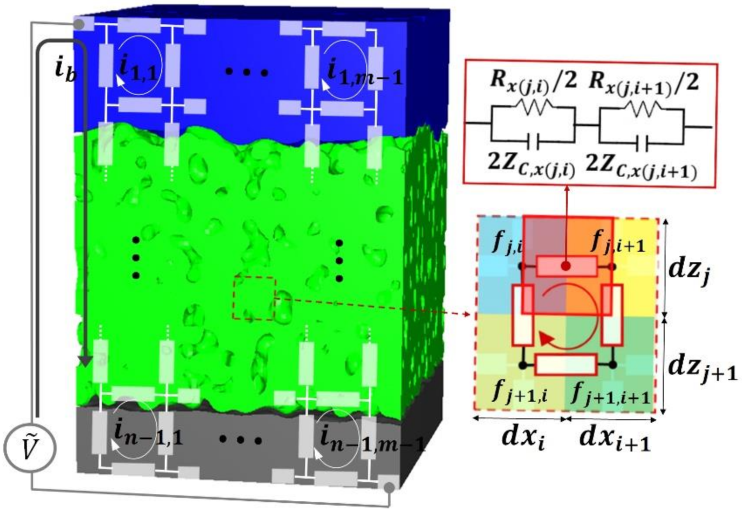

Figure 3.6 Schematic image of impedance element networks for two-dimensional impedance model.

3.3. Results and Discussion

Before the consideration of the effect by the various electrical property distributions in the 2D impedance model, a feasibility test is conducted to scrutinize whether the 2D calculation is reasonable. It is expected that the response of the 2D impedance model would correspond to that of the equivalent circuit model, if the electrical properties inside the coating between metal substrate and electrolyte are uniformly distributed. As shown in Fig. 3.7(a), electrical conductivity and permittivity are uniformly distributed within the coating. The values of electrical conductivity and permittivity are used $10^{-11}\ \Omega^{-1}\mathrm{cm}^{-1}$ and $10^{-12}\ \mathrm{F\ cm}^{-1}$, respectively. When the thickness ($l_{thickness}$) of the designed coating is $20\ \mu$m, the equivalent values of electrical resistance ($\mathrm{R_{eq}}$) and capacitance (C_{eq}) are calculated as follows

$$\mathrm{R_{eq}}A = l_{thickness}/\sigma = 2 \times 10^{8}\ \Omega\ \mathrm{cm}^2 \tag{3.24}$$

$$C_{\mathrm{eq}}/A = \varepsilon/l_{thickness} = 5 \times 10^{-10}\ F/\mathrm{cm}^2 \tag{3.25}$$

where A is a measurement area for normalization. As described in Bode and Nyquist plots of Fig. 3.7(b), it can be verified that impedance response of the electrical equivalent circuit consisting of a parallel combination of the electrical resistance component and the capacitor component is the same as the response of impedance through the 2D model. The impedance responses in both calculations show a perfect semicircle describing one time constant with a diameter of $200\ \mathrm{M\Omega\ cm^2}$ in the Nyquist domain. The result infers that an approach using the distribution of electrical properties along the local segments in x and z directions of the 2D impedance model is suitable for expressing the representative shape and value of the impedance response of the well-known bulk system. In other words, it shows an example of how the global phenomenon of the bulk system can be explained through the combination of the distributed local properties.

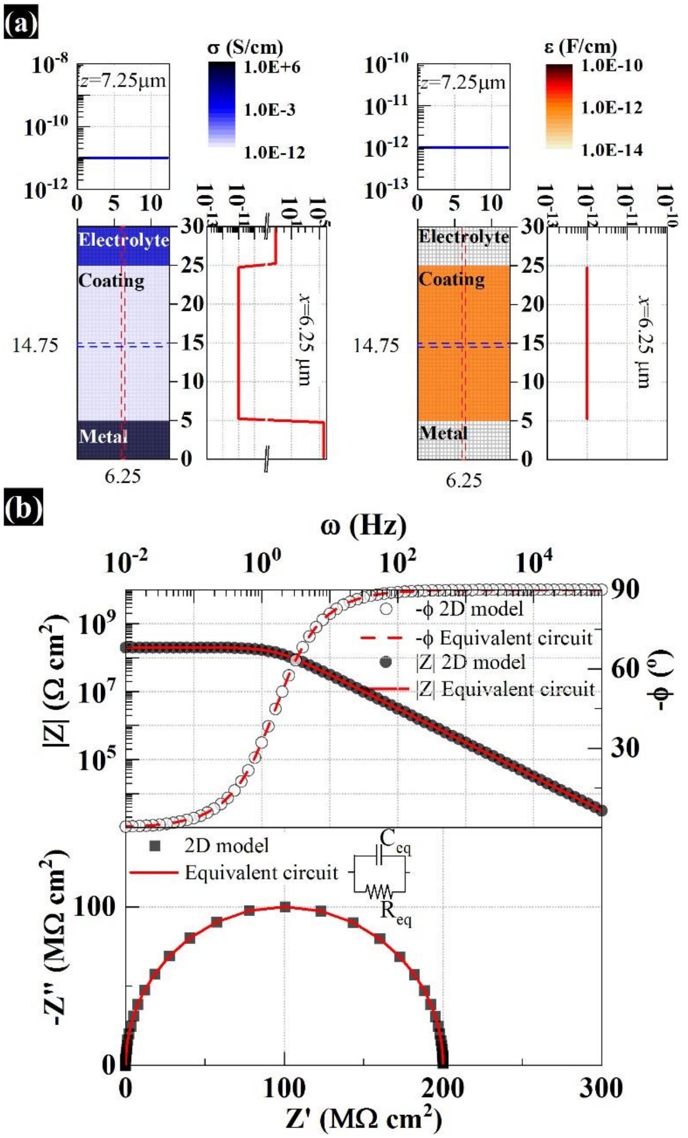

Figure 3.7 Impedance responses of electrical equivalent circuit model and two-dimensional impedance model at constant conductivity (σ=10^{-11} Ω^{-1} cm^{-1}) and permittivity (ε=10^{-12} F cm^{-1}) values: (a) Distribution of conductivity and permittivity in two-dimensional domain. (b) Bode and Nyquist plots.

The changes in impedance response according to the degree of heterogeneity in electrical properties are examined. Coefficient of variation (CV) value as relative standard deviation is used to represent heterogeneous characteristics of the electrical properties. CV is known as the ratio of the standard deviation to the mean. The large CV value indicates that the electrical properties are highly spread out from the mean value, and the larger the value, the more heterogeneous the electrical properties are dispersed. Fig. 3.8 shows the impedance response according to CV values when the electrical conductivity values are randomly distributed in the 2D domain that follows the normal distribution. To define the parametric properties such as electrical conductivity and permittivity inside the coating, the transformation through the relationship with the non-parametric properties such as x and z segment position are described in Fig. 3.8(a). The bivariate correlation coefficients between each properties are defined as zero, and the conversion to normal distribution by the inverse Nataf transformation indicates the correlation coefficient as -0.034, which is little difference between electrical conductivity and permittivity. In each CV case, it is statistically shown through 30 repeated calculations. To mathematically express the degree of distortion in the semicircle of the Nyquist plot, the aspect ratio of the semicircle is defined as the ratio of maximum length, b, in the y-imaginary axis direction to the maximum length, a, in the x-real axis direction as described in Fig. 3.8(b). The aspect ratio of 1 indicates a perfect semicircle, which is an ideal impedance response. The aspect ratio smaller than 1 means that the semicircle of impedance spectra is squeezed in Nyquist domain. A difficulty in designing CV values greater than 0.2 by physical boundary condition is illustrated in

Fig. 3.8(c). The histogram shown in the figure, describing the generation of electrical conductivity at the CV of 1, disobeys the physical boundary as it also generates negative values. Within the designed CV values, the impedance responses are almost unchanged and show almost perfect semicircles comparable to the ideal impedance behavior in a Nyquist domain. The smallest aspect ratio of 0.985 from 0.2 CV value near the design limit is observed. Thus, this implies that the electrical conductivity with normal distribution could not represent a non-ideal impedance behavior which describes a distorted semicircle in a Nyquist domain.

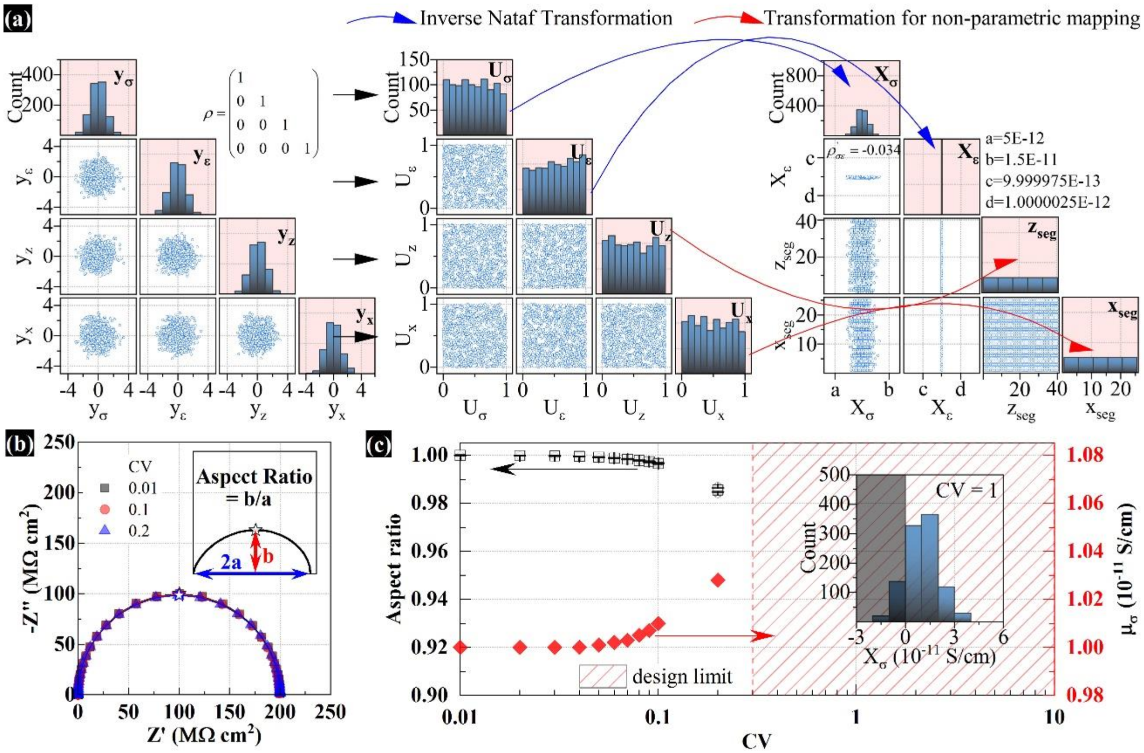

Figure 3.8 Impedance response on coefficient of variation of electrical conductivity following normal distribution at constant permittivity ($\mu_\varepsilon=10^{-12}$ F cm^{-1}, $CV_\varepsilon=10^{-7}$): (a) Random data generation through inverse Nataf transformation at 0.1 CV of electrical conductivity. (b) Nyquist plot. (c) Aspect ratio and average electrical conductivity vs CV.

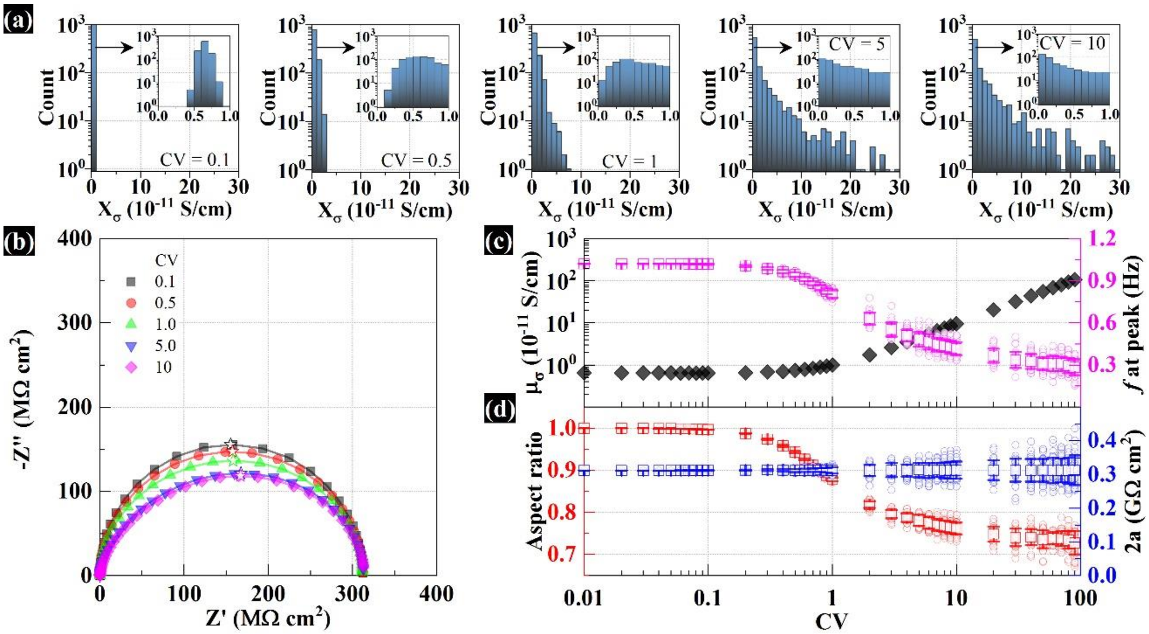

Figure 3.9 Impedance response according to the change of CV values of electrical conductivity following log-normal distribution at constant $\varepsilon=10^{-12}$ F cm^{-1}: (a) Electrical conductivity histogram according to CV value. (b) Nyquist plot. (c) Average electrical conductivity and characteristic frequency vs CV. (d) Aspect ratio and diameter of semicircle in the Nyquist plot vs CV.

Fig. 3.9 analyzes the impedance spectra that respond to the changes in CV values when electrical conductivity properties of local segments follow log-normal distribution. The bivariate correlation of each variable is randomly distributed to zero as shown in Fig. 3.8, and the permittivity of each segment is also designed to be almost constant as a mean of 10^{-12} F cm^{-1} with a very small standard deviation of 10^{-19} F cm^{-1}. 10 points per logarithmic decade between 100 and 0.01 are considered as CV values for electrical conductivity. The mean and standard deviation of the electrical conductivity from 30 repeated CV calculations are adjusted to equalize the average diameter of the semicircle in the Nyquist plot, so the effective electrical resistance of the bulk coating can be designed to be the same as indicated in Fig. 3.9(b) and 2a of Fig. 3.9(d). The histogram of electrical conductivity and the calculated average electrical conductivity values of the local segments inside the coating according to the CV values are illustrated in Fig. 3.9(a) and diamond-shaped black dots in Fig. 3.9(c), respectively. Aspect ratio values can be found to go down from 1 to approximately 0.72 as the CV value increases. This shows that the more heterogeneous the electrical conductivity of each segment, the greater the non-ideal impedance response is observed. However, as a CV value of electrical conductivity increases, it is noticeable that the aspect ratio does not become smaller than 0.7. The interfacial impedance between each local segment defined by a parallel configuration of RC elements in Eq. (3.21) is dominated by the capacitance value when the resistance value becomes relatively large. When the CV value of the electrical conductivity increases, a greater number of segments with smaller conductivity are observable as shown in Fig. 3.9(a). Since the impedance between local segments with relatively smaller conductivity is mainly dominated by a constant permittivity rather than conductivity or resistivity, it is possible to observe a lower plateau of the aspect ratio with high CV value, especially at CV greater than 10.

In addition, as shown in Fig. 3.9(d), the greater the CV value that indicates a more heterogeneous coating material, is expected to result in a greater deviation of the effective resistance value of the bulk system, represented as 2a, by the random distribution of the electrical conductivity values in the 2D domain. This is because the local segments with higher CV of electrical conductivity have more chance to form a variety of 2D random percolating networks in a coating system which possibly result in various effective resistance values. As shown in Fig. 3.9(c), characteristic frequency decreases as the CV value of the electrical conductivity increases. The characteristic frequency is the peak frequency which exhibits a maximum in negative imaginary impedance for a feature. The characteristic frequency of the impedance of local segment followed by a parallel configuration of RC elements is calculated as $1/2\pi RC$. As the CV value of the electrical conductivity increases, it can be expected that there are more segments with relatively small electrical conductivity that increase an average electrical conductivity, resulting in a decrease of the characteristic frequency of the coating system.

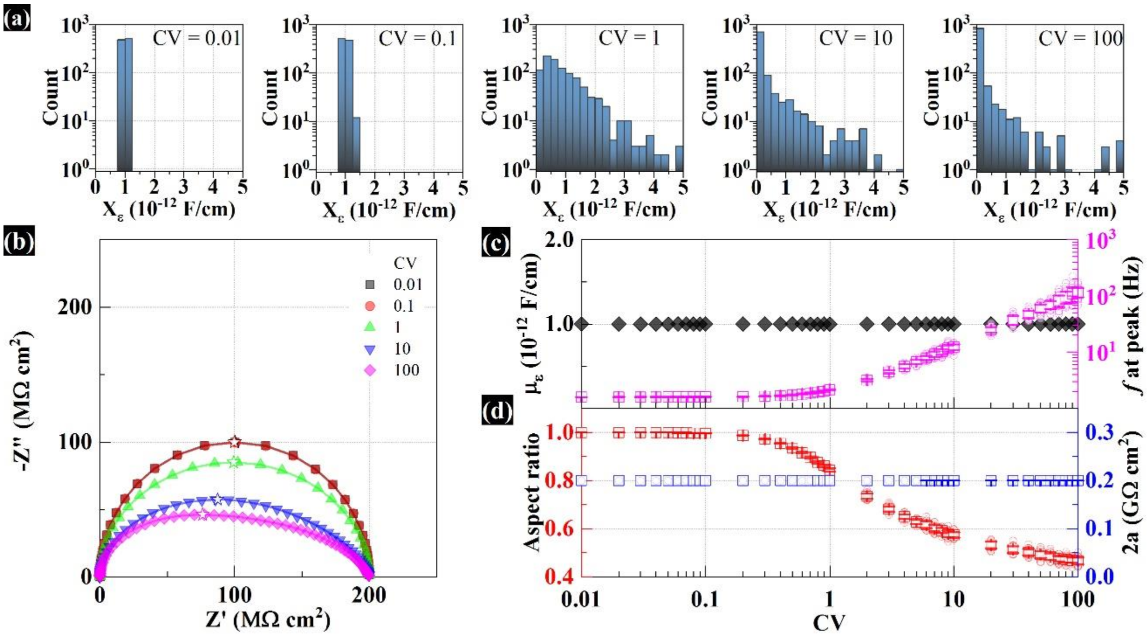

Figure 3.10 Impedance response according to the change of CV values of permittivity following log-normal distribution at constant $\sigma=10^{-11}$ S cm^{-1}: (a) Permittivity histogram according to CV value. (b) Nyquist plot. (c) Average permittivity and characteristic frequency vs CV. (d) Aspect ratio and diameter of semicircle in the Nyquist plot vs CV.

Fig. 3.10 describes the effect of the CV value changes of log-normal permittivity in the impedance response. The mean value of permittivity along the log-normal distribution is designed to be 10^{-12} F cm^{-1} in Fig. 3.10(c), and the electrical conductivity of each segment is maintained as 10^{-11} S cm^{-1}. All properties had a zero correlation coefficient. First of all, the aspect ratio decreases more sensitively with an increase of the permittivity CV value as shown in Fig. 3.10 (b), compared to the influence of the distribution of electrical conductivity. Fig. 3.10(d) indicates that the aspect ratio drops around 0.45 at the CV value of 100. The impedance of the local segment is inversely proportional to the permittivity value at constant conductivity. When the CV value of permittivity is increased, the impedance values of the local segments become more varied, resulting in a decrease of the aspect ratio. Secondly, unlike the changes by electrical conductivity distribution, the varied distribution of permittivity by different CV values does not affect the effective resistance value of coating, indicative of the semicircle diameter, as represented in 2a of Fig. 3.10(d). Finally, as discussed in Fig. 3.9, the frequency of local segment at peak is inversely proportional to the values of electrical resistivity and permittivity. As the CV value of permittivity increases, there are more segments with smaller permittivity values in Fig. 3.10(a), thereby the characteristic frequency of bulk system increases as shown in Fig. 3.10(c). Based on the results of the changes in characteristic frequency with respect to the CV values of electrical conductivity and permittivity, Fig. 3.9(c) and 3.10(c), the characteristic frequency of the coating system is more sensitive to changes in permittivity than to changes in electrical conductivity.

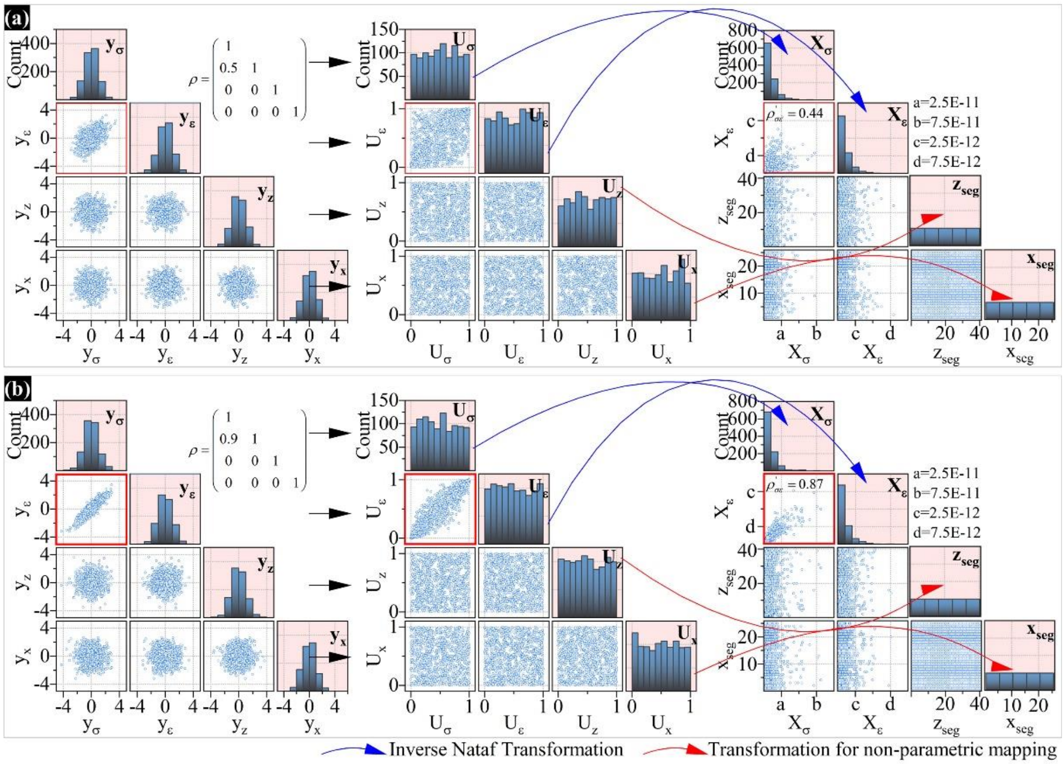

Figure 3.11 Random data generation through inverse Nataf transformation on different correlation coefficients between log-normal permittivity (μ_ε=10^{-12} F cm^{-1}, CV$_\varepsilon$=1) and log-normal electrical conductivity (μ_σ=10^{-11} S cm^{-1}, CV$_\sigma$=1): (a) $\rho_{\sigma\varepsilon}$=0.5. (b) $\rho_{\sigma\varepsilon}$=0.9.

To comprehend the influence of the statistical relationship between two variables on impedance spectra of the bulk system, random data are generated by the inverse Nataf transformation in Fig. 3.11. Difference correlation coefficients between log-normal permittivity and log-normal electrical conductivity are considered to design various relationships between the relative movements of the two variables. Figs. 3.11(a) and (b) describe scattered plots at 0.5 and 0.9 correlation coefficients between log-normal permittivity and log-normal electrical conductivity, respectively, and other bivariate correlation coefficients are considered as 0. As the scatter plots are shown in Fig. 3.11, the closer correlation coefficient gets to 1, the linear relationship positively becomes stronger. As can be seen from the result through the inverse Nataf transformation, when the CV values of two variables are 1, a transformation error of about 5-10% occurs between the input correlation coefficients and the reduced correlation coefficients.

Based on these transformations, the effect on impedance spectra for various reduced correlation coefficients between log-normal permittivity and log-normal electrical conductivity is studied in Fig. 3.12. The Fig. 3.12(a) shows the impedance spectra on the Nyquist domain according to the varied correlation coefficient when the CV values of both log-normal electrical conductivity and log-normal permittivity are 1. As the correlation coefficient between the two electrical variables approaches to 1, the impedance spectra close to the perfect semicircle can be seen through the Nyquist domain. In order to examine the correlation effect between the two electrical variables in detail, the aspect ratio is calculated through 30 iterations by changing the CV value of permittivity in Fig. 3.12(b). As can be seen from the calculation results, the aspect ratio increases as the reduced correlation coefficient increases. The impedance response of each local segment to frequency is represented by the ratio of permittivity and electrical conductivity. When the reduced correlation between two electrical variables becomes positively more linear, the differences of the ratio among local segments become small. Thus, it allows to represent homogeneous in terms of bulk systems and consequently results in the increased aspect ratio.

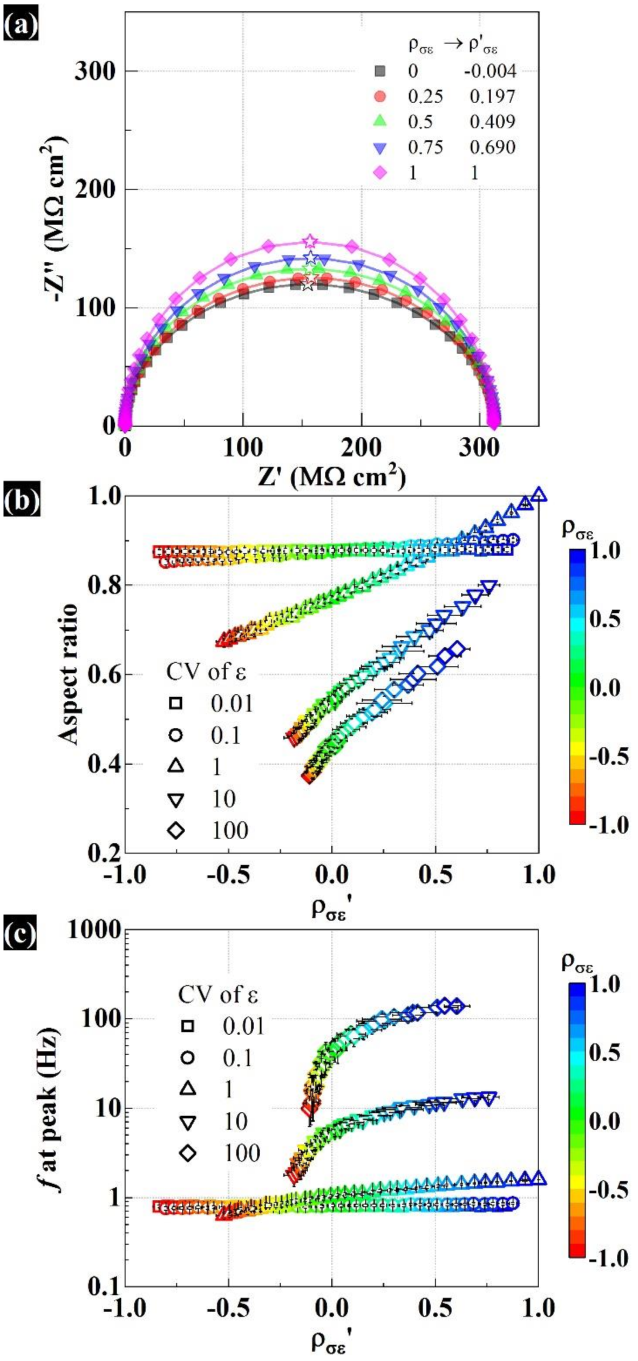

Figure 3.12 The effect of various correlation coefficients between log-normal permittivity ($\mu_\varepsilon=10^{-12}$ Fcm^{-1}) and log-normal electrical conductivity ($\mu_\sigma=10^{-11}$ Scm^{-1}, $CV_\sigma=1$) on impedance spectra: (a) Nyquist plot at $CV_\varepsilon=1$. (b) Aspect ratio vs reduced correlation coefficient. (c) Characteristic frequency vs reduced correlation coefficient.

In addition, as the CV value of permittivity increases, the slope between the change in aspect ratio and the change in reduced correlation coefficient also increases. This is indicative that the more heterogeneous the permittivity distribution is, the more various systems can be designed, depending on the electrical conductivity. The change in characteristic frequency according to the reduced correlation coefficient also shows a similar tendency to the change in the aspect ratio in Fig. 3.12(c). As the reduced correlation coefficient between log-normal electrical conductivity and log-normal permittivity increased, the characteristic frequency of the coating system tends to increase. As a result, a more positive linear relationship between the two variables results in a phase shift towards the higher frequencies with more ideal impedance spectra shape.

Finally, the impedance responses induced by the spatial distribution of the electrical properties for the local segments are studied. It is important to understand the impedance response to the bias distribution of the electrical properties because the distribution of pores may be biased during the curing process of the coating material [11]. Various correlation coefficients between log-normal electrical conductivity and z-direction position are considered to understand the impedance response of the coating system shown in Fig. 3.13. The electrical properties for each local segment are randomly generated through the inverse Nataf transformation at almost constant permittivity of $\mu_{\varepsilon} = 10^{-12}$ F cm^{-1} and $\mathrm{CV}_{\varepsilon} = 10^{-6}$ as illustrated in Fig. 3.13(a). As the absolute value of correlation coefficient between log-normal electrical conductivity and z-direction position approaches to 1, the electrical conductivity values are aligned in the z-direction according to the magnitude of the electrical conductivity. Alignment of the electrical conductivity in the z-direction by size indicates that it is heterogeneous in terms of bulk system, and the highest aspect ratio can be seen at the 0 correlation coefficient in Figs. 3.13(b) and (c). The 0 correlation coefficient between log-normal electrical conductivity and z-direction position describes that the properties of electrical conductivity are more randomly distributed thus showing more ideal impedance spectra of the coating system.

Aligning the electrical conductivity by magnitude in the z-direction forms an electrical network that relies on the percolation paths through low electrical conduction. Therefore, increasing the absolute value of the correlation coefficient increases the effective ohmic resistance of the bulk system. This phenomenon can be seen from the diameter of semicircle in Nyquist image of Fig. 3.13(b) and the result of 2a in Fig. 3.13(d). Additionally, the characteristic frequency results show that the spatial distribution of electrical conductivity exhibit a physical phenomenon similar to that occur from the change of the CV value of electrical conductivity in terms of the bulk system as the Fig. 3.13 (d) describes. The bulk coating system has the highest characteristic frequency at zero correlation coefficient between log-normal electrical conductivity and z-direction position which describes the more ideal impedance spectra and highest aspect ratio. This is because the linear distribution of electrical conductivity along the z-direction is more heterogeneous in the bulk coating system, and the lower characteristic frequency of the system is expressed as can be seen in high CV value of electrical conductivity. In terms of how heterogenous the distribution of local electrical conductivity is in the bulk coating system, the CV value of electrical conductivity and the correlation coefficient between electrical conductivity and z-direction position can have the same physical interpretation. Therefore, as the changes in aspect ratio and characteristic frequency according to the CV value of electrical conductivity are similar in Fig. 3.9, the distribution of electrical conductivity in space according to the correlation coefficient also describes the similar tendency between aspect ratio and characteristic frequency in Figs. 3.13(c) and (d).

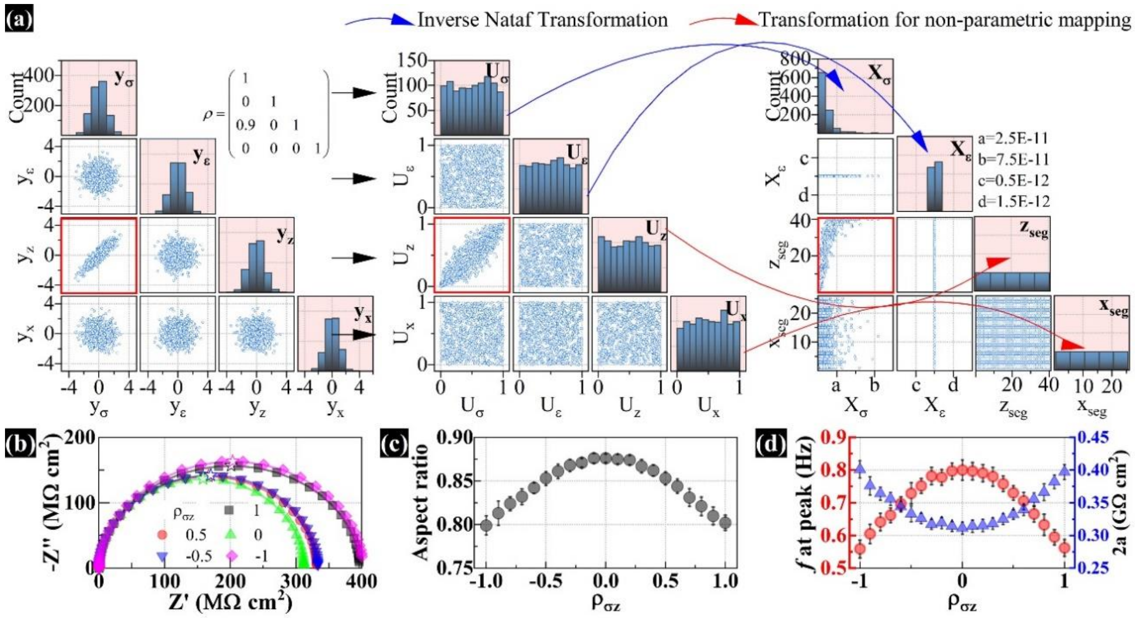

Figure 3.13 The effect of various correlation coefficients between log-normal electrical conductivity (μ_σ=10^{-11} S cm^{-1}, CV$_\sigma$=1) and z-direction position on impedance spectra: (a) Random data generation through inverse Nataf transformation at $\rho_{\sigma z}$=0.9 and μ_ε=10^{-12} F cm^{-1} and CV$_\varepsilon$=10^{-6}. (b) Nyquist plot. (c) Aspect ratio vs input correlation coefficient. (d) Characteristic frequency and diameter of semicircle in the Nyquist plot vs input correlation coefficient.

3.4. Summary

Through changing the distribution of local physical properties such as electrical conductivity and permittivity, the 2D impedance spectra that responses on the bulk coating system were studied. The multivariate random variables were controlled through the Copula, a statistical probabilistic approach, in order to provide inter-correlated information of the electrical properties to local segments inside the coating. To understand the non-ideal impedance spectra through various distributions of electrical properties in 2D space, the distortion of perfect semicircle of impedance spectra in the Nyquist domain was expressed through aspect ratio, and the changes in the characteristics of the coating system were described using characteristic frequency.

From the distribution type with a perspective of electrical conductivity, a normal distribution only allowed to show almost ideal impedance spectra due to design limitation, but the electrical conductivity along with log-normal distribution was possible to express the distorted response of impedance spectra with an aspect ratio of 0.7 or higher through various CV values of the electrical conductivity. The CV value described the degree of heterogeneity in the distribution of electrical properties. In addition, unlike the effect of log-normal electrical conductivity on the impedance spectra, the 2D impedance domain with log-normal permittivity showed continuous and more sensitive decrease of the aspect ratio as the CV value of permittivity increased because the interfacial impedance between each local segment was defined by the parallel configuration of the RC element. The results of characteristic frequency and aspect ratio illustrated that the variation in impedance spectra was more sensitive to log-normal permittivity compared to log-normal electrical conductivity.

Considering not only the CV value of electrical properties but also the correlation coefficient between electrical conductivity and z-direction position, it was confirmed that the degree of heterogeneity inside the coating also had an influence on the aspect ratio of the impedance spectra. As the electrical conductivity was aligned in z-direction according to its size, the smaller aspect ratio was calculated which represents more heterogeneous system under the perspective of bulk coating. Additionally, the correlation coefficient between the log-normal electrical conductivity and the log-normal permittivity on impedance spectra showed a greater influence on the characteristic frequency and the aspect ratio of impedance spectra when it got closer to the positive linear relationship between the two electrical properties.

3.5. References

[1] S. Cho, Y. Cubides, H. Castaneda, Probing the degradation mechanism of a Cr (VI) coating/aluminum alloy 2024-T3 system based on dynamic mechanisms and a 2D deterministic-probabilistic approach, Electrochimica Acta, 236 (2017) 82-96.

[2] W. Breymann, A. Dias, P. Embrechts, Dependence structures for multivariate high-frequency data in finance, Quantitative Finance, 3 (2003) 1-14.

[3] C.N. Haas, On modeling correlated random variables in risk assessment, Risk Analysis, 19 (1999) 1205-1214.

[4] B. Renard, M. Lang, Use of a Gaussian copula for multivariate extreme value analysis: some case studies in hydrology, Advances in Water Resources, 30 (2007) 897-912.

[5] C. Genest, A.-C. Favre, Everything you always wanted to know about copula modeling but were afraid to ask, Journal of Hydrologic Engineering, 12 (2007) 347-368.

[6] A. Bárdossy, S. Hörning, Gaussian and non-Gaussian inverse modeling of groundwater flow using copulas and random mixing, Water Resources Research, 52 (2016) 4504-4526.

[7] C. Schölzel, P. Friederichs, Nonlinear processes in geophysics multivariate non-normally distributed random variables in climate research–introduction to the copula approach, Nonlinear Processes in Geophysics, 15 (2008) 761-772.

[8] Y. Noh, K. Choi, L. Du, Reliability-based design optimization of problems with correlated input variables using a Gaussian copula, Structural and Multidisciplinary Optimization, 38 (2009) 1-16.

[9] X.-S. Tang, D.-Q. Li, C.-B. Zhou, L.-M. Zhang, Bivariate distribution models using copulas for reliability analysis, Proceedings of the Institution of Mechanical Engineers, Part O: Journal of Risk and Reliability, 227 (2013) 499-512.

[10] B.M. Boshkoska, P. Boškoski, A. Debenjak, Đ. Juričić, Dependence among complex random variables as a fuel cell condition indicator, Journal of Power Sources, 284 (2015) 566-573.

[11] V. Lavaert, M. De Cock, M. Moors, E. Wettinck, Influence of pores on the quality of a silicon polyester coated galvanised steel system, Progress in Organic Coatings, 38 (2000) 213-221.

[12] N.J. Higham, Cholesky factorization, Wiley Interdisciplinary Reviews: Computational Statistics, 1 (2009) 251-254.

[13] R.B. Nelsen, An introduction to copulas, Springer Science & Business Media, 2007.

[14] C. Schoelzel, P. Friederichs, Multivariate non-normally distributed random variables in climate research–introduction to the copula approach, Nonlinear Processes in Geophysics, 15 (2008) 761-772.

[15] V. Mišković-Stanković, D. Dražić, M. Teodorović, Electrolyte penetration through epoxy coatings electrodeposited on steel, Corrosion Science, 37 (1995) 241-252.

4. LOCALIZED ELECTROCHEMICAL TWO-DIMENSIONAL IMPEDANCE MODEL

In this study, the localized impedance spectra, which describe electrical and electrochemical phenomena in the local area of a coated material, are analyzed by modifying the boundary conditions of the 2D impedance model developed in previous studies. The correlation between the local location of the measuring electrode probe and the actual measurement area is verified through the normalized current distribution flowing into the coating material when measuring the local area. In local measurement, the physical meaning of local impedance spectra by taking into account important parameters such as electrical conductivity of electrolyte solutions, the angular frequency of the applied measurement potential, and electrode probe location is understood.

4.1. Introduction

The global impedance spectra of the bulk system reflect the averaged combination of local electrical/electrochemical systems [1], but sometimes it failed to describe the macroscopic behavior of the bulk system due to dominant response through the internal defects or pinholes inside of the coating [2]. Hence, it is difficult to quantitatively understand the phenomenon of corrosion or coating degradation in the early stage from the global impedance perspective. In the case of the bulk system that is non-homogeneous depending on their spatial position from an electrical and electrochemical perspective, localized impedance data generated by bi-electrode probe methods [3-5], vibrating probe method [6], and micro-capillary-based methods [7] have often been used to understand the changes in the electrical and electrochemical properties on the local position of the system [8].

Changes in local systems under the electrolyte solution of low electrical conductivity were interpreted by localized impedance signal dependent on applied frequency [9]. Corrosion of steel under the defected organic coating and the degradation of the coating have been studied by localized electrochemical impedance spectroscopy (LEIS) [10, 11]. Local electrochemical impedance mapping was also utilized to scrutinize delamination phenomena at the steel/organic coating interface [12]. In most studies, the localized impedance spectra for in-situ monitoring were analyzed on the assumption that the spectra obtained through the experiment described the localized physicochemical phenomenon of the material surface close to the electrode probe [13-15].

However, the localized impedance spectrum, which is determined by the electrical current flow between the local measurements, varies in its meaning and interpretation depending on various measurement environmental conditions, such as electrical conductivities of electrolyte and coating materials and applied perturbation frequency. Balusamy and Nishimura have investigated local corrosion behavior of scratched epoxy coated steel according to various electrical conductivities of electrolyte solution by LEIS [16]. As the electrode probe moved away from the scratch, the obtained impedance spectra indicated different responses depending on the concentration of chloride in the electrolyte. Eckhard et al. have illustrated perturbation frequency-dependent impedance response for local corrosion sites [17]. From this result, it was evident that not only do appropriate frequencies exist for the localized impedance spectra to observe a particular phenomenon, but also the physical meaning of each frequency is different for local measurements. Therefore, it is necessary to know the confined area or local location of the macro-physicochemical system, which is measured according to the various environmental conditions mentioned above, in order to accurately interpret the local system through the localized impedance spectra.

In a previous study (Chapter 3), the global impedance response of the bulk system through the inter-correlated local physical properties inside coatings, that have electric and dielectric characteristics, was scrutinized by 2D impedance model with probabilistic approach. From the 2D impedance model which was represented by a combination of impedance values for each local segment, it can be expected that the local behavior of a electrochemical system is likely to be obtained if boundary conditions similar to that of a local experimental measurement is given. Using the 2D impedance model modified in this study, the physical meanings of impedance spectra responding to the local location of electrode probe, electrical conductivity of electrolyte, and applied frequency are examined in depth.

4.2. Localized 2D Impedance Model

Localized 2D impedance model is proposed by modifying the 2D impedance model developed in previous studies [18] for understanding global impedance behavior of bulk electrical and electrochemical systems. Since local electrical properties, such as electrical resistivity and permittivity, of each segment in the 2D domain are embedded, the information of each electrical property can be extracted by adjusting the input boundary condition of the 2D impedance model.

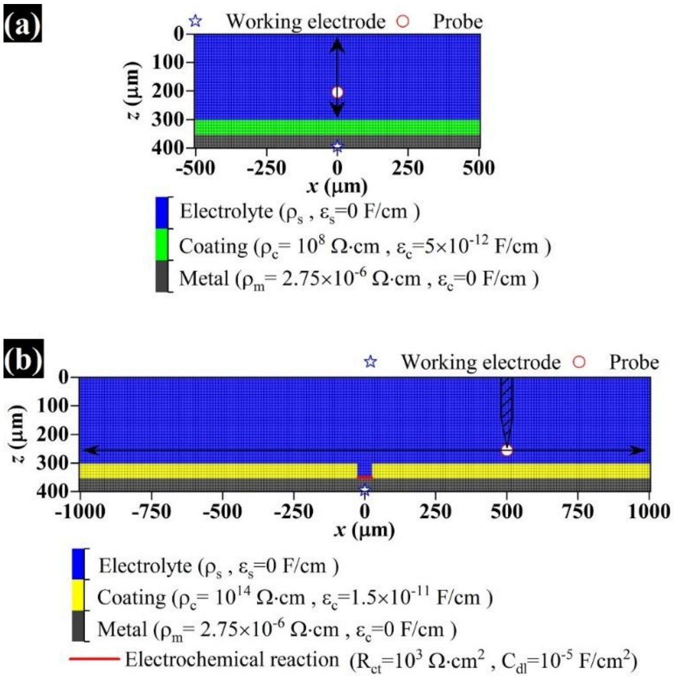

Figure 4.1 Schematic image of cross-sectional coating material on localized 2D impedance model: (a) Coating without defect. (b) Scratched coating.

In this study, the responses of localized impedance spectra are analyzed to two types of coating system, as shown in Fig. 4.1. The Fig. 4.1(a) is designed to observe the changes in impedance signal taking place in the homogeneous coating system without a defect. The electrochemical reaction is considered to be nonexistent because it forms a perfect barrier from the coating. The electrical resistivity of the electrolyte and the distance between the electrode probe and coating surface are used as manipulated variables. A single-layered system consisting of coating, electrolyte, and metal substrate was configured. The designed single layer coating system is divided into 40 x 101 segments. Each segment has 10 μm x 10 μm, and it is designed with 300, 50, and 50 μm thickness of the electrolyte, coating, and substrate, respectively. Fig. 4.1(b) is presented to analyze the response of localized impedance in coating materials that are locally damaged by mechanical scratch according to various electrical resistivity of electrolyte and x-position of electrode probe. The single-layered system with 50 μm of scratch width in the coating is constructed. The designed coating system is divided into 40 x 201 segments. The size of each segment and the thickness of each layer are designed exactly as mentioned in Fig. 4.1(a). Steady state condition and isotropic electrical properties, such as permittivity and electrical resistivity, are assumed for each local segment in this model. The resistances and capacitances at z and x directions of local (j, i) element are defined as

$$C_{x(j,i)} = \varepsilon_{(j,i)} dz_j / dx_i \tag{4.1a}$$

$$C_{z(j,i)} = \varepsilon_{(j,i)} dx_i / dz_j \tag{4.1b}$$

$$R_{x(j,i)} = \rho_{(j,i)} \cdot dx_i / dz_j \tag{4.1c}$$

$$R_{z(j,i)} = \rho_{(j,i)} dz_j / dx_i \tag{4.1d}$$

where ε is permittivity, which is the product of dielectric constant and the free space permittivity, ρ is electrical resistivity, and subscripts x and z describe x- and z-directions, respectively. An equivalent circuit analog at the elemental interface including the capacitance and electrical resistance of the segments is used to define for each local impedance. The interfacial impedance between each segment is defined by the arithmetic-averaged impedance at the interface, which is expressed by the following equation:

$$Z_{(j,i\leftrightarrow j,i+1)}=\frac{R_{x(j,i)}/2}{1+j\omega C_{x(j,i)}R_{x(j,i)}}+\frac{R_{x(j,i+1)}/2}{1+j\omega C_{x(j,i+1)}R_{x(j,i+1)}} \tag{4.2a}$$

$$Z_{(j,i\leftrightarrow j+1,i)}=\frac{R_{z(j,i)}/2}{1+j\omega C_{z(j,i)}R_{z(j,i)}}+\frac{R_{z(j+1,i)}/2}{1+j\omega C_{z(j+1,i)}R_{z(j+1,i)}} \tag{4.2b}$$

where $Z_{(j,i\leftrightarrow j,i+1)}$ denotes localized impedance at the cell interface between the (j,i) element and the $(j,i+1)$ element, and $Z_{(j,i\leftrightarrow j+1,i)}$ is localized impedance at the cell interface between the (j,i) element and the $(j+1,i)$ element. ω denotes an angular frequency.

The interfacial impedance between segments that describes electrochemical reactions occurring at the interface can be affected by non-faradaic impedance such as electrochemical double layer as well as faradaic impedance, which is composed of the charge transfer impedance induced from the kinetics of the charge transfer reaction and diffusion. If electrochemical control processes such as charge transfer phenomenon take place on the localized cell interface between the metal substrate and the electrolyte in red line of Fig. 4.1(b), impedance at the interface can be defined by the following expressions.

$$\begin{aligned}\mathrm{Z}_{(\mathrm{j,i}\leftrightarrow\mathrm{j+1,i})}&=\frac{\mathrm{R}_{\mathrm{z(j,i)}}/2}{1+j\omega C_{z(j,i)}R_{z(j,i)}}+\frac{\mathrm{R}_{\mathrm{ct,z}}}{1+j\omega\mathrm{C}_{\mathrm{z,dl}}\mathrm{R}_{\mathrm{ct,z}}}\\&+\frac{\mathrm{R}_{\mathrm{z(j+1,i)}}/2}{1+j\omega C_{z(j+1,i)}R_{z(j+1,i)}}\end{aligned} \tag{4.3}$$

where C_{dl} is the capacitance of the double layer and R_{ct} is the charge transfer impedance. In this work, we assume that there is no diffusion phenomenon.

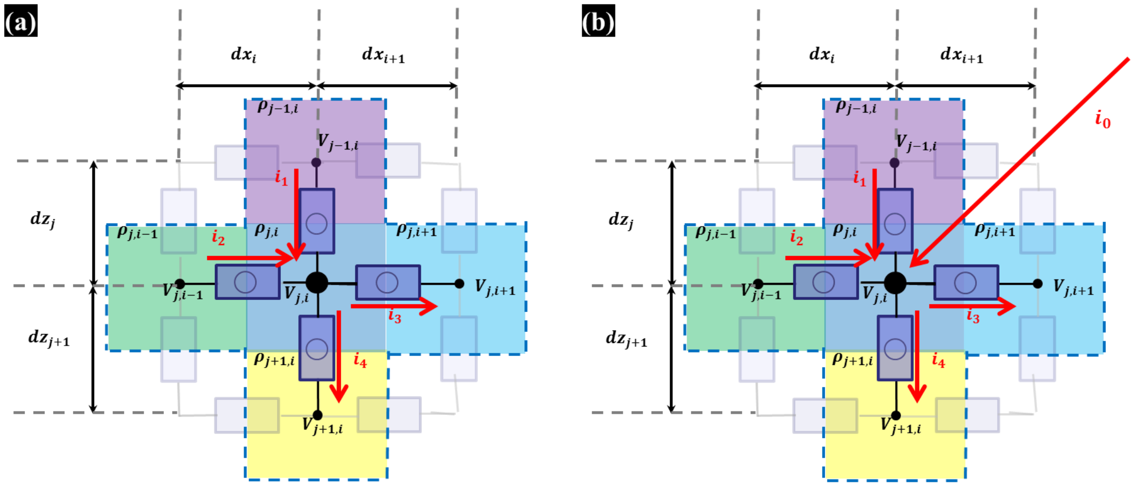

Figure 4.2 The schematic diagram for the 2D networks of local impedance at the interface of segments: (a) Without current source. (b) With current source at electrode probe.

The current is assumed to flow intensively through a probe tip near the surface of the coating material to account for localized phenomena. To concentrate the current flow without dissipation from the electrode probe in the electrolyte, point charge at input probe electrode segment is considered. The circuit of the designed system with input point charge source becomes a non-planar circuit which is drawn on a flat surface with at least one wire crossing. Thus, the modified two-dimensional impedance model for LEIS is calculated using junction rule which conserves total charges at each node instead of the loop rule which should identify a closed loop based on the conservation of energy. The 2D networks of local impedance at the interface of segments can be designed for the proposed coating system as shown in Fig. 4.2. If it is assumed that there is no charge loss at a junction in a circuit, the Kirchhoff's laws which is based on charge conservation at any junction ($\sum i_{in} = \sum i_{out}$) can be applied on the 2D networks of local interfacial impedance. Using local interfacial impedance and relative potential at each node can then describe that the sum of the current densities at each junction is zero.

$$
\begin{aligned}
& i_4 + i_3 - i_2 - i_1 = 0 \\
& \rightarrow -\left(\frac{1}{Z_{(j,i \leftrightarrow j-1,i)}}\right) V_{j-1,1} - \left(\frac{1}{Z_{(j,i \leftrightarrow j,i-1)}}\right) V_{j,i-1} \\
& + \left(\frac{1}{Z_{(j,i \leftrightarrow j-1,i)}} + \frac{1}{Z_{(j,i \leftrightarrow j,i-1)}} + \frac{1}{Z_{(j,i \leftrightarrow j,i+1)}}\right. \\
& \left. + \frac{1}{Z_{(j,i \leftrightarrow j+1,i)}}\right) V_{j,i} - \left(\frac{1}{Z_{(j,i \leftrightarrow j,i+1)}}\right) V_{j,i+1} \\
& - \left(\frac{1}{Z_{(j,i \leftrightarrow j+1,i)}}\right) V_{j+1,i} = 0
\end{aligned}
\tag{4.4}
$$

The square boundary of the 2D domain is given an insulating condition which is no current flow through the local interfacial impedance at the boundary. The conditions of inlet current in the electrode probe segment (in Fig. 4.2 (b)) and outlet current in the working electrode segment based on the conservation of charge can be express in Eq. (4.5) and Eq. (4.6), respectively.

$i_4 + i_3 - i_2 - i_1 = i_0$

$$\begin{aligned} &\rightarrow -\left(\frac{1}{Z_{(j,i\leftrightarrow j-1,i)}}\right)V_{j-1,1} - \left(\frac{1}{Z_{(j,i\leftrightarrow j,i-1)}}\right)V_{j,i-1} \\ &+ \left(\frac{1}{Z_{(j,i\leftrightarrow j-1,i)}} + \frac{1}{Z_{(j,i\leftrightarrow j,i-1)}} + \frac{1}{Z_{(j,i\leftrightarrow j,i+1)}}\right. \\ &\left. + \frac{1}{Z_{(j,i\leftrightarrow j+1,i)}}\right)V_{j,i} - \left(\frac{1}{Z_{(j,i\leftrightarrow j,i+1)}}\right)V_{j,i+1} \\ &- \left(\frac{1}{Z_{(j,i\leftrightarrow j+1,i)}}\right)V_{j+1,i} = i_0 \end{aligned} \tag{4.5}$$

$i_3 - i_2 - i_1 = -i_0 \because i_4 = 0\ (boundary\ condition)$

$$\begin{aligned} &\rightarrow -\left(\frac{1}{Z_{(j,i\leftrightarrow j-1,i)}}\right)V_{j-1,1} - \left(\frac{1}{Z_{(j,i\leftrightarrow j,i-1)}}\right)V_{j,i-1} \\ &+ \left(\frac{1}{Z_{(j,i\leftrightarrow j-1,i)}} + \frac{1}{Z_{(j,i\leftrightarrow j,i-1)}} + \frac{1}{Z_{(j,i\leftrightarrow j,i+1)}}\right)V_{j,i} \\ &- \left(\frac{1}{Z_{(j,i\leftrightarrow j,i+1)}}\right)V_{j,i+1} = -i_0 \end{aligned} \tag{4.6}$$

After the potential for each node is obtained from the equations defined by the conservation of energy in the junctions of all segments, a total impedance on 2D domain from input current density (i_0) and potential difference between CE/RE probe and WE probe could be given by

$$\mathrm{Z}_{total}(\omega) = l_e\left(\frac{V_{CE/RE\ probe} - V_{WE\ probe}}{i_0}\right) \tag{4.7}$$

where l_e is coating length exposed by electrolyte in the x-direction.

4.3. Results and Discussion

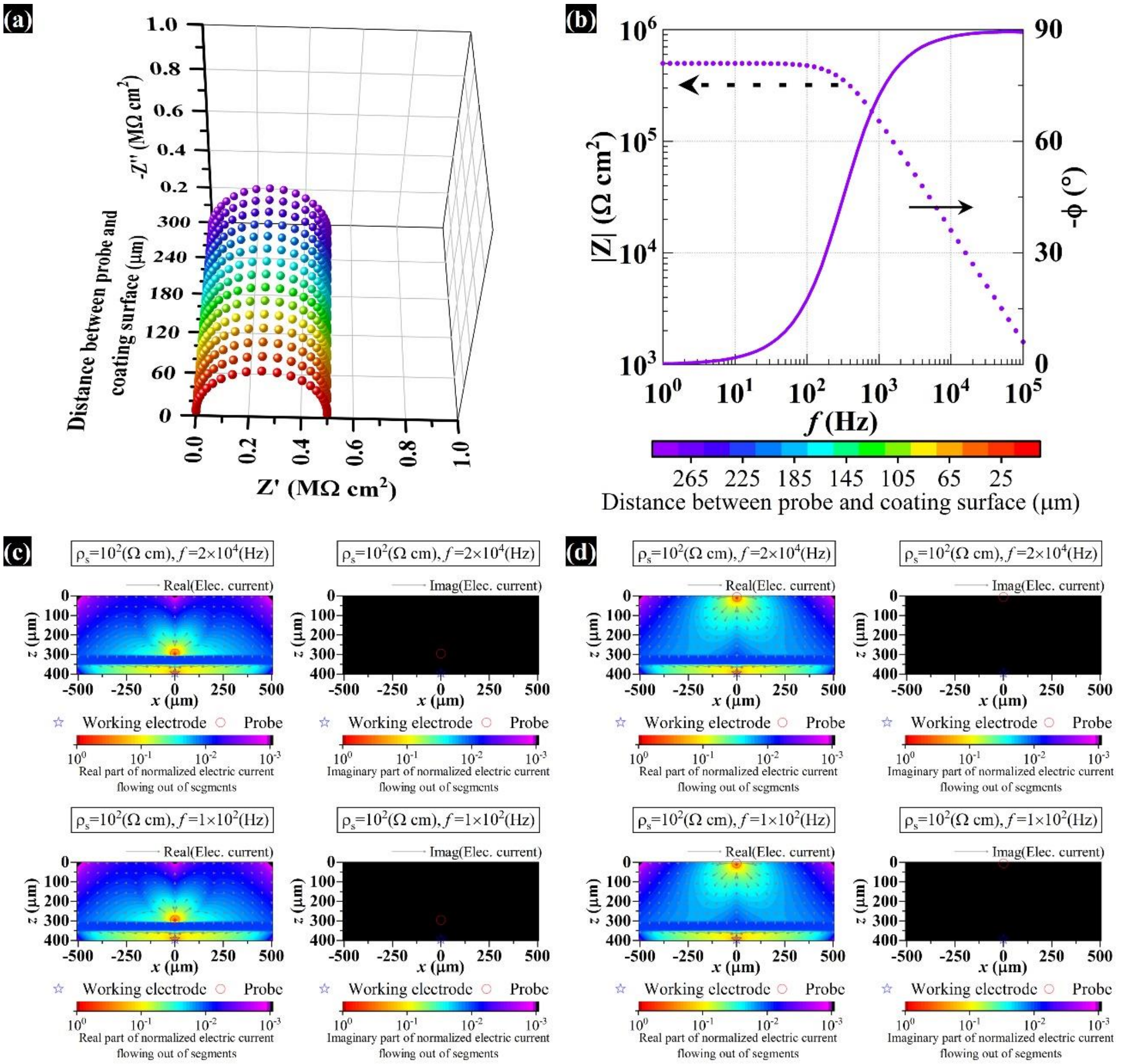

Figure 4.3 Localized response of homogenous coating without defect at 10^2 Ω cm electrical resistivity of electrolyte: (a) Nyquist plots with respect to the distance between electrode probe and coating surface. (b) Magnitude and phase angle of impedance spectra. (c) Real and imaginary part of normalized electric current flowing out of local segments at the 5 μm distance and 20000 Hz or 100 Hz. (d) Real and imaginary part of normalized electric current flowing out of local segments at the 295 μm distance and 20000 Hz or 100 Hz.

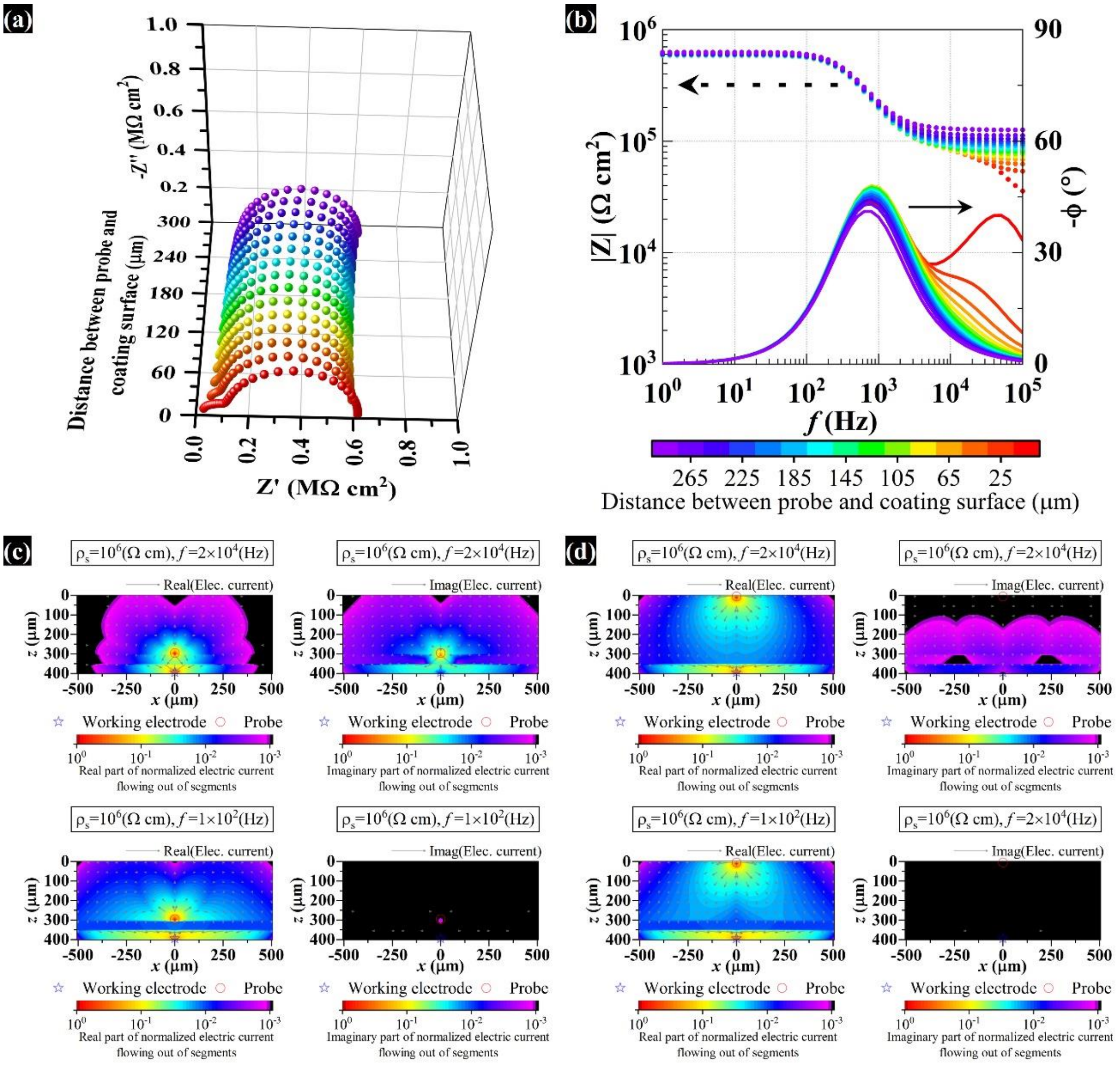

Figure 4.4 Localized response of homogenous coating without defect at 10^6 Ω cm electrical resistivity of electrolyte: (a) Nyquist plots with respect to the distance between electrode probe and coating surface. (b) Magnitude and phase angle of impedance spectra. (c) Real and imaginary part of normalized electric current flowing out of local segments at the 5 μm distance and 20000 Hz or 100 Hz. (d) Real and imaginary part of normalized electric current flowing out of local segments at the 295 μm distance and 20000 Hz or 100 Hz.

To know the local response of the impedance spectra depending on the location of the electrode probe in a *z*-direction, we considered a homogeneous coating without a defect, as illustrated in Figs. 4.3 and 4.4. The electrolyte resistivity to be conductive solution is considered as 100 Ω·cm. As shown in the Nyquist and Bode images of Fig. 4.3(a) and (b), there is little difference between each impedance signal resulted from the distance between electrode probe and coating surface in high electrical conductivity solution. This result can be seen in more detail through the local electrical current distribution that occurs during measurement. The electric current distribution flowing out of local segments is normalized based on input electrical current and then divided the current into real and imaginary parts as shown in Fig. 4.3(c) and (d). Since normalized, the input electrical current at electrode probe is always 1, the real value is 1, and the imaginary value is 0. The real part of normalized electric current distribution flowing out of each local segment could be considered as the relative amount of electric current flow through the each segment between the measurement electrodes, and the imaginary part of the current distribution could indirectly describe the influence of the phase shift induced by local dielectric properties. First, the electric current distribution inside the coating is shown evenly and similarly regardless of the applied frequency through the real part of electric current flow. As frequency increases, the electrolyte is sufficiently conductive regardless of the decrease in the impedance value of the dielectric coating, so that the electric currents are distributed evenly over the coating surface through the electrolyte first and are measured evenly within the designed coating domain. That is why the same homogeneous bulk coating system is measured even if frequency changes, and the impedance spectra show a perfect semi-circle as an ideal response. In addition, it appears that the impedance of the coating is not sensitive for the electrode probe location in high conductive solution. When the electrode probe is away from the coating surface in Fig. 4.3(d), the electrical current is distributed uniformly towards the coating surface to obtain more electrical passes. Even if the electrode probe is close to the coating surface as shown in Fig. 4.3(c), more electrical path can be obtained through the back flow of electrical current, which is the opposite flow from electrode probe to working electrode, within the high electrical conductive electrolyte and the current signal spreads evenly towards the coating surface. Therefore, almost the same impedance spectra can be observed in low electrical resistive solution.

However, under high electrical resistivity condition (10^6 Ω·cm), unusual phenomena are seen depending on the local position of the electrode probe and the measurement frequency as described in Fig. 4.4. First of all, the effect of the electrode probe position is clearly shown by the increase in the resistivity of electrolyte solution in the magnitude plot of Fig 4.4(b). The increase in solution resistance can be seen in high frequency region as the electrode probe moves away from the coating surface. In addition, as it can be seen in Nyquist (Fig. 4.4(a)) and phase angle (Fig. 4.4(b)) plots, it shows more time constants than one time constant in single-layered homogenous coating when the electrode probe is closer to the coating surface. If researchers are not aware of the system, the researchers will generally explain the system through equivalent values and most likely conclude as a complex system with more than two-time constants. This is the result of the homogeneous system that shows that non-homogeneous result dependent on the local measurement condition. For a more detailed understanding, it is considered through the distribution of normalized electric current flowing out of each segment as illustrated in Fig. 4.4(c) and (d). These calculation results explain how important the distribution of electric current for local measurement is within the electrolyte. When the position of electrode probe is far away from the coating surface, the current distribution appears to yield sufficient electrical paths for measuring the coating system in a similar area within the electrolyte, regardless of the applied frequency in Fig. 4.4 (d). However, as described in Fig. 4.4(c), when the probe electrode is moved close to the coating surface exposed to low electrical conductivity solution, real part of normalized electric current can confirm that the measured current is localized without much back flow in the electrolyte because of the relatively small impedance value of dielectric coating under high perturbation frequency. Because the relative conductivity between two mediums including electrolyte and coating, in which the electric current determines the pattern of flow, varies according to the applied frequency, it appears to measure the coating system in different areas from the bulk system perspective. Therefore, it shows non-homogeneous results in the impedance spectra as shown in the result of sweeping frequencies in red signal of Fig. 4.4(a) and (b). In other words, this means that local area characteristic can be measured in relatively high perturbation frequency and high electrical resistive solution.

Fig. 4.5 shows the effect of the electrical resistivity of the electrolyte solution and applied frequency on the impedance magnitude of the scratched coating sample designed in Fig. 4.1(b). First, it is confirmed that the magnitude of the impedance increases with an increase of the electrical resistivity of the electrolyte solution. This is because the higher the electrical resistivity of electrolyte solution under similar electrical path conditions, the higher the electrical resistance of the electrolyte solution becomes. In addition, as the measurement perturbation frequency decreases, the magnitude of the impedance tends to increase in Fig. 4.5. This is because as the frequency decreases, the impedance magnitude values of the dielectric coating material and the metal/electrolyte interface increase.

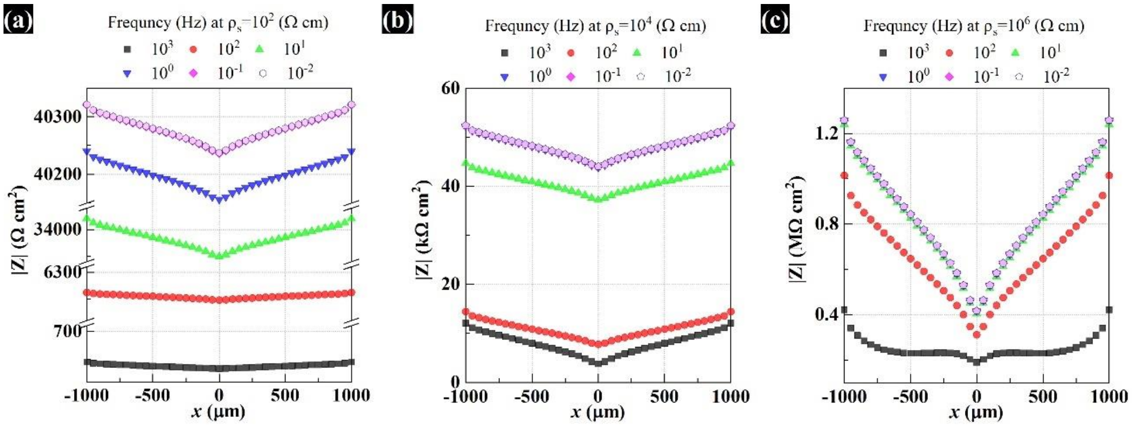

Figure 4.5 The effect of electrolyte electrical resistivity and applied frequency on the impedance magnitude of scratched coating sample: (a) $\rho_s=10^2$ Ω cm. (b) $\rho_s=10^4$ Ω cm. (c) $\rho_s=10^6$ Ω cm.

When the scratched coating system is immersed in low electrical resistivity electrolyte solution, it is evident that the impedance magnitude increases linearly as the electrode probe moves away from the scratch area in Fig. 4.5(a) and (b). Even if the system is exposed to the high electrical resistivity electrolyte of 10^6 Ω cm, the measuring at the perturbation frequency lower than 10 Hz still gives a similar response to changes in the impedance magnitude depending on electrode probe position in the low electrical resistivity electrolyte. However, as described in black squares of Fig. 4.5(c), the measurement conditions of 10^3 Hz high frequency and 10^6 Ω cm high electrical resistivity electrolyte yield the impedance response that differs from the linear changes. The impedance magnitude increases linearly as the electrode probe moves away from the zero position on the x-axis, the center of the scratch part, and then shows constant values from when the electrode probe reaches on the unscratched coating area. Then, as the electrode probe reaches the 2D domain's boundary, it shows an increasing signal again.

The physical meaning of the impedance spectra according to the electrode probe location under the various measurement conditions, including perturbation frequency and electrical electrolyte resistivity, could be understood in detail through the distribution of flowing electric current between measurement electrodes. Figs. 4.6-4.14 display normalized electric current distribution according to the electrode probe position, applied frequency, the electrical resistivity of electrolyte solution. It can be confirmed from this calculation that LEIS in the low resistivity electrolyte solution does not measure the local part of the coating except the scratch from Figs. 4.6-4.8. Since the electrical current flows easily into the scratched coating part through the highly conductive electrolyte solution, the linear change of LEIS can be seen as it moves away from the center of the probe position. The imaginary part of normalized electric current distribution also shows that LEIS at low electrical resistivity solution measures the scratch area regardless of the location in the x-direction of the electrode probe as described in Figs. 4.6(b)-4.8(b). The imaginary electric current distribution indirectly expresses the phase shift that is induced by the influence of the dielectric properties in local segments. The results indicate the imaginary electric current distribution in a similar area without being influenced by the position of the x-direction of the electrode probe, which explains that the dielectric effects of measuring under low electrical resistivity electrolyte condition is mostly due to double layer capacitors at the metal/electrolyte interface.

Similarly, the phenomenon, which measures the scratch part, not the local area of the electrode probe location, can be observed in the high resistivity electrolyte solution when the perturbation frequency is low (10 Hz), as shown in Fig. 4.14. This is because at low perturbation frequency, the relative impedance value of the dielectric coating material is higher than the electrical resistance of the electrolyte, so that the electric current moves to scratch part via the electrolyte. Thus, even in this case, electrode probe tends to increase linearly as it moves away from the scratch position in Fig. 4.5(c).

Therefore, in order to observe local changes in all measurement areas in the case of scratched coatings, it is necessary to use high electrolyte resistivity as described in Figs. 4.12 and Fig. 4.5(c). Real and imaginary parts of normalized electric current enable us to observe large amounts of electric current flow through the local coating area near the electrode probe due to the impedance value of the dielectric coating which is relatively small at high frequency (10^3 Hz). This allows the electrode probe to measure the electrical properties of local coating area and obtains a nearly constant impedance magnitude value on homogeneous properties of coating in Fig. 4.5(c). In addition, the phenomenon of an increase in impedance magnitude as the electrode probe approaches the boundary of 2D domain indicates limitations in calculating the local phenomenon of the proposed 2D impedance model because the area of the electric current that can flow through coating decreases due to the insulating boundary condition. Despite the limitation, however, this study is expected to be able to propose the suitable guidelines of the electrical electrolyte conductivity and AC perturbation frequency according to the designed coating to observe and understand local characteristics of the coating.

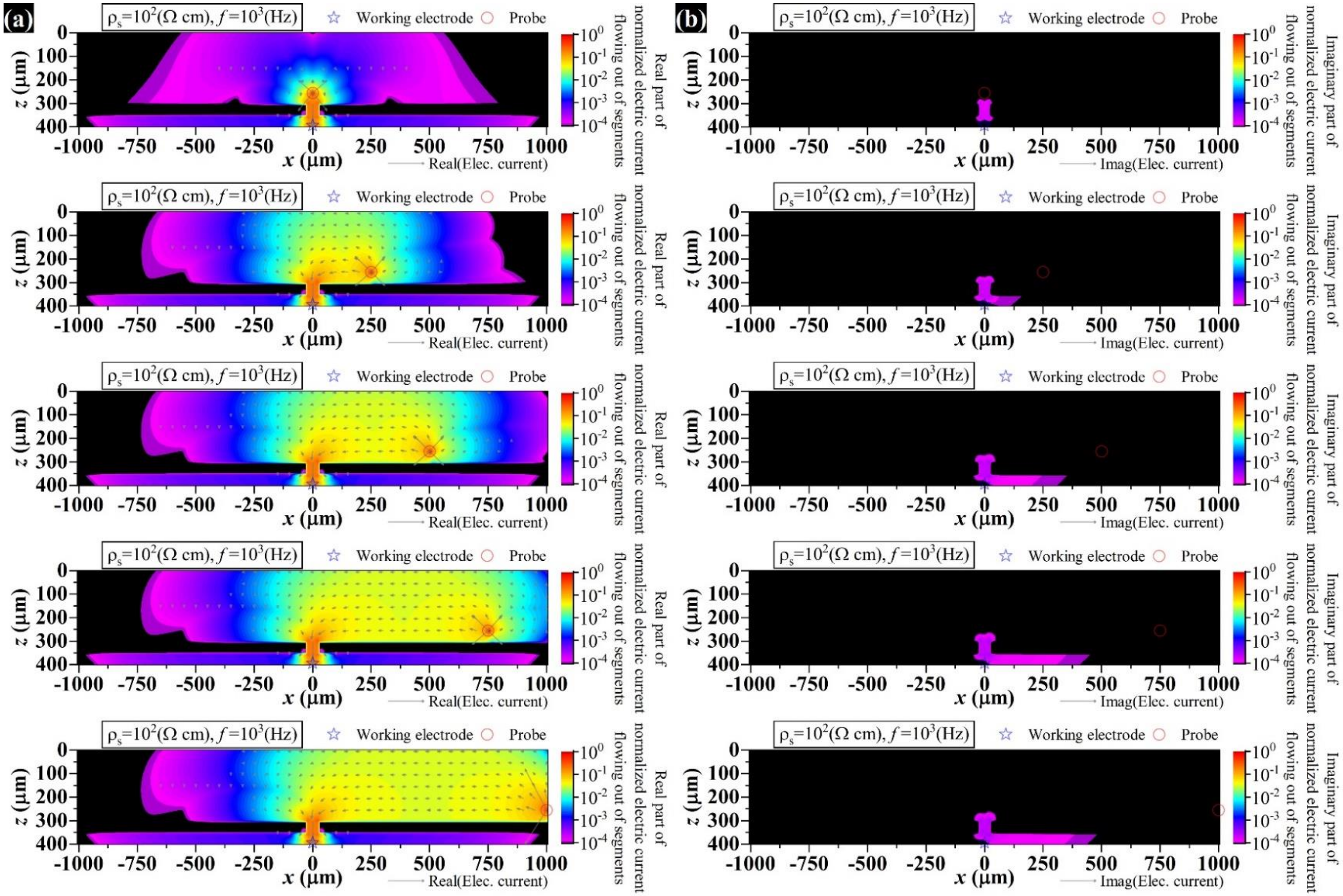

Figure 4.6 Normalized electric current distribution according to electrode probe positions at ρ_s=10^2 Ω cm and *f*=10^3 Hz: (a) Real part of normalized electric current. (b) Imaginary part of normalized electric current.

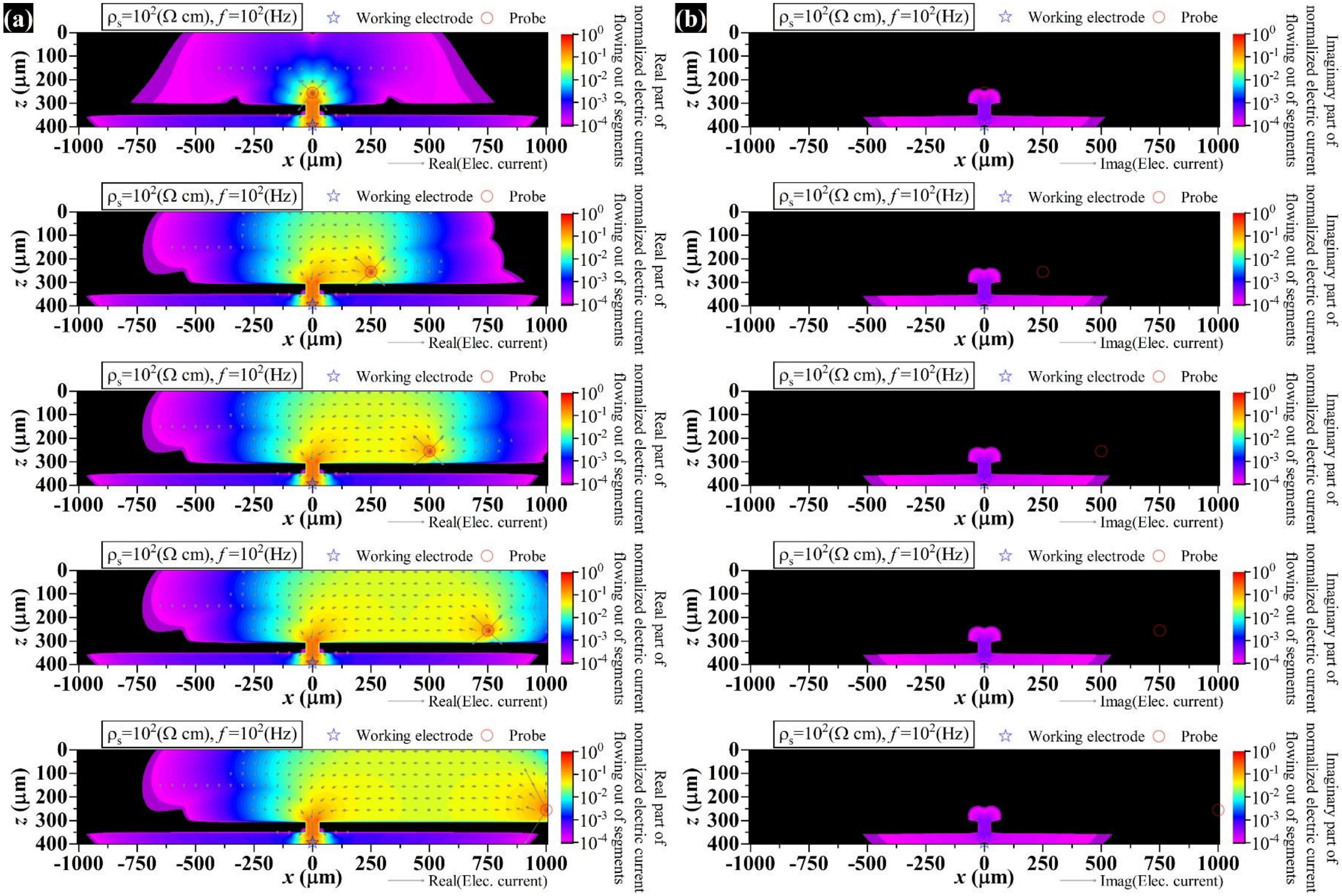

Figure 4.7 Normalized electric current distribution according to electrode probe positions at ρ_s=10^2 Ω cm and f=10^2 Hz: (a) Real part of normalized electric current. (b) Imaginary part of normalized electric current.

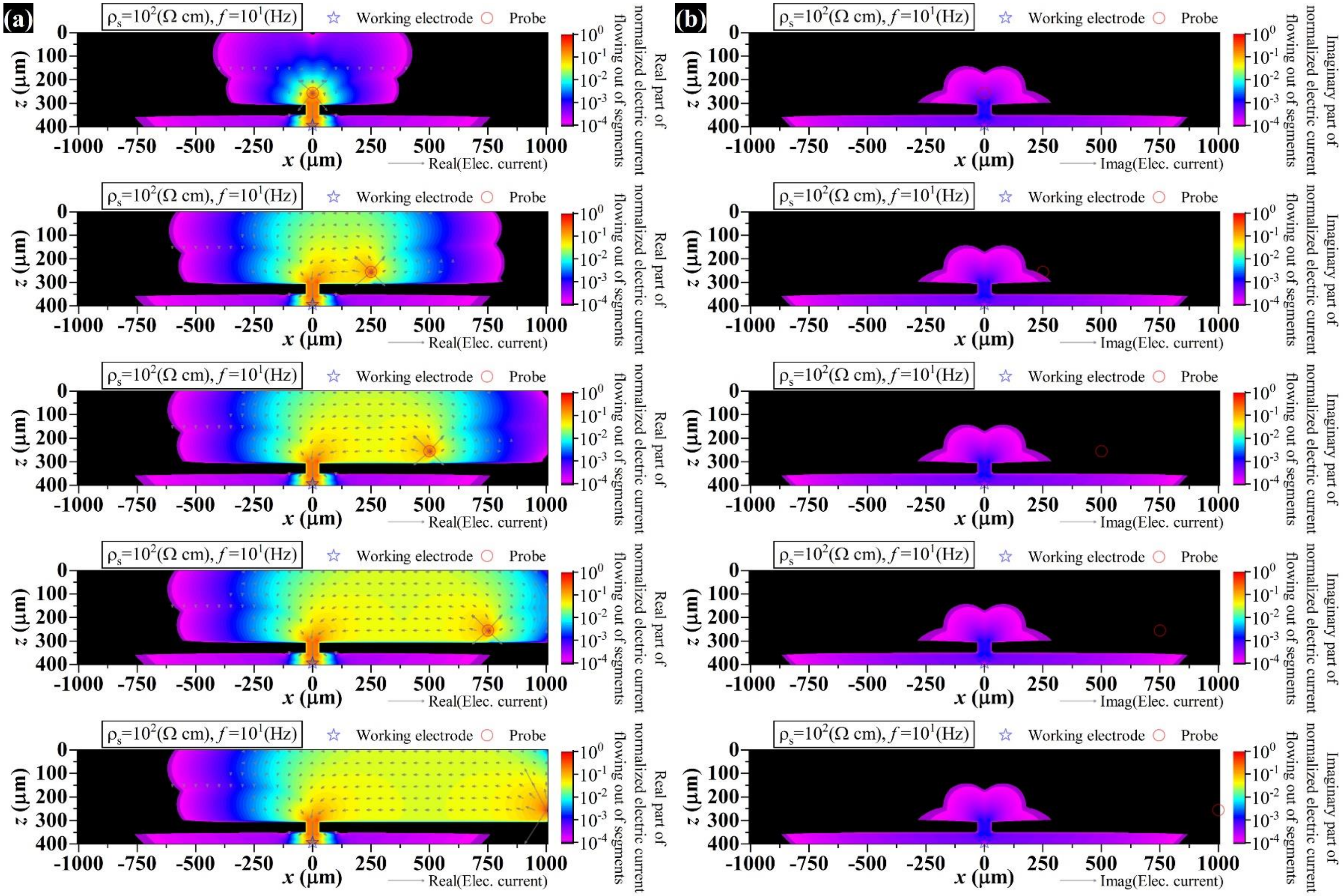

Figure 4.8 Normalized electric current distribution according to electrode probe positions at $\rho_s=10^2$ Ω cm and $f=10^1$ Hz: (a) Real part of normalized electric current. (b) Imaginary part of normalized electric current.

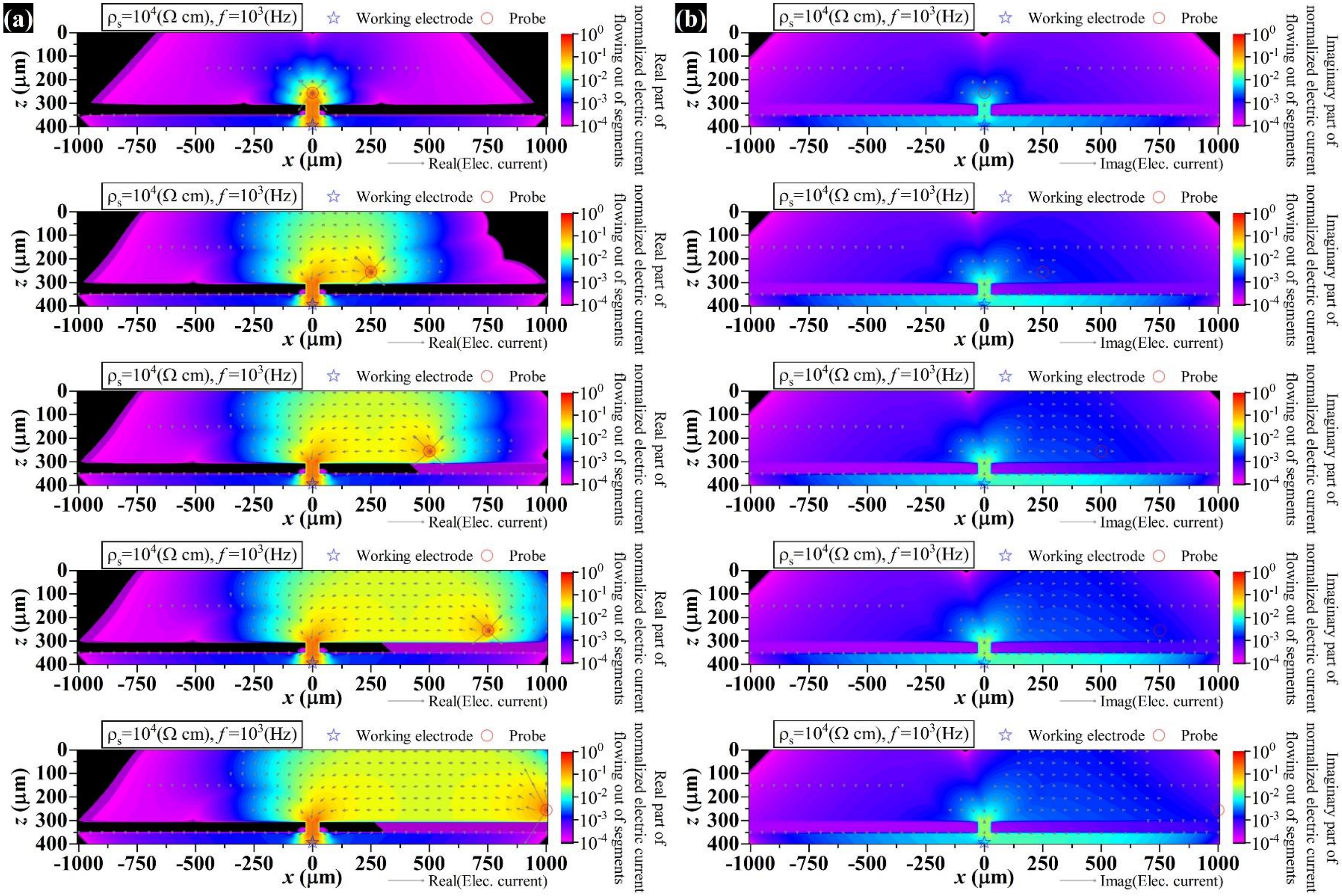

Figure 4.9 Normalized electric current distribution according to electrode probe positions at $\rho_s=10^4$ Ω cm and $f=10^3$ Hz: (a) Real part of normalized electric current. (b) Imaginary part of normalized electric current.

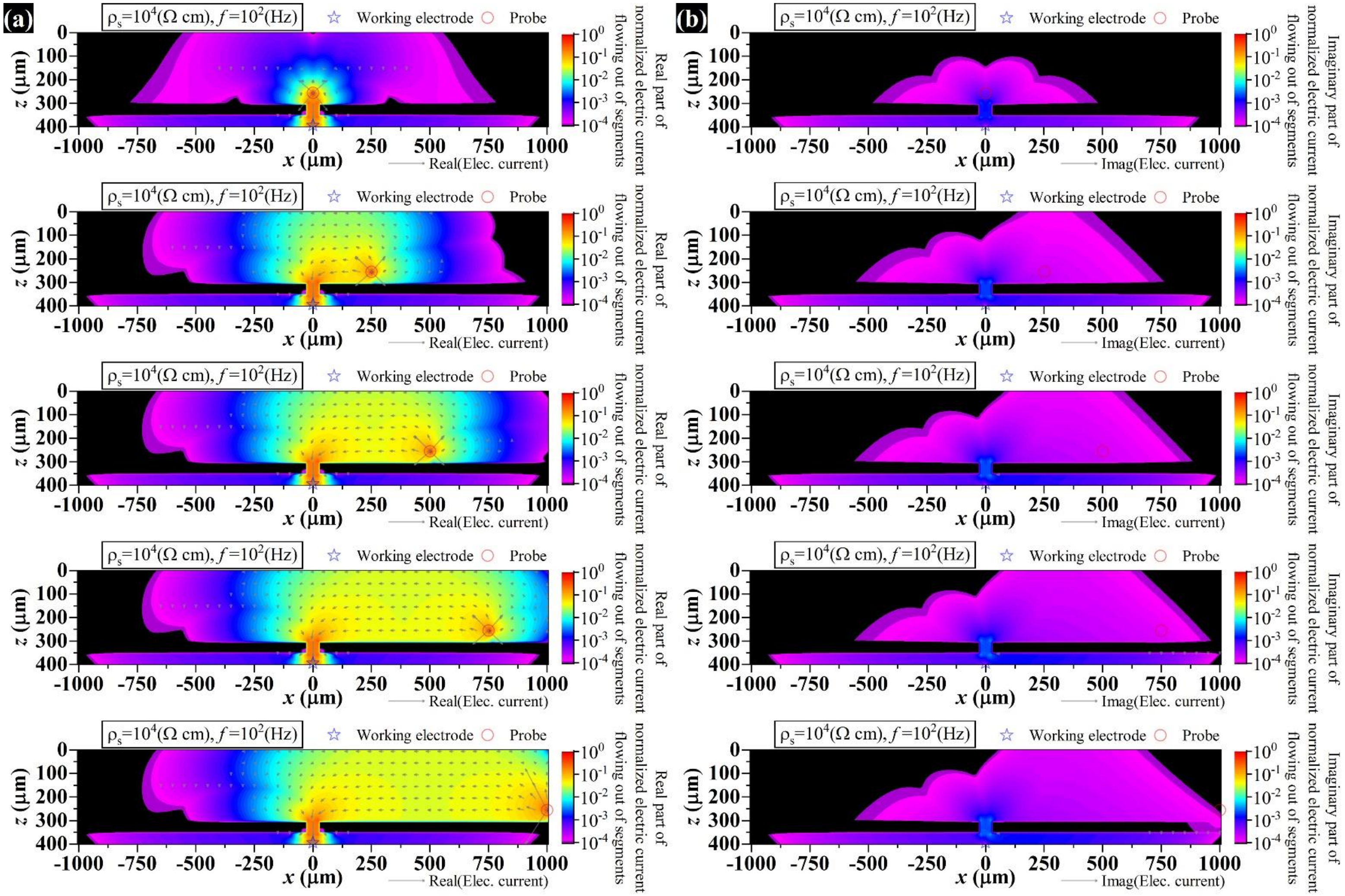

Figure 4.10 Normalized electric current distribution according to electrode probe positions at ρ_s=10^4 Ω cm and *f*=10^2 Hz: (a) Real part of normalized electric current. (b) Imaginary part of normalized electric current.

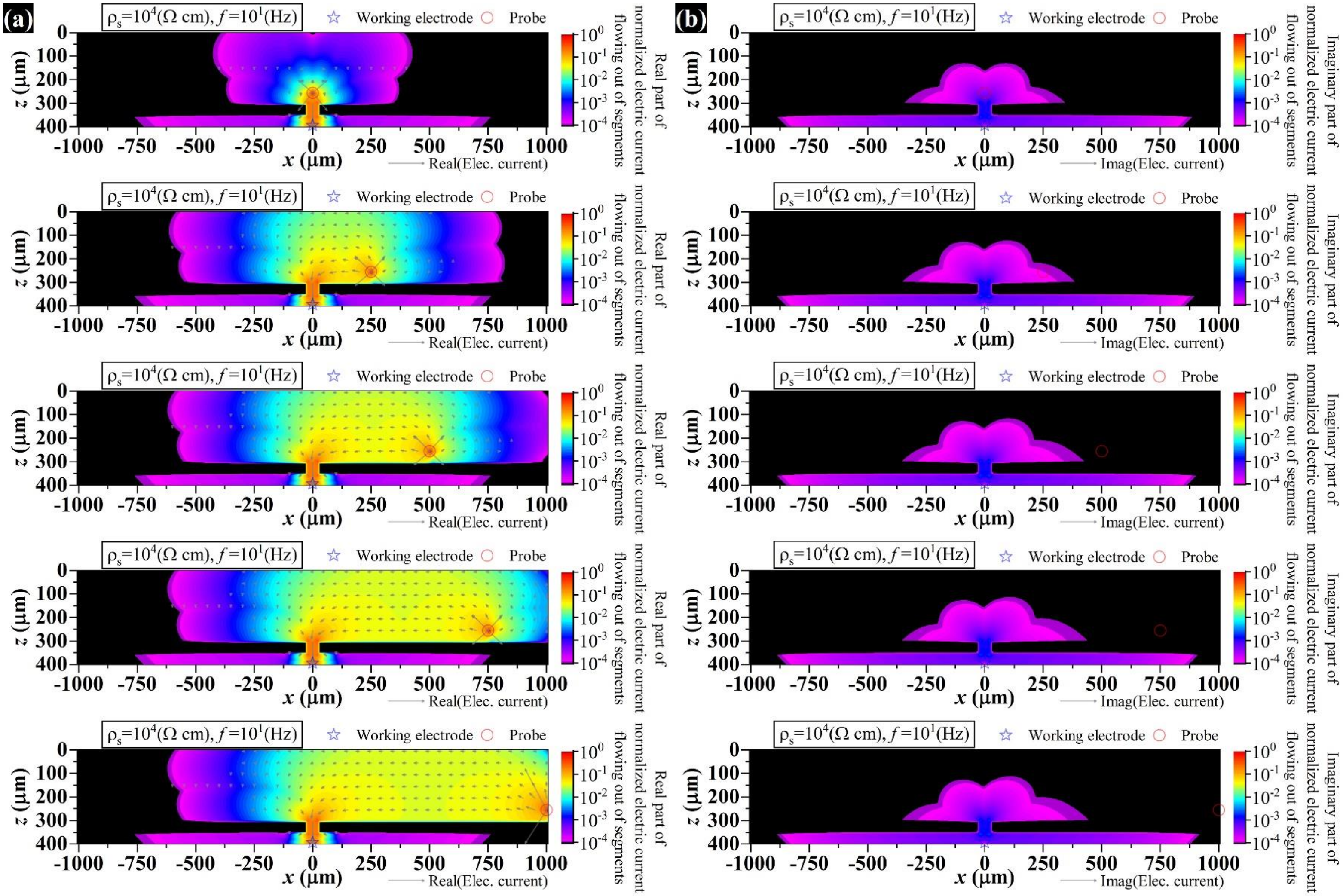

Figure 4.11 Normalized electric current distribution according to electrode probe positions at ρ_s=10^4 Ω cm and f=10^1 Hz: (a) Real part of normalized electric current. (b) Imaginary part of normalized electric current.

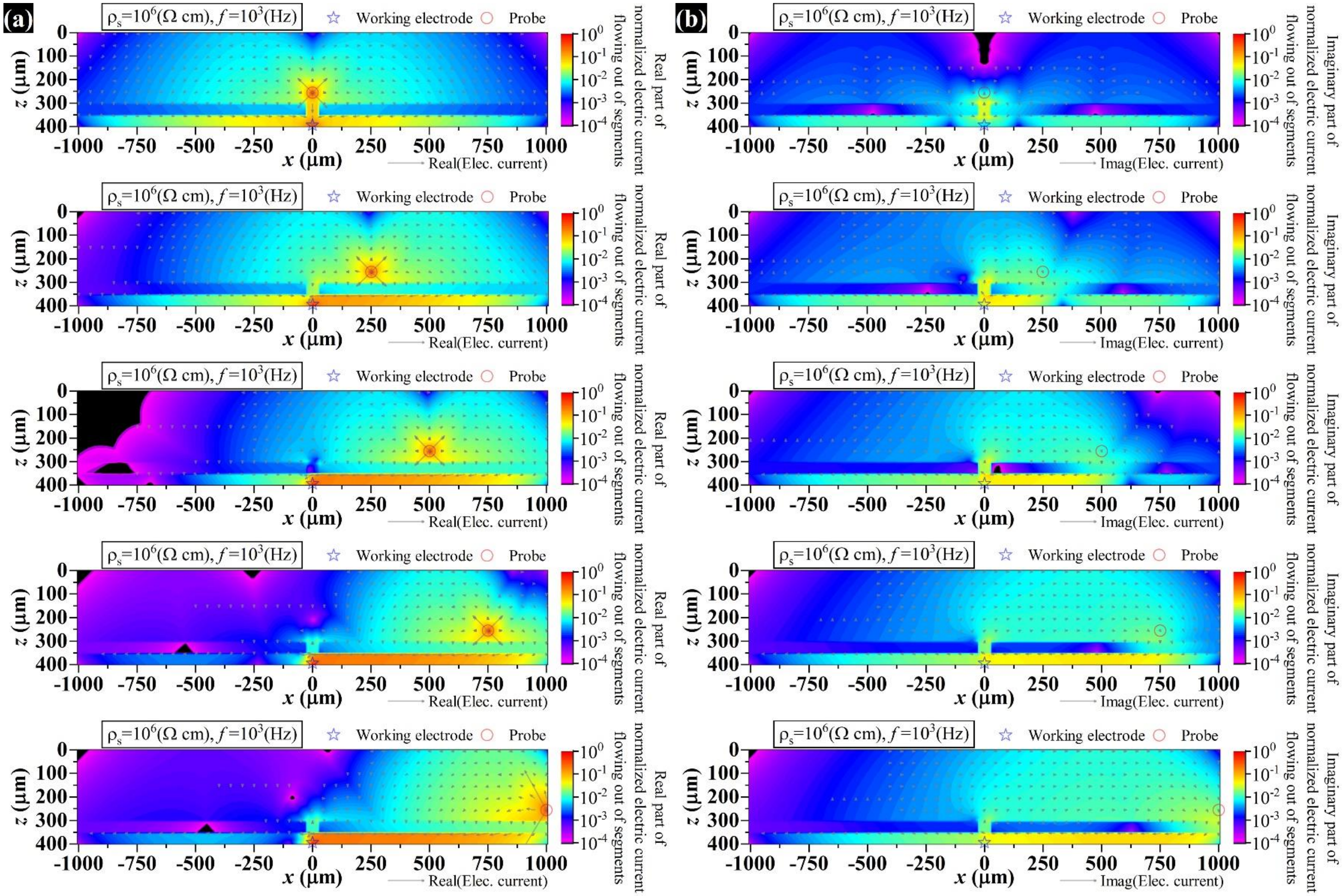

Figure 4.12 Normalized electric current distribution according to electrode probe positions at $\rho_s=10^6$ Ω cm and $f=10^3$ Hz: (a) Real part of normalized electric current. (b) Imaginary part of normalized electric current.

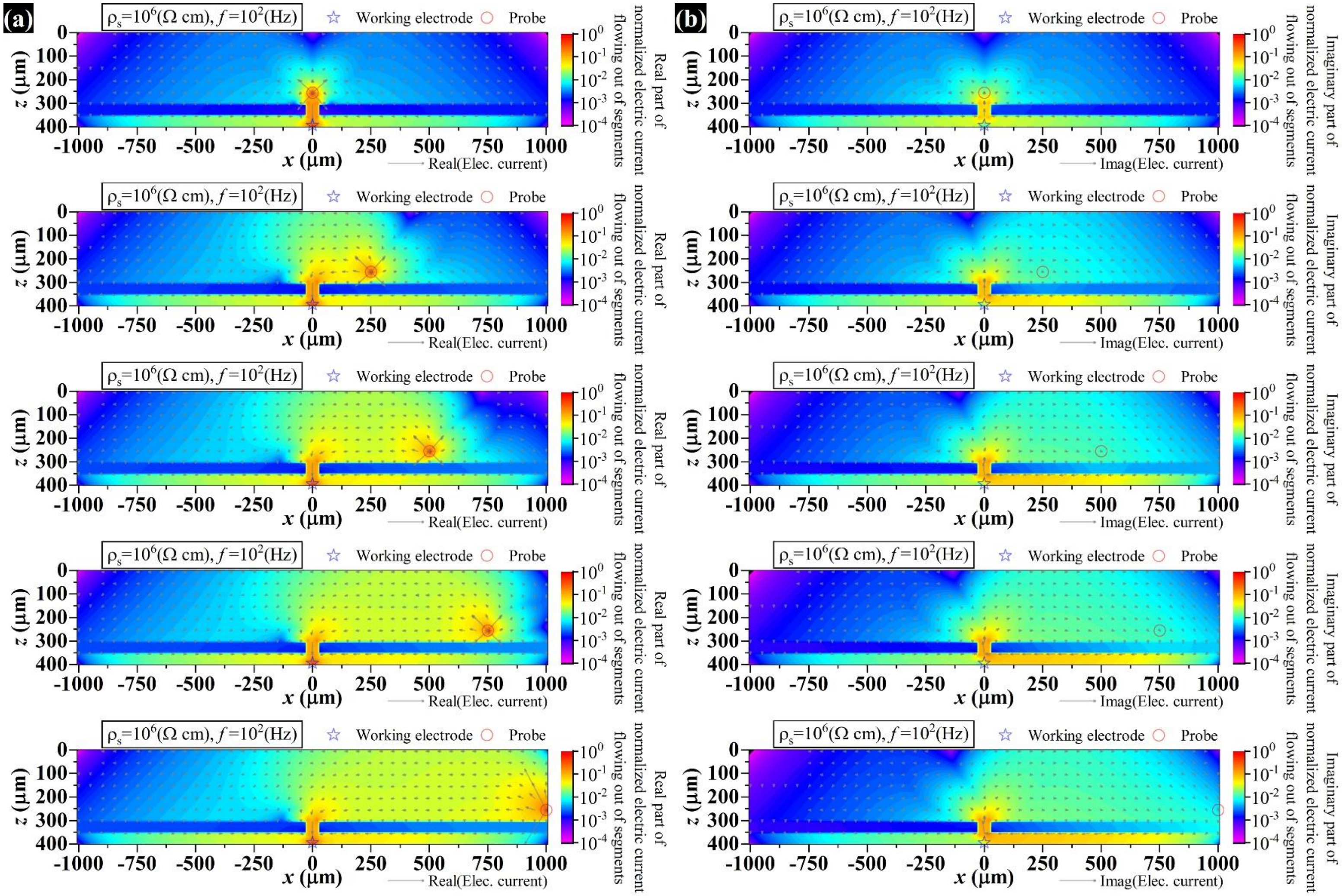

Figure 4.13 Normalized electric current distribution according to electrode probe positions at ρ_s=10^6 Ω cm and *f*=10^2 Hz: (a) Real part of normalized electric current. (b) Imaginary part of normalized electric current.

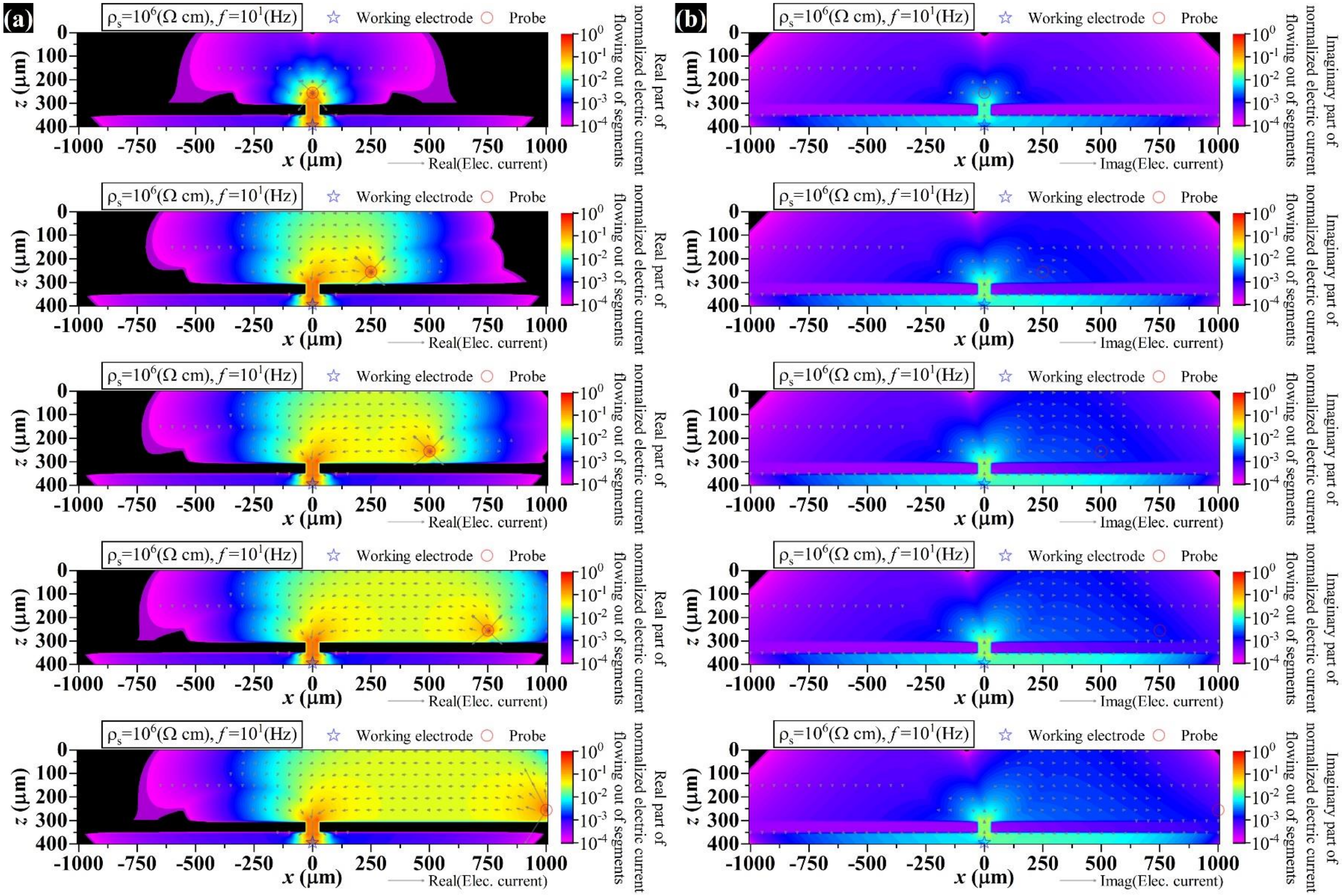

Figure 4.14 Normalized electric current distribution according to electrode probe positions at ρ_s=10^6 Ω cm and *f*=10^1 Hz: (a) Real part of normalized electric current. (b) Imaginary part of normalized electric current.

4.4. Summary

The localized 2D impedance model was proposed to understand the response of the localized impedance spectra. The various environmental conditions, including the electrode probe location used in local measurements, examined the physical meaning represented by the impedance signal from the perspective of the perturbation frequency and the electrical/electrochemical properties of the systems. Normalized electric current distribution induced by local measurement was presented to understand the meaning of the impedance value. The electric current distribution overcomes the limits of the fact that the position of the electrode probe is assumed to be a locally measured position and allows the actual area of local measurement to be identified under real test conditions.

In this study, two single-layered systems with and without defect were considered. For the homogeneous single-layer coating without defect, the closer the electrode probe is to the coating surface, it was confirmed that the area measured according to perturbation frequency is different at low electrical conductivity of electrolyte. Then, non-homogenous impedance spectra were obtained from the homogenous system. When the coating system with defect is considered in the high electrical conductivity of electrolyte, the electric current distribution and impedance spectra results showed that the local technique measured the defect rather than the local area near the location of probe at most perturbation frequencies, so the local impedance and the distance between the electrode probe and the defect area was described a linear relationship. If the scratched coating system is immersed in low electrical conductivity solution, the impedance of the dielectric coating material is relatively small in the high frequency, thus it was confirmed that local characteristics can be displayed by ensuring that normalized the electric current is propagated into the coating rather than spreading through electrolyte.

4.5. References

[1] J.-B. Jorcin, M.E. Orazem, N. Pébère, B. Tribollet, CPE analysis by local electrochemical impedance spectroscopy, Electrochimica Acta, 51 (2006) 1473-1479.

[2] S. Taylor, Incentives for using local electrochemical impedance methods in the investigation of organic coatings, Progress in Organic Coatings, 43 (2001) 141-148.

[3] V.M. Huang, S.-L. Wu, M.E. Orazem, N. Pébère, B. Tribollet, V. Vivier, Local electrochemical impedance spectroscopy: A review and some recent developments, Electrochimica Acta, 56 (2011) 8048-8057.

[4] R. Lillard, P. Moran, H. Isaacs, A novel method for generating quantitative local electrochemical impedance spectroscopy, Journal of the Electrochemical Society, 139 (1992) 1007.

[5] I. Frateur, V.M. Huang, M.E. Orazem, B. Tribollet, V. Vivier, Experimental issues associated with measurement of local electrochemical impedance, Journal of the Electrochemical Society, 154 (2007) C719-C727.

[6] E. Bayet, F. Huet, M. Keddam, K. Ogle, H. Takenouti, Local electrochemical impedance measurement: scanning vibrating electrode technique in ac mode, Electrochimica Acta, 44 (1999) 4117-4127.

[7] M. Pilaski, T. Hamelmann, A. Moehring, M. Lohrengel, Impedance spectroscopy in micro systems, Electrochimica Acta, 47 (2002) 2127-2134.

[8] T. Balusamy, T. Nishimura, In-situ monitoring of local corrosion process of scratched epoxy coated carbon steel in simulated pore solution containing varying percentage of chloride ions by localized electrochemical impedance spectroscopy, Electrochimica Acta, 199 (2016) 305-313.

[9] A.S. Bandarenka, K. Eckhard, A. Maljusch, W. Schuhmann, Localized electrochemical impedance spectroscopy: Visualization of spatial distributions of the key parameters describing solid/liquid interfaces, Analytical Chemistry, 85 (2013) 2443-2448.

[10] C. Zhong, X. Tang, Y. Cheng, Corrosion of steel under the defected coating studied by localized electrochemical impedance spectroscopy, Electrochimica Acta, 53 (2008) 4740-4747.

[11] F. Zou, D. Thierry, Localized electrochemical impedance spectroscopy for studying the degradation of organic coatings, Electrochimica Acta, 42 (1997) 3293-3301.

[12] J.-B. Jorcin, E. Aragon, C. Merlatti, N. Pébère, Delaminated areas beneath organic coating: A local electrochemical impedance approach, Corrosion Science, 48 (2006) 1779-1790.

[13] M. Szocinski, K. Darowicki, Local impedance spectra of organic coatings, Polymer Degradation and Stability, 98 (2013) 261-265.

[14] A.S. Bandarenka, Exploring the interfaces between metal electrodes and aqueous electrolytes with electrochemical impedance spectroscopy, Analyst, 138 (2013) 5540-5554.

[15] M. Mouanga, M. Puiggali, O. Devos, EIS and LEIS investigation of aging low carbon steel with Zn–Ni coating, Electrochimica Acta, 106 (2013) 82-90.

[16] T. Balusamy, T. Nishimura, Localized electrochemical impedance spectroscopy observation on scratched epoxy coated carbon steel in saturated Ca (OH) 2 with various chloride concentration, Journal of Analytical & Bioanalytical Techniques, 7 (2016) 2.

[17] K. Eckhard, T. Erichsen, M. Stratmann, W. Schuhmann, Frequency-dependent alternating-current scanning electrochemical microscopy (4D AC-SECM) for local visualisation of corrosion sites, Chemistry–A European Journal, 14 (2008) 3968-3976.

[18] S. Cho, Y. Cubides, H. Castaneda, Probing the degradation mechanism of a Cr (VI) coating/aluminum alloy 2024-T3 system based on dynamic mechanisms and a 2D deterministic-probabilistic approach, Electrochimica Acta, 236 (2017) 82-96.

5. NON-CONVENTIONAL ELECTRICAL IMPEDANCE BEHAVIOR[*]

Non-conventional responses in the impedance spectra of a zinc-rich coating system were observed in electrical impedance measurements that have previously been considered to have no effect on the system. Non-electrolytic cells on zinc-rich (55 vol%) coatings with multi-wall carbon nanotube systems were analyzed to determine the intrinsic response of the coating with electrical passive and active analogs under electrical conditioning cycles. In the dry condition, the impedance spectra of the carbon nanotube-added zinc-rich coating showed increased electrical resistance of the film under consecutive cyclic testing. The non-conventional response of the increase in impedance was studied by determining the impedance responses under various temperatures and bias potentials and performing a current-voltage method. The non-conventional phenomenon was found to be caused by an increased barrier height between the semiconducting zinc oxide material and metal, which is susceptible to an external electrical field.

5.1. Introduction

Zinc has been widely used in organic or inorganic coatings to protect steel substrates against corrosion [1-4]. The protective mechanism is based on zinc, which is

---

[*] Part of this section is reprinted with permission from “Electrical and electrochemical behavior of a zinc-rich epoxy coating system with carbon nanotubes as a diode-like material” by Seongkoo Cho, Tse-Ming Chiu, Homero Castaneda, 2019. *Electrochimica Acta*, 316, 189-201, Copyright © 2019 by Elsevier Ltd.

in electrical contact with the underlying steel surface and provides cathodic protection: the anodic dissolution of the zinc occurs before the steel corrodes, and the zinc thus acts as a sacrificial material that slows the degradation of steel substrate [5]. The anodic reaction corresponding to zinc dissolution (1) and an oxygen reduction reaction (2) at the surface of the metal substrate in near neutral electrolyte solution occur as follows:

$$Zn \rightarrow Zn^{2+} + 2e^{-} \tag{5.1}$$

$$\mathrm{O}_2 + 2H_2O + 4e^{-} \rightarrow 4OH^{-} \tag{5.2}$$

The second protective mechanism is the barrier protection provided by the solid matrix of the zinc-rich primer (ZRP), which results from delaying water uptake and mass transport [6] or alternatively from the zinc corrosion product's filling the pore spaces in the ZRP coating [7, 8]. To prolong the cathodic protection period and promote the barrier performance of ZRP films, additional electrical paths for galvanic action have been built by including conductive additives such as polyaniline nanofibers [9, 10], graphene [11, 12], and carbon nanotubes(CNTs) [13, 14], as well as controlling the sizes of the zinc particles[15].

These protective mechanisms have been characterized and studied with time and frequency domain electrochemical methods; the former includes open circuit potential (OCP), linear polarization, and cyclic potentiodynamic polarization [3], and the latter includes electrochemical impedance spectroscopy (EIS) [16, 17]. In OCP measurements, no external electrical potential or current is introduced into the electrochemical system by design. The frequency domain technique EIS reveals the dielectric characteristics of the formed interfaces. Both methods are generally considered non-destructive techniques that provide mechanistic and qualitative interfacial information on the system over time [18, 19], and they have been used to assess the performance of the ZRP system [20, 21]. For example, the physical characteristics of ZRP film, including the electrical resistance of the coating containing zinc particles, corrosion products, and epoxy matrix with electrolyte penetration, as well as the impedance characteristics due to charge-transfer or mass-transfer-controlled processes have been evaluated with EIS [21-23]. The non-destructive conditions rely on a lack of influence on material characteristics when the assessment is performed. This assumption has been accepted, and thus further studies are lacking regarding the potential effects of these presumably non-destructive conditions on ZRP systems.

Many metal oxides controlling the corrosion process are either monolithic semiconductors or diodes [24]. In a ZRP coating system, the stochastic distribution of the corrosion products might potentially lead to the formation of diode junctions through the construction of semiconductor-metal or semiconductor- semiconductor interfaces. Zinc oxide, a semiconductive material with an inherent n-type doped tendency, is widely used in electronic devices because of its high electron mobility and wide direct band gap [25, 26]. The oxygen vacancies are responsible for most of the imperfections in the crystal lattice of the oxides and confer the semiconducting property [26]. In recent years, CNTs have been extensively studied and are considered to form Schottky contacts [27] or heterojunctions (as ambipolar materials) with metal [28]; some findings, including Schottky diode characteristics at the interface between multi-wall CNTs and zinc oxide, have been reported through measuring the current-voltage characteristics [29]. The ZRP film might also play a role as a diode in materials, owing to the existence of the corrosion product zinc oxide and the CNTs as conductive additives.

In this work, the effects of EIS measurement on CNT-added ZRP film were studied under dry condition through electrical cyclic sequences. We observed non-conventional electrical film responses and characterized two critical points: (i) the effects of the electroanalytical technique on the ZRP impedance response; (ii) the electrical interpretation of the dry coating.

5.2. Experimental Methods

5.2.1. Materials and Sample Preparation

ZRPs with multi-wall CNTs obtained from Tesla NanoCoatings were produced by mixing a solvent-based epoxy-polyamide primer with spherical fine zinc particles. Epoxy resin (6.7 wt%, Tesla® P1150ASAS) was mechanically blended with CNTs (<1 wt%) and tert-butyl acetate solvent. After mixing the CNTs and resin, 90 wt% zinc particles (55 vol%) were added under agitation at room temperature. Finally, 3.3 wt% Tesla ® P1150BSAS hardener was added to the agitated mixture with a 1:2 weight ratio of hardener to epoxy resin, and sonicated for 5 min. The final mixture was air-sprayed onto AISI 1008 carbon steel (UNS G10080, 0.035 wt% S, 0.030 wt% P, 0.15 wt% C, 0.60 wt% Mn, and balanced Fe). The coating was cured for 6 hours at 60 °C. The dry film coating thickness was measured as 418.10 ± 31.43 μm with a coating thickness gauge, and the cross-section SEM image of the designed coating is shown in Fig. 5.1(a).

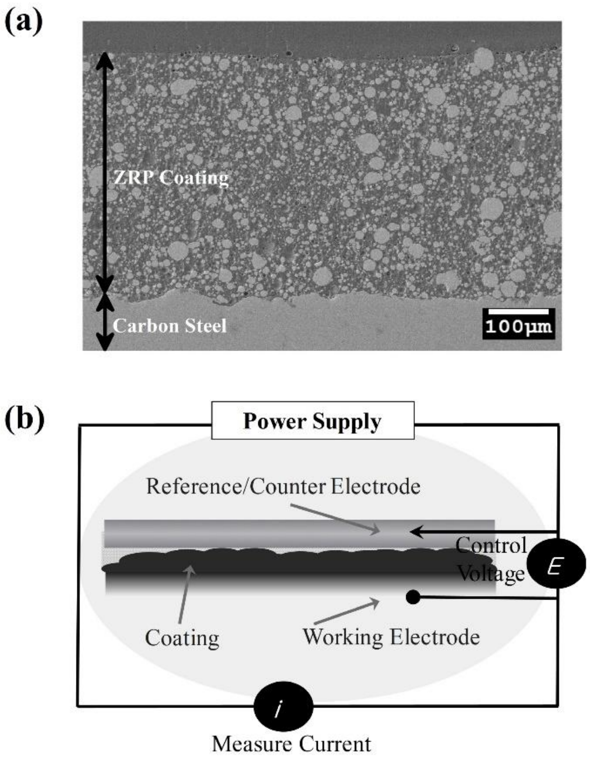

Figure 5.1 The images of a test sample and experimental setup: (a) Cross-section SEM image of intact ZRP/CNT coating. (b) A two-electrode sandwich-like cell at the dry condition.

5.2.2. Electrochemical Measurements in the Dry Condition

A two-electrode sandwich-like cell with an area of 3.19 cm^2 was used for the dry test presented in Fig. 5.1(b). ZRP-coated carbon steel was used as a working electrode, and a stainless-steel panel was used as a counter/reference electrode (CE/RE) at room temperature, 30 °C, 40 °C, and 50 °C. To control and set the dry coating temperature, we used a Faraday cage with a temperature controller. The surface temperature was measured with an infrared thermometer and controlled by the volumetric air flow rate at the required temperature. An air heater was used to control the conditions of the inlet air by applying a voltage to a resistive coil and transferring the heat generated from the coil into the cage. The electrical tests were conducted while the temperature of the coating surface was under steady state conditions. The electrical test sequence procedure was based on five loops, including a potential difference measurement between two electrodes, indicated as OCP, and EIS as a second technique. EIS was conducted by following the potential difference for 5 min (OCP), at frequencies between 100 kHz and 1 Hz at 10 points per decade interval and an amplitude of 10 mV (rms) around the OCP.

To understand the non-ohmic current-voltage relationship of the ZRP film, we used large polarization techniques of AC and DC at room temperature in the dry condition. Bias voltages (+1V to -1V) for EIS were applied on the ZRP at frequencies between 100 kHz and 1 Hz at 10 points per decade interval and an amplitude of 10 mV (rms). The DC current-voltage characteristics of the ZRP film were assessed by potentiodynamic testing by applying a wide voltage window between +1.5V to -1.5Vat a 10 mV/s scan rate. The applied voltage was set between the carbon steel substrate and CE/RE on the coating.

5.3. Results and Discussion

5.3.1. Non-conventional and Conventional Impedance Response in the Dry Condition

The basic electrical characteristics that occurred in the ZRP film were studied by conducting five continuous EIS cycles in a dry-film condition, as presented in Fig. 5.2. The electrochemical reaction can be eliminated in a dry test, because no electrolytes are added, and the dry test reveals the equivalent electrical properties of ZRP coatings, such as the dielectric constant and electrical resistivity, with no corrosion/degradation. Therefore, the system in the dry condition is analogous to an electrical circuit composed of a resistor (R_f) and constant phase element (CPE, Q_f) of the ZRP film and ohmic resistance (R_Ω) of cables, which corresponds to the electrically conductive pathways and dielectric properties. The CPE attributed to non-ideal capacitive behavior is used for an equivalent description of a porous coated system, electric double layers, or heterogeneous coating materials [21, 30, 31]. Fig. 5.1(a) shows the heterogeneous distribution of zinc particles in the ZRP film. Various ‘depressed’ semicircles in Nyquist format were expected to be produced after EIS testing. Fig. 5.2(a) shows the accuracy of the fitting process according to the EIS tests, with fitting errors of less than 0.03. This result demonstrates the good agreement between the experimental and theoretical fitting process for the film in the dry condition. During continuous EIS testing, an increase in ohmic resistance was observed over the testing cycles (from 3 to 6 $M\Omega\ cm^2$), as represented by the diameter of the semicircle in Fig. 5.2(a). In the case of OCP, there was a slight change (10 µV - 50 µV) in the cyclic test conditions, but there was no particular trend and no relation to the tendency of the increase in impedance magnitude. Fig. 5.2(b) illustrates that the ohmic resistance of all ZRP coating samples increased by approximately 60% over the initial resistance after five cyclic tests. This result demonstrates how the EIS test influences the electrical response of the ZRP coating system.

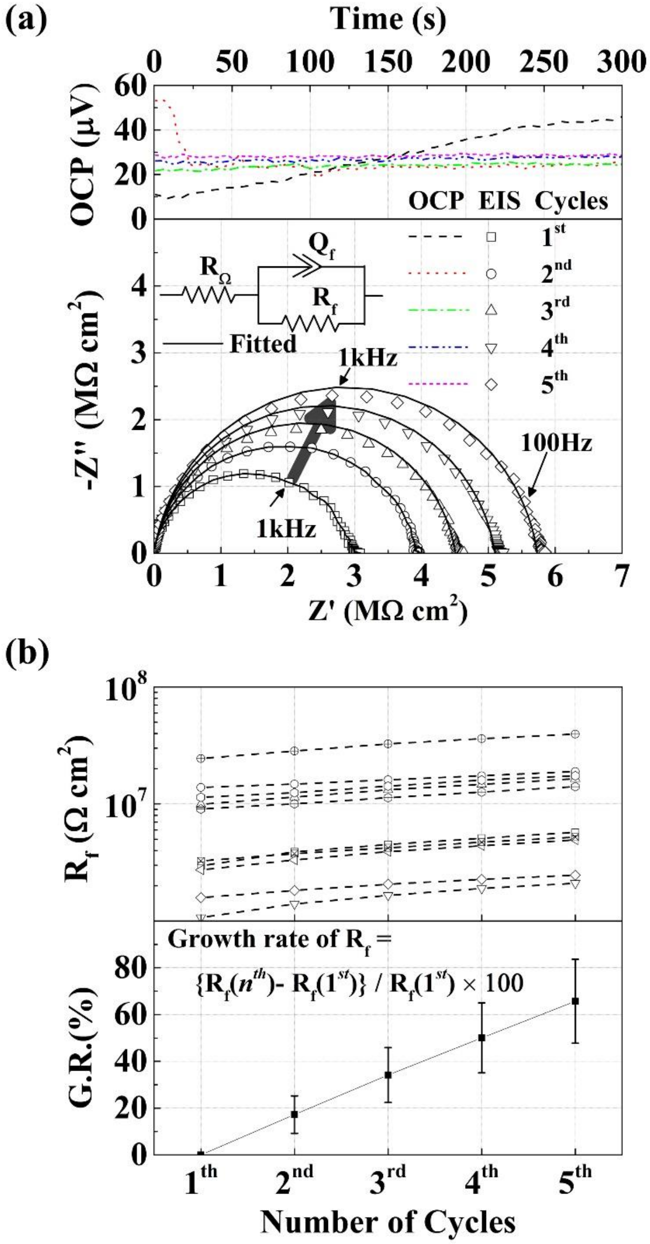

Figure 5.2 ZRP films under a two-electrode system at room temperature in the dry condition: (a) Impedance spectra and potential difference of ZRP films with cyclic tests. (b) Impedance variation of ten ZRP samples and growth rate of impedance at 1 Hz under cyclic tests.

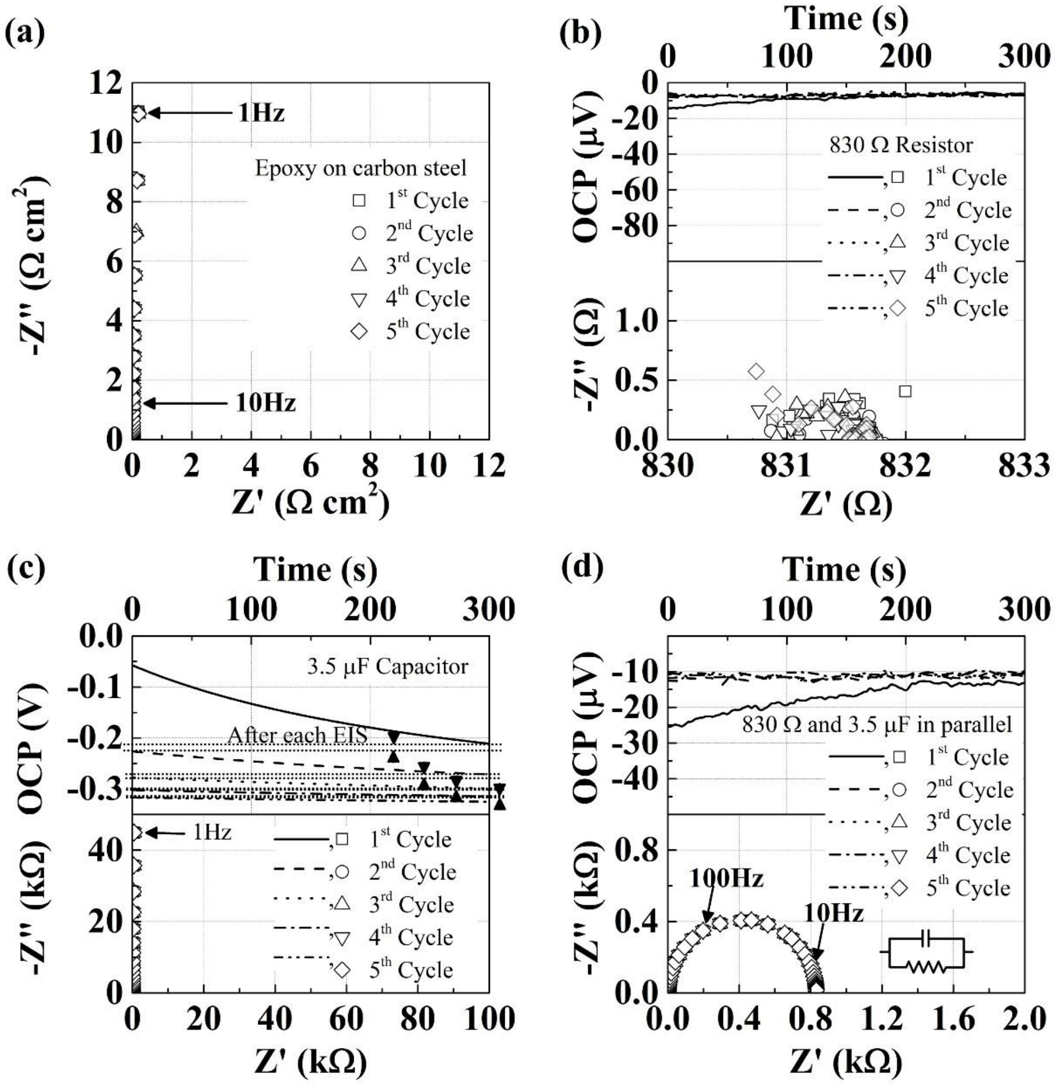

Figure 5.3 Potential difference at open circuit and complex-plane representation of the impedance response of electrical components with a two-electrode system under cyclic tests: (a) Epoxy coating on carbon steel substrate. (b) Resistor of 831 Ω. (c) Capacitor of 3.5 µF. (d) 831 Ω resistor and 3.5 µF capacitor connected in parallel.

Figure 5.3 shows the consecutive impedance spectra for several different systems: epoxy on carbon steel and passive electrical components including a resistor, a capacitor, and resistor-capacitor in an RC configuration. The impedance responses of the systems were unaffected by the electrical cyclic testing. These results illustrate the conventional response of the systems to impedance spectroscopy, as is generally known. The recorded OCP value remained nearly constant at -10 μV for the resistor circuit (Fig. 5.3(b)) and the RC circuit (Fig. 5.3(d)), because the stored energy of the capacitor in the RC circuit was quickly discharged through the resistor. The potential across the capacitor exponentially decayed through the resistor, as explained by the low relaxation time in Kirchhoff's current law. For the capacitor electrical element, a tendency toward decreasing to a potential of -350 mV was observed (Fig. 5.3(c)). The potential in the capacitor circuit was negatively biased with an increase in the test time of the OCP, and the potential was further negatively biased after each EIS test. A possible explanation for this OCP bias may be that the rate of energy storage in the electric field from the deviated signal of an electroanalytical tool was faster than the spontaneous discharge of the capacitor.

5.3.2. Electrical-aspect Interpretation of the Non-conventional Response

To understand the non-conventional phenomenon in detail, we conducted an experiment to observe the EIS response change under various temperatures, as shown in Fig. 5.4. Because the ohmic resistance depends on the temperature, the operating temperature might possibly result in the growth of impedance spectra under electrical cyclic tests. The results, presented in magnitude and phase angle representation in Fig. 5.4, showed that the magnitude of impedance at 1 Hz decreased with increasing temperature. This finding indicates that the operating temperature, which can be assumed to increase under a flowing current through the resistance of the coating during continuous conditioning tests, is not the reason for the growth of impedance spectra in the ZRP coating. The impedance spectra of ZRP films under various temperatures indicate a trend similar to that of a semiconductor. Because thermal energy induces electrons to jump into the conduction band and then freely move, the electrical conductivity of a typical semiconductor increases with increasing temperature, in the range of 20–50 °C [32].

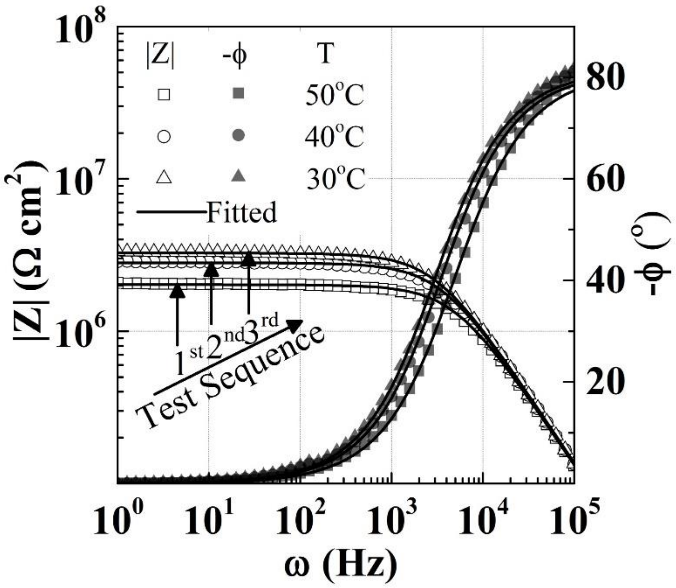

Figure 5.4 Effect of temperature on the magnitude and phase angle images of ZRP films under a two-electrode system in the dry condition. The fitting values of R_f at 50°C, 40°C, and 30°C are $2.022\times10^{6}\ \Omega\ \text{cm}^2$, $2.812\times10^{6}\ \Omega\ \text{cm}^2$, $3.257\times10^{6}\ \Omega\ \text{cm}^2$, respectively.

The pristine ZRP coatings were examined by X-ray diffraction, as shown in Fig. 5.5, in the presence of both zinc and zinc oxide. Native zinc oxide is common in ZRP films and forms on the surfaces of zinc particles during the coating synthesis and application processes [4]. Zinc oxide is a wide-bandgap semiconducting material, and multi-wall CNTs are a quasi-metallic material with a band gap of several dozens of millielectronvolts; thus, the interfaces between both materials could form a Schottky barrier junction, producing a diode effect [29]. The current density through an oxide system/metal interface with single diode-like behavior can be explained as follows [33]:

$$j = \left(\frac{4\pi q m^* k^2}{h^3}\right) T^2 e^{-\frac{q\Phi_B}{k_B T}} \left[e^{\frac{q(V_a - \Delta V)}{n k_B T}} - 1 \right] \tag{5.3}$$

where V_a is the applied voltage powered by the electrochemical analysis machine, ΔV is the voltage drop because of an ohmic semiconductor-metal contact and the bulk resistance of the semiconductor, q is the elementary charge, k_B is the Boltzmann constant, T is the absolute temperature, n is the ideality factor, $m^*$is the charge carrier effective mass, h is Planck's constant, and Φ_B is the Schottky barrier height at the metal/semiconductor interface in volts. On the basis of the previous expression, two driving potentials can be used to explain the change in resistance in the ZRP film. One is V_a, with exponentially proportional current density that can explain the exponential change in conductivity of the ZRP film. Similar behavior of the ZRP films was observed in applied bias potential and in immersion conditions (discussed later in Fig. 5.6 and Fig. 6.7(b)). The other potential is Φ_B, which is exponentially inversely proportional to the current density in Eq. (5.3). Changes in the formed Schottky barrier have been reported during continuous electrical cycles following voltage scans [34, 35]. The changes in the barrier have been described to be due to the slow repositioning of trap charges at perpendicular and parallel interfaces to the changing electrical field.

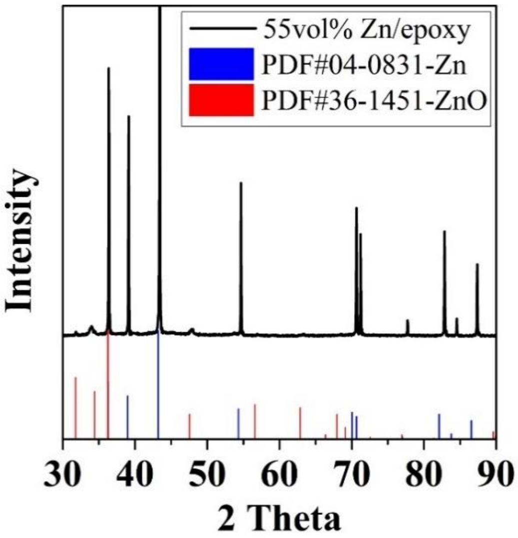

Figure 5.5 XRD of the ZRP film at room temperature in the dry condition.

To characterize the diode-like response of ZRP films and to understand the influence of the applied bias potential (V_a) in the films, we conducted impedance measurements on the ZRP films by using positive and negative bias. The results showed that the resistance of ZRP film, as shown in Fig. 5.6(a), decreased with applied positive bias potential, which had a response analogous to that of a single diode, as indicated in Eq. (5.3). In addition, the ZRP film indicates that the radius of the semicircle decreased with decreasing potential under negative bias (a reverse-bias regime), as shown in Fig. 5.6(b). The DC polarization results illustrated the idea of non-ohmic current-voltage characteristics of the dry film, as presented in Fig. 5.6(c). The upward and downward current responses from the origin at 0 V indicated a decrease in the electrical resistance, which can be seen from the slope of the current-potential curve and showed the same behavior regarding bias potential explained in Figs. 5.6(a) and (b).

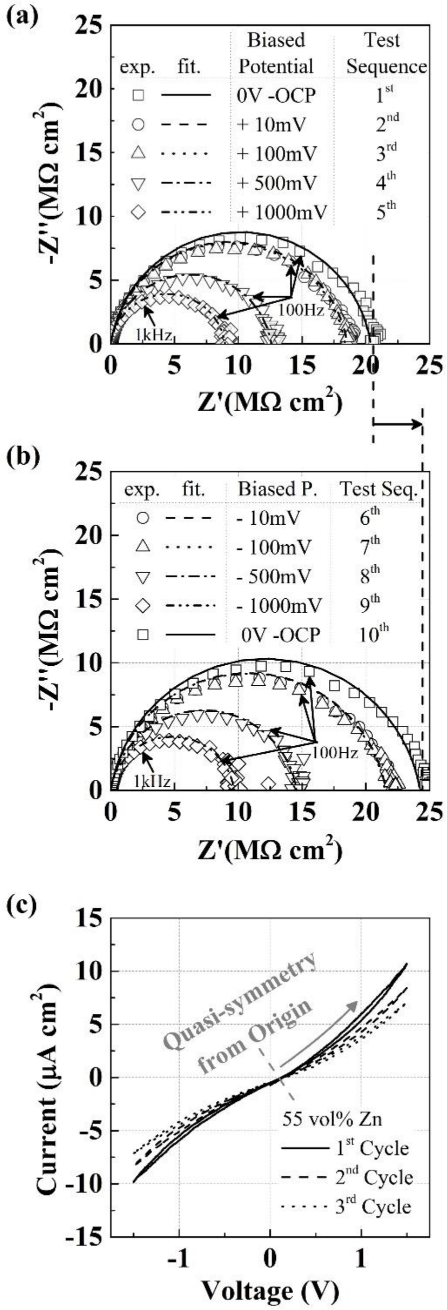

Figure 5.6 ZRP films at room temperature in the dry condition: (a) Impedance spectra of the ZRP film with a two-electrode system in the condition of positive bias potential. (b) Impedance spectra of the ZRP film with a two-electrode system in the condition of negative bias potential. (c) Current-voltage characteristics of the ZRP film in the dry condition (10mV/s scan rate). The voltage at the bottom carbon steel substrate with top CE/RE on the coating was consistent with the applied voltage. The result is described on a linear scale.

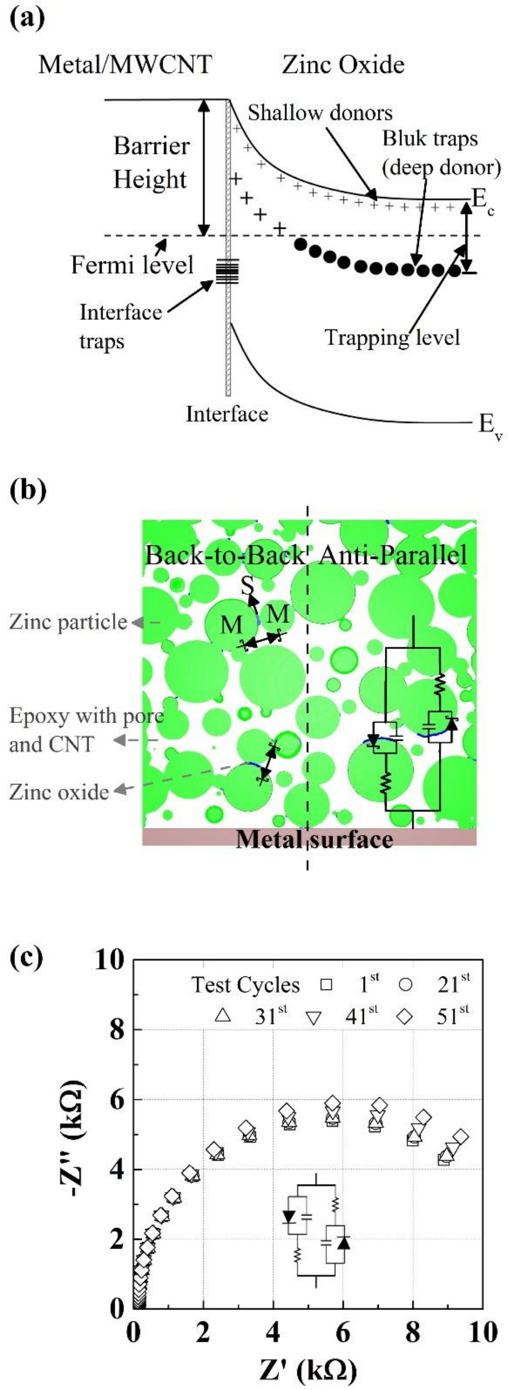

Figure 5.7 (a) The diagram of electron energy level of a metal-zinc oxide interface with a bulk trapping level. (b) Schematic image of the distribution of diode-like materials including back-to-back (Metal-Semiconductor-Metal) Schottky and two diodes in anti-parallel. (c) The similar behavior of the electrical circuit with a diode (IN5820-f-AE45), capacitance (3.5 μF), and resistor (226 Ω) under the cyclic tests.

However, the tendency of the change in electrical resistance of the dry ZRP film under the consecutive electrical tests was different from the decrease in the electrical resistance of the film in response to the applied bias potential. The current density decreased in Fig. 5.6(c) during DC scanning cycles, thus indicating that the electrical resistance of the ZRP film increased. As presented in the first EIS response in Fig. 5.6(a) and the tenth EIS response in Fig. 5.6(b), continuous impedance measurements of the ZRP film using positive and negative-bias also increased the electrical resistance by approximately 5 MΩ cm^2. Thus, the growth of impedance spectra in the dry condition with cyclic electrical conditioning tests appears to be caused not by the applied bias potential but by the increase in the barrier potential. If the barrier height in the ZRP film increases with cyclic conditioning tests, the magnitude of ohmic resistance of the film would increase according to Eq. (5.3), as discussed above.

The barrier height for n-type semiconductors in a no-bias environment is defined as the difference between the Fermi level and interfacial conduction band edge in the electron energy level diagram in Fig. 5.7(a) [37]. The Fermi level within the Schottky barrier denotes the division between positively charged traps and neutral traps. If the positively charged trap in the center of the interface catches a negative electric charge as a neutral process, the barrier becomes lower, but if the neutral trap positioned below the Fermi level catches a carrier, the barrier height is increased. During electrical cyclic conditioning, the trap charges are removed from the field perpendicular interface to other places in response to an external electric field; this effect is due to spatial reoccupation and diminishes the barrier [36]. The spatial repositioning is influenced by the distribution of zinc particles with zinc oxides and their volume fraction, and the trap charge relaxation time of the spatial repositioning can be short at high volume fractions of zinc particles in the ZRP film (55 vol%), owing to good electrical connection. However, the unusual trend in electrical conditioning can be attributed to induced dipole traps. When a neutral trap acquires a positive charge or undergoes polarization reoccupation in response to an external electrical field changing direction according to frequency, an additional dipole trap enhancing the Schottky barrier can be obtained.

In the previous discussion, the physical meaning of the non-conventional response of the dry ZRP film under consecutive electrical testing was examined, and the change in barrier height as a main factor was considered. In addition, electrical responses that positively and negatively bias potential enable a deeper interpretation of the electrical element distributions in the ZRP film. A single diode cannot exhibit quasi-symmetric electrical behaviors, as shown in Fig. 5.6, because the resistance of the single diode as an active element increases after the application of a negative bias potential. The electrical behaviors of ZRP film can be explained by using the spatial distribution of the active elements, which is the anti-parallel superposition of two diodes. Similar quasi-symmetric electrical behavior has also been observed in a back-to-back Schottky diode [38]. The quasi-symmetric behavior about the origin in the current-voltage response can be explained by the physical connections of native zinc oxides between zinc particles or between zinc particles and CNTs as a back-to-back Schottky diode, as well as by the random orientation of native zinc oxides toward or away from the substrate in the epoxy film in Fig. 5.7(b). If we consider two anti-parallel diodes, the equivalent electrical circuit of the film can be considered as two diodes with capacitors and resistors in an anti-parallel connection, as shown in Fig. 5.7(c). A similar trend of increased ohmic resistance was observed in EIS cycling tests by an actual electrical circuit construction using commercial diodes, resistors, and capacitors in Fig. 5.7(c).

5.4. Summary

We used electroanalytical techniques to document the electrochemical responses of a ZRP coating in the presence of a ZnO film with diode-like behavior. From an electrical standpoint, the resistance of the system with ZnO as a native product in the ZRP film is susceptible to exposure to a transfer function signal. Barrier potential and applied bias potential may be important potentials driving the impedance variations in ZRP films observed under electroanalytical cyclic tests. The barrier height, which can be changed as a result of the slow relaxation of polarization reoccupation of traps under an external electrical field through electrical cyclic conditioning, plays a major role in the electrical resistance of ZRP film in the dry condition. The electrical conductivity of the dry ZRP (55 vol%) film decreased during conditioning.

5.5. References

[1] S. Feliu, R. Barajas, J.M. Bastidas, M. Morcillo, Mechanism of cathodic protection of zinc-rich paints by electrochemical impedance spectroscopy. 1. Galvanic stage, Journal of Coatings Technology, 61 (1989) 63-69.

[2] S. Feliu, R. Barajas, J.M. Bastidas, M. Morcillo, Mechanism of cathodic protection of zinc-rich paints by electrochemical impedance spectroscopy. 2. Barrier stage, Journal of Coatings Technology, 61 (1989) 71-76.

[3] W.B. Chen, P. Chen, H.Y. Chen, J. Wu, W.T. Tsai, Development of Al-containing zinc-rich paints for corrosion resistance, Applied Surface Science, 187 (2002) 154-164.

[4] Y. Cubides, H. Castaneda, Corrosion protection mechanisms of carbon nanotube and zinc-rich epoxy primers on carbon steel in simulated concrete pore solutions in the presence of chloride ions, Corrosion Science, 109 (2016) 145-161.

[5] B. Ramezanzadeh, S.Y. Arman, M. Mehdipour, Anticorrosion properties of an epoxy zinc-rich composite coating reinforced with zinc, aluminum, and iron oxide pigments, Journal of Coatings Technology and Research, 11 (2014) 727-737.

[6] A. Gergely, I. Bertoti, T. Torok, E. Pfeifer, E. Kalman, Corrosion protection with zinc-rich epoxy paint coatings embedded with various amounts of highly dispersed polypyrrole-deposited alumina monohydrate particles, Progress in Organic Coatings, 76 (2013) 17-32.

[7] L. Zhang, X.Y. Lu, Y. Zuo, The influence of cathodic polarization on performance of two epoxy coatings on steel, International Journal of Electrochemical Science, 9 (2014) 6266-6280.

[8] H. Marchebois, M. Keddam, C. Savall, J. Bernard, S. Touzain, Zinc-rich powder coatings characterisation in artificial sea water - EIS analysis of the galvanic action, Electrochimica Acta, 49 (2004) 1719-1729.

[9] B. Ramezanzadeh, M.H.M. Moghadam, N. Shohani, M. Mandavian, Effects of highly crystalline and conductive polyaniline/graphene oxide composites on the corrosion protection performance of a zinc-rich epoxy coating, Chemical Engineering Journal, 320 (2017) 363-375.

[10] F. Yang, T. Liu, J.Y. Li, S.H. Qiu, H.C. Zhao, Anticorrosive behavior of a zinc-rich epoxy coating containing sulfonated polyaniline in 3.5% NaCl solution, Rsc Advances, 8 (2018) 13237-13247.

[11] J. Liu, T. Liu, Z. Guo, N. Guo, Y. Lei, X. Chang, Y. Yin, Promoting barrier performance and cathodic protection of zinc-rich epoxy primer via single-layer graphene, Polymers, 10 (2018) 591.

[12] H. Hayatdavoudi, M. Rahsepar, A mechanistic study of the enhanced cathodic protection performance of graphene-reinforced zinc rich nanocomposite coating for corrosion protection of carbon steel substrate, Journal of Alloys and Compounds, 727 (2017) 1148-1156.

[13] S. Park, M. Shon, Effects of multi-walled carbon nano tubes on corrosion protection of zinc rich epoxy resin coating, Journal of Industrial and Engineering Chemistry, 21 (2015) 1258-1264.

[14] A. Gergely, Z. Paszti, J. Mihaly, E. Drotar, T. Torok, Galvanic function of zinc-rich coatings facilitated by percolating structure of the carbon nanotubes. Part II: Protection properties and mechanism of the hybrid coatings, Progress in Organic Coatings, 77 (2014) 412-424.

[15] K. Schaefer, A. Miszczyk, Improvement of electrochemical action of zinc-rich paints by addition of nanoparticulate zinc, Corrosion Science, 66 (2013) 380-391.

[16] A. Meroufel, S. Touzain, EIS characterisation of new zinc-rich powder coatings, Progress in Organic Coatings, 59 (2007) 197-205.

[17] H.W. Shi, F.C. Liu, E.H. Han, The corrosion behavior of zinc-rich paints on steel: Influence of simulated salts deposition in an offshore atmosphere at the steel/paint interface, Surface & Coatings Technology, 205 (2011) 4532-4539.

[18] C. Fernandez-Sanchez, C.J. McNeil, K. Rawson, Electrochemical impedance spectroscopy studies of polymer degradation: application to biosensor development, Trac-Trends in Analytical Chemistry, 24 (2005) 37-48.

[19] X.W. Liu, J.P. Xiong, Y.W. Lv, Y. Zuo, Study on corrosion electrochemical behavior of several different coating systems by EIS, Progress in Organic Coatings, 64 (2009) 497-503.

[20] M. Jalili, M. Rostami, B. Ramezanzadeh, An investigation of the electrochemical action of the epoxy zinc-rich coatings containing surface modified aluminum nanoparticle, Applied Surface Science, 328 (2015) 95-108.

[21] Y. Cubides, S.S. Su, H. Castaneda, Influence of zinc content and chloride concentration on the corrosion protection performance of zinc-rich epoxy coatings containing carbon nanotubes on carbon steel in simulated concrete pore environments, Corrosion, 72 (2016) 1397-1423.

[22] A.H. Sofian, K. Noda, Corrosion resistance and mechanism of zinc rich paint in corrosive media, ECS Transactions, 58 (2014) 29-37.

[23] C.M. Abreu, M. Izquierdo, P. Merino, X.R. Novoa, C. Perez, A new approach to the determination of the cathodic protection period in zinc-rich paints, Corrosion, 55 (1999) 1173-1181.

[24] J.R. Scully, Corrosion chemistry closing comments: opportunities in corrosion science facilitated by operando experimental characterization combined with multi-scale computational modelling, Faraday Discussions, 180 (2015) 577-593.

[25] H.G. Guo, J.Z. Zhou, Z.G. Lin, ZnO nanorod light-emitting diodes fabricated by electrochemical approaches, Electrochemistry Communications, 10 (2008) 146-150.

[26] A. Janotti, C.G. Van de Walle, Fundamentals of zinc oxide as a semiconductor, Reports on Progress in Physics, 72 (2009) 126501.

[27] L. Zhang, Y. Jia, S. Wang, Z. Li, C. Ji, J. Wei, H. Zhu, K. Wang, D. Wu, E. Shi, Carbon nanotube and CdSe nanobelt Schottky junction solar cells, Nano Letters, 10 (2010) 3583-3589.

[28] J. Svensson, E.E. Campbell, Schottky barriers in carbon nanotube-metal contacts, Journal of Applied Physics, 110 (2011) 111101.

[29] A.K. Sharma, R. Sharma, Fabrication and characterization of zinc oxide/multi-walled carbon nanotube Schottky barrier diodes, Journal of Electronic Materials, 47 (2018) 3037-3044.

[30] S. Cho, Y. Cubides, H. Castaneda, Probing the degradation mechanism of a Cr (VI) coating/aluminum alloy 2024-T3 system based on dynamic mechanisms and a 2D deterministic-probabilistic approach, Electrochimica Acta, 236 (2017) 82-96.

[31] A. Miszczyk, K. Darowicki, Water uptake in protective organic coatings and its reflection in measured coating impedance, Progress in Organic Coatings, 124 (2018) 296-302.

[32] H. Bidadi, S.M. Hasanli, H. Hekmatshoar, S. Bidadi, S.M. Aref, Temperature dependence of electrophysical characteristics of zinc oxide based varistors, Vacuum, 84 (2010) 1232-1235.

[33] S.M. Sze, K.K. Ng, Physics of semiconductor devices, John Wiley & Sons, 2006.

[34] X.J. Luo, C.P. Yang, X.P. Song, S.s. Chen, L.F. Xu, K. Bärner, Slow trap charge repositioning processes and the polarization of $CaCu_3Ti_4O_{12}$, Journal of the American Ceramic Society, 94 (2011) 2512-2517.

[35] K. Barner, X.J. Luo, X.P. Song, C. Hang, S.S. Chen, I.V. Medvedeva, C.P. Yang, Correlation between the trap state spectra and dielectric behavior of $CaCu_3Ti_4O_{12}$, Journal of Materials Research, 26 (2011) 36-44.

[36] X. Luo, C. Yang, S. Chen, X. Song, H. Wang, K. Baerner, The trap state relaxation related polarization in $CaCu_3Ti_4O_{12}$, Journal of Applied Physics, 108 (2010) 014107.

[37] J.F. Cordaro, Y. Shim, J. May, Bulk electron traps in zinc oxide varistors, Journal of Applied Physics, 60 (1986) 4186-4190.

[38] S. Sinha, S. Kumar Chatterjee, J. Ghosh, A. Kumar Meikap, Semiconducting selenium nanoparticles: Structural, electrical characterization, and formation of a back-to-back Schottky diode device, Journal of Applied Physics, 113 (2013) 123704.

6. NON-CONVENTIONAL ELECTROCHEMICAL IMPEDANCE BEHAVIOR[*]

6.1. Overview

Non-conventional responses in the impedance spectra of a zinc-rich coating system were also observed in electrochemical impedance measurements that have previously been considered to have no effect on the system. Despite the impressive progress in zinc-rich coating systems to control corrosion in metal structures through galvanic effects, some physical properties influencing the responses of electrochemical systems remain unexplored. Electrochemical cells on zinc-rich (55 vol%) coatings with multi-wall carbon nanotube systems were analyzed to determine the intrinsic response of the coating with electrical passive and active analogs under electrical conditioning cycles. During immersion, the change in impedance of the zinc-rich primer (ZRP) film under consecutive electrochemical sequences differed from that under natural degradation. This non-conventional response of the ZRP coating was influenced by the applied bias potential. The capacitive behavior influenced by the zinc corrosion products in the coating had a longer relaxation time, thus decreasing the open circuit potential. To understand this phenomenon, we propose a charging-relaxation potential model. In addition, the potential exhibited a change in the electrical resistance of the ZRP film during consecutive electrochemical testing.

---

[*] Part of this section is reprinted with permission from “Electrical and electrochemical behavior of a zinc-rich epoxy coating system with carbon nanotubes as a diode-like material” by Seongkoo Cho, Tse-Ming Chiu, Homero Castaneda, 2019. *Electrochimica Acta*, 316, 189-201, Copyright © 2019 by Elsevier Ltd.

In this work, the effects of EIS measurement on CNT-added ZRP film were studied under immersed conditions through electrochemical cyclic sequences. We observed non-conventional electrochemical film responses and characterized two critical points: (i) the electrochemical response analysis of the immersed coating in electrochemical sequencing tests; and (ii) the charging/relaxation behavior during EIS testing.

6.2. Experimental Methods

6.2.1. Materials and Sample Preparation

Test samples were prepared using the method used in Chapter 5.2.1.

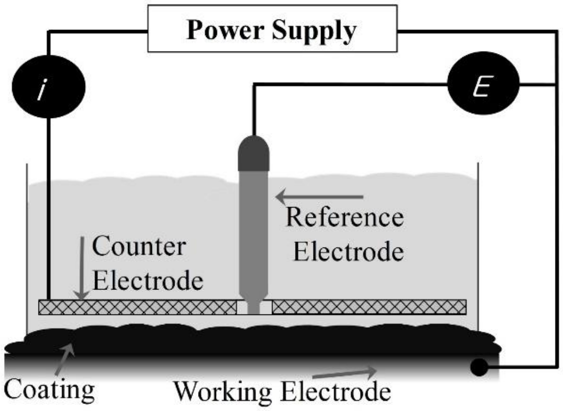

Figure 6.1 The standard flat cell of the three-electrode system at the immersed condition.

6.2.2. Electrochemical Measurements in Immersed Condition

Full immersion testing was performed with a standard flat cell with an exposed area of 7.07 cm^2. Steel-coated panels were used as the working electrode, platinum mesh was used as a CE, and a saturated calomel electrode (SCE) was used as a RE (illustrated in Fig. 6.1). All immersion measurements were performed in 3.5 wt% NaCl solution at room temperature for 25 days. To understand the charging and relaxation effects of electrochemical measurement on the ZRP film, we performed two electrochemical sequence testing procedures during full immersion conditions. For each day, procedure A (four specimens) included a 1-hour loop test followed by 23 hours of relaxation, procedure B (four specimens) included the 12 loop tests (1 hour per loop) followed by 12 hours of relaxation, and procedure C (four specimens) included single loop test at the end of immersion. Each loop included 20 min of OCP followed by EIS at a range of frequencies between 100 kHz and 10 mHz (10 points per decade interval) and an amplitude of 10 mV (rms) vs OCP. All electrical and electrochemical measurements were mainly conducted with a Gamry Interface 1000, and to avoid any influence due to instrumentation, different potentiostats, such as Biologic SP-200 and Ametek VersaStat 3F, were used. The results of the EIS experiment were fitted in Ec-Lab® software, and chi-square tests were used to analyze the fitting error.

6.3. Results and Discussion

6.3.1. Conventional and Non-conventional Impedance Response in the Immersed Condition

The degradation mechanism of the ZRP coating/carbon steel system immersed in the 3.5 wt% NaCl solution can be illustrated by the EIS data according to procedure A.

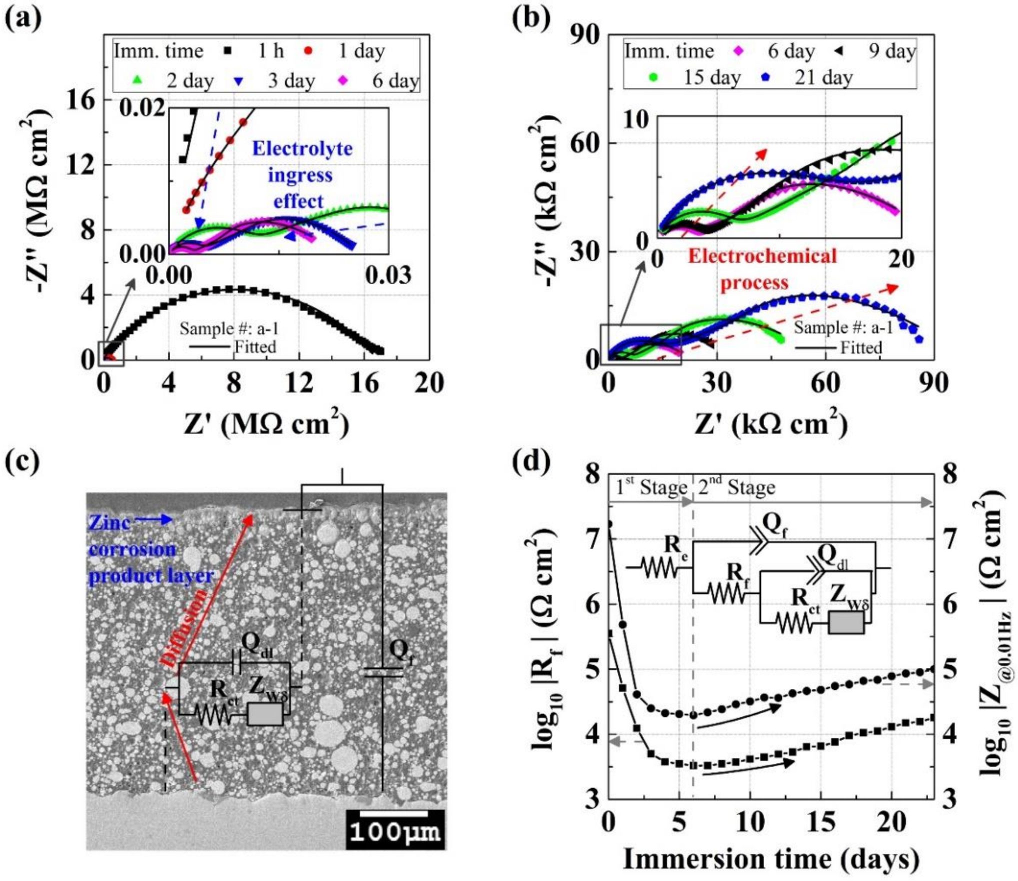

Figure 6.2 Degradation process on the impedance response of ZRP coating/carbon steel system immersed in 3.5 wt% NaCl solution: (a) Nyquist diagram and Bode diagram between the 1st and 6th immersion day in the condition of procedure A. (b) Nyquist diagram and Bode diagram between the 6th and 21st immersion day in procedure A. (c) Cross-section SEM image of a ZRP/CNT coating with transmission line at 24th immersion day. (d) Equivalent circuit element R_f of coating resistance and impedance at 0.01Hz with immersion time.

The EIS plots for 21 days of immersion are illustrated in Figs. 6.2(a) and (b). Fig. 6.2(a) shows that the initial degradation stage was influenced by the electrolyte transport within the coating. The water transport with existing free ions in the pores influenced the bulk film electrical resistance. The charge transfer and diffusion processes occurred at the interface between the electrolyte and zinc particles, as illustrated in Fig. 6.2(c) [1]. These mechanisms are represented in the first and second semicircles of the responses of the impedance, respectively. As a results of mass transfer to charge transfer mechanism, the zinc reaction products fill the ZRP film pores, and the active zinc-to-steel area ratio is decreased after the ZRP film fully saturates with electrolyte [2]. This phenomenon subsequently increases the impedance magnitudes of both loops formed during the exposure time, as illustrated in Fig. 6.2(b). The EIS results were fitted with an equivalent circuit analog, as shown in Fig. 6.2(d) [1]. The time constant, which can be attributed to the time-invariant first-order linear system, at higher frequencies reflects the physical properties of the coating, including the formation of corrosion product, whereas the electrochemical processes dominate the responses at lower frequencies [1, 3-5]. The equivanlent circuit is composed of R_f, Q_f, charge transfer resistance (R_{ct}), CPE (Q_{dl}) for a double layer capacitor, electrolyte resistance (R_e), and the bounded Warburg impedance ($Z_{w\delta}$), owing to the finite length diffusion process within the zinc corrosion products [6]. CPEs ($Q_i, i = \mathrm{f}$ or dl) and $Z_{w\delta}$ are given by the following expressions;

$$Q_i = \frac{1}{Q_{0i}(i\omega)^n}\ ,(0 \leq n \leq 1) \tag{6.1}$$

$$Z_{w\delta} = \frac{R_d \tanh\sqrt{\tau_d i\omega}}{\sqrt{\tau_d i\omega}} \tag{6.2}$$

where Q_{0i} (F $\mathrm{s}^{\mathrm{n}-1}$ cm^{-2}) is the constant of CPE. τ_d (s) is the characteristic diffusion time in finite layer thickness, and $R_d/\sqrt{\tau_d}$ (Ω cm^2) is the Warburg coefficient. The fitting errors of the experimental data were smaller than 0.008. As represented in Fig. 6.2(d), the R_f fitting magnitude (high frequency region) and the lowest frequency impedance magnitude at 0.01 Hz tended to increase with increasing immersion time during the second stage of degradation. This result is in agreement with the classical coating degradation mechanism described in previous studies [2, 6].

The response of the immersed sample in EIS measurements is generally expected to describe the current state of the sample in steady state conditions. As previously described, changes in the EIS responses over time have been used as an important tool to explain the natural degradation mechanism of CNT-added ZRP samples.

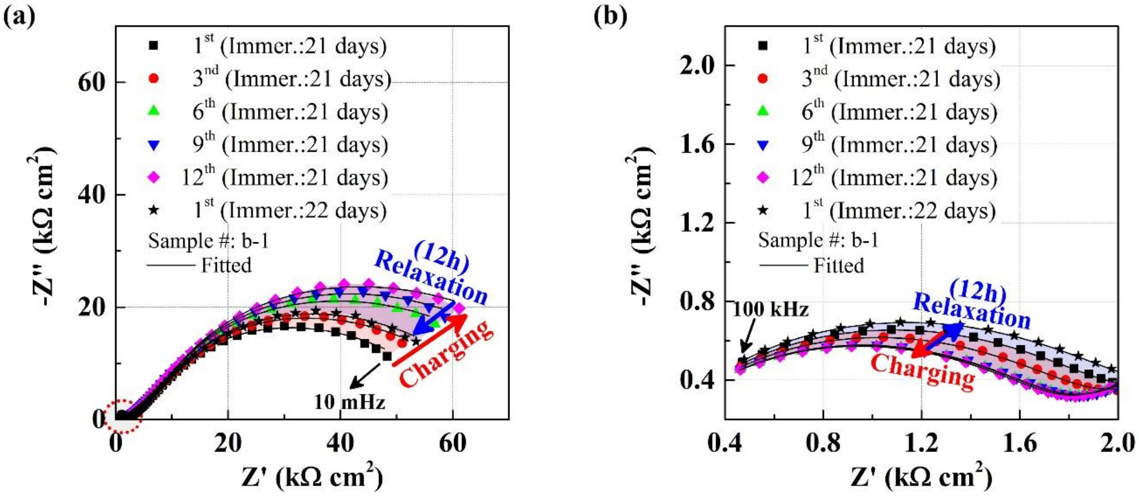

Figure 6.3 The impedance response of ZRP coating/carbon steel system immersed in 3.5 wt% NaCl solution in continuous electrochemical conditioning tests (Procedure B): (b) Magnified view of Nyquist image (a) close to high frequency region at 21st and 22nd immersion day.

However, the impedance change of the ZRP sample responds differently during the second stage compared with the one expressed by the conventional natural degradation mechanism when the sample follows the procedure B, as shown in Fig. 6.3. Whereas conventional electrochemical testing showed increased high-frequency impedance magnitude during the second stage, a decrease in high-frequency impedance magnitude was observed with increasing immersion time under consecutive electrochemical testing, as shown in Fig. 6.3(b). Additionally, the first and second capacitive loops at the high and low frequency regions, respectively, moved away from the initial response, and were accompanied by the loop size changes, as the electrochemical experiment continued (red arrow in Fig. 6.3). However, the impedance spectra of the sample after the 12 hours of relaxation, as shown in the first impedance spectra of the 22nd immersion day (blue arrow in Fig. 6.3), tended to return to the initial state of the response, as shown in the first impedance spectra on the 21th immersion day. These trends were not expected, and some physical properties of the ZRP film in the electrochemical system might reasonably be concluded to have been influenced by the non-destructive electrochemical technique.

6.3.2. Charging-relaxation Effects of a ZRP Film under Consecutive Electrochemical Conditioning

In an aqueous environment, the presence of the ZnO film was clear, as shown in Fig. 6.4. The intensity ratio of Zn/ZnO varied slightly among samples, but the higher XRD intensities of the ZnO product were similar to the intensities of samples in the dry condition. The *E-pH* diagram of Zn in an aqueous medium [7] indicates that ZnO formation is thermodynamically feasible in an electrolyte solution with a pH between 8 and 10 (experimentally observed) and potentials between -1 and -0.85 V vs SCE. Most of the zinc oxides as corrosion products were formed on the top of the ZRP film, as depicted in Fig. 6.4(b) and (c) at location S1. The layer structure, in a darker color, was also found partially covering Zn particle/epoxy interface (location S2), which was higher in chloride content; this compound may be the zinc hydroxychloride compound seen through XRD in Fig. 6.4(a). The zinc hydroxychloride compound has a band gap energy of 2.4 eV after N doping [8], which is slightly smaller than the energy of ZnO (3.3 eV), but it is also considered a semiconductor.

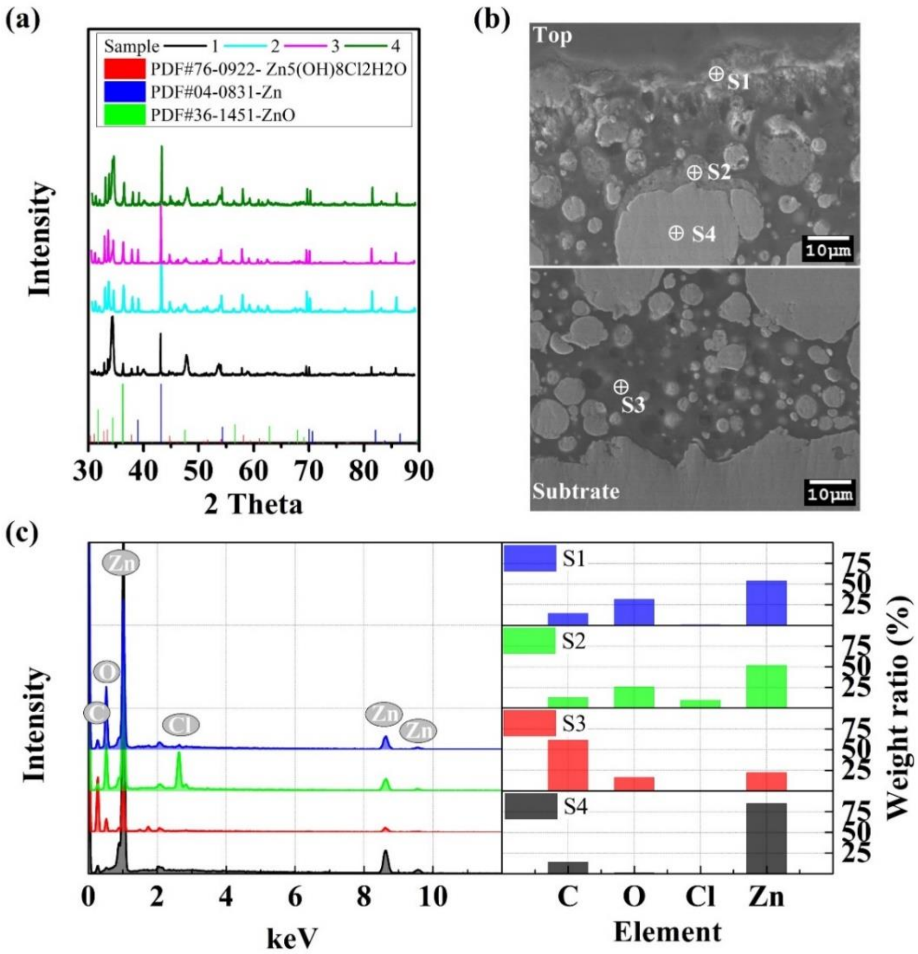

Figure 6.4 The ZRP/CNT films after 24 days of immersion: (a) XRD. (b) Cross-section SEM image of a ZRP coating; S1(corrosion product on the top surface of the ZRP film), S2(corrosion product on the zinc particle), S3(epoxy primer), and S4(zinc particle). (c) EDS on S1, S2, S3, and S4 of the SEM image of (b).

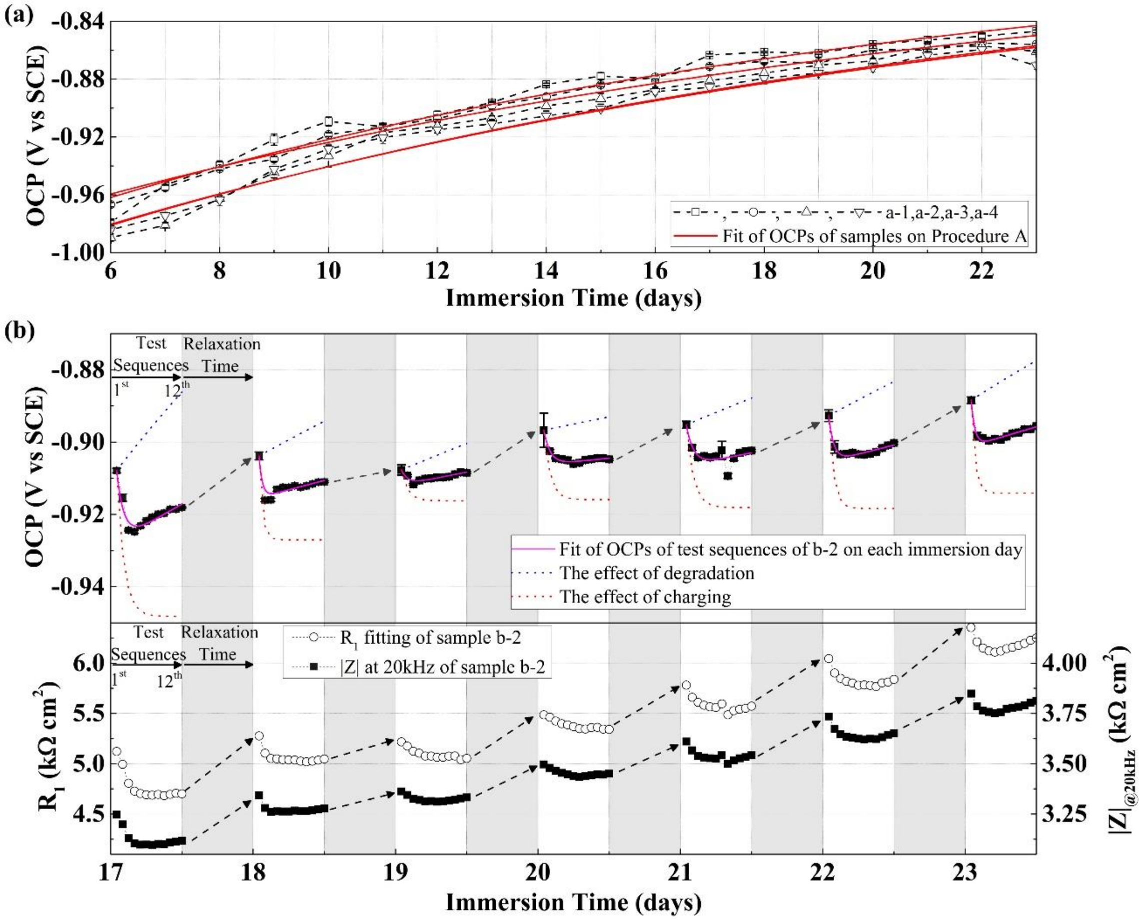

Figure 6.5 Global and local variations of ZRP films in electrolyte solution on electrochemical tests: (a) The global change in OCP of ZRP films with one sequence test per day during cathodic protection period (Procedure A). (b) The local change in OCP and impedance responses at high-frequency capacitive loop dependent on electrochemical conditioning sequential tests (Procedure B).

The ZnO-electrolyte interface plays an important role in the distribution of charges and potentials [9]. As shown in Fig. 6.5(a), the general trend of the OCP from the macroscopic natural degradation process during cathodic protection period of ZRP film gradually shifts positively, owing to the decrease in the area ratio of the active zinc particles after the uptake of water by the electrolyte, thus producing a protective layer on carbon steel [2]. However, contrasting behavior of OCP during the electrochemical cycling conditioning tests was observed in Fig. 6.5(b). The results showed that the coated system was cathodically biased during the continuous EIS conditioning test loop. These OCP local variations in the ZRP film in 3.5 wt% NaCl solution may be explained by a charging-relaxation potential model. Through mixed potential theory, the kinetics of every simultaneous electrochemical reaction can normally be used to explain the OCP of the reactive electrode. The charging-relaxation potential model assumes that the effect of the free degradation on the OCP value during the sacrificial period of zinc particles for corrosion protection mainly depends on the surface area ratio of the anode (active zinc particles) to the cathode (carbon steel). Thus, the potential at the double-layer region between the metal and electrolyte is altered by the surface change, owing to the formation of corrosion products, a phenomenon that can be explained by classical mixed potential theory incorporating the Frumkin effect [10]. The OCP, which can be obtained by setting the sum of anodic and cathodic current densities with the Frumkin effect to zero and solving for the potential of the electrode, is given by [11]

$$
\begin{aligned}
E_1(t) &= \frac{(1-\alpha_a)E_a^0 + \alpha_c E_c^0}{1-\alpha_a+\alpha_c} + \frac{1}{1-\alpha_a+\alpha_c}\frac{k_B T}{q}\ln\left(\frac{n_c k_c[Ox]}{n_a k_a}\right) + \frac{\alpha_a - z_c}{1-\alpha_a+\alpha_c}\phi_2 \\
&= A + B\phi_2(\mathrm{t}) \qquad (6.3)
\end{aligned}
$$

where t (h) is immersion time, α_a and α_c are the anodic and cathodic electron transfer coefficients, respectively, E_a^0 and E_c^0 are the formal potentials, n_a and n_c are the number of electrons transferred, k_a and k_c are the reaction rate constants, $[Ox]$ is the bulk concentration of the oxidation state of the oxidizer in the electrolyte, and z_c is the charge of the oxidation. $\phi_2(t)$ is the potential at the outer Helmholtz plane, which continuously experiences a change in the superimposed charging process of the double layer. To express $\phi_2(t)$ simply and mathematically, we assume that it can be considered a cumulative function because the geometric distribution of zinc/zinc corrosion products and CNTs for cathodic protection process evolves stochastically over time, and the change in the surface area ratio of zinc to corrosion products is a continuous and irreversible process. Because an exponential distribution is a tractable cumulative distribution function, the OCP change from cathodic protection can be written in Eq. (6.4).

$$E_1(t) \quad = A_1 + B_1(1 - e^{-(t-t_c)/\tau_1}) \tag{6.4}$$

$$= a_0 + B_1 e^{-(t_0-t_c)/\tau_1} - B_1 e^{-(t-t_c)/\tau_1} \tag{6.5}$$

where t_c (h) is the initial time for the cathodic protection curve, τ_1(h) is the characteristic time of the degradation on the cathodic protection of the ZRP film, A_1(V vs SCE) is an OCP at t_c, and B_1(V) is an increasing potential coefficient for cathodic protection. If the initial OCP at the first sequence time (t_0) of electrochemical conditioning tests is a_0, E_1 can be redefined as written in Eq. (6.5). During the electrochemical continuous conditioning tests, the ZRP film charges until reaching the capacitive limit, which is an electric field strength limit that determines the maximum amount of energy stored by the ZRP film. This charging is because zinc corrosion product interface formed on top of the ZRP film acts as a diode with capacitive behavior that controls the direction of current flow and has a longer relaxation time than resistance with a capacitor from the small sinusoidal potential excitation signal of an electroanalytical technique. The voltage of a capacitor discharging through a resistor decays rapidly as an exponential function of time, but the voltage decay is a logarithmic function of time in a diode-capacitor circuit [12]. Thus, this ZRP coating system shows a lack of relaxation of charge distribution under continuous cycling conditioning, and the negative bias through charge recombination can be considered in local OCP trends. The charging effect of capacitive behavior on potential can be defined according to Eq. (6.6).

$$E_2(t) \quad = a_0 - B_2(1 - e^{-(t-t_0)/\tau_2}), \qquad (t > t_0) \tag{6.6}$$

where τ_2(h) is the characteristic time of the capacitive charging effect of the ZRP film, and B_2(V) is a decreasing potential coefficient for charging. The local OCP change of the ZRP film on the cyclic conditioning tests can be expressed by a charging-relaxation potential relationship.

$$E_{OCP}(t) \quad = 1/2(E_1(t) + E_2(t)) \tag{6.7}$$

$$= a_0 + \frac{B_1}{2} e^{-(t_0-t_c)/\tau_1} - \frac{B_1}{2} e^{-(t-t_c)/\tau_1} - \frac{B_2}{2}(1 - e^{-(t-t_0)/\tau_2}), \qquad (t > t_0) \tag{6.8}$$

The overall charging-relaxation potential model is depicted in Fig. 6.6. The blue line (Eq. (6.5)) describes the effect of degradation of the ZRP film during the relaxation time, and the red line (Eq. (6.6)) represents the effect of the charging behavior of the ZRP system during continuous electrochemical conditioning. The black line in Fig. 6.6 is represented by the combination of two mechanisms, which is described by Eq. (6.8). The combination gives rise to the OCP patterns between the “V” and “L” trend of the

ZRP film in the continuous conditioning tests in Fig. 6.5(b). Because the relaxation time of energy stored in the capacitive behavior of the ZRP/CNT-coated system with corrosion byproducts is longer than the time interval between experiments, the system accumulates energy from the electrical signal of the electroanalysis machine and shifts the electrode potential in the negative direction during continuous electrochemical conditioning.

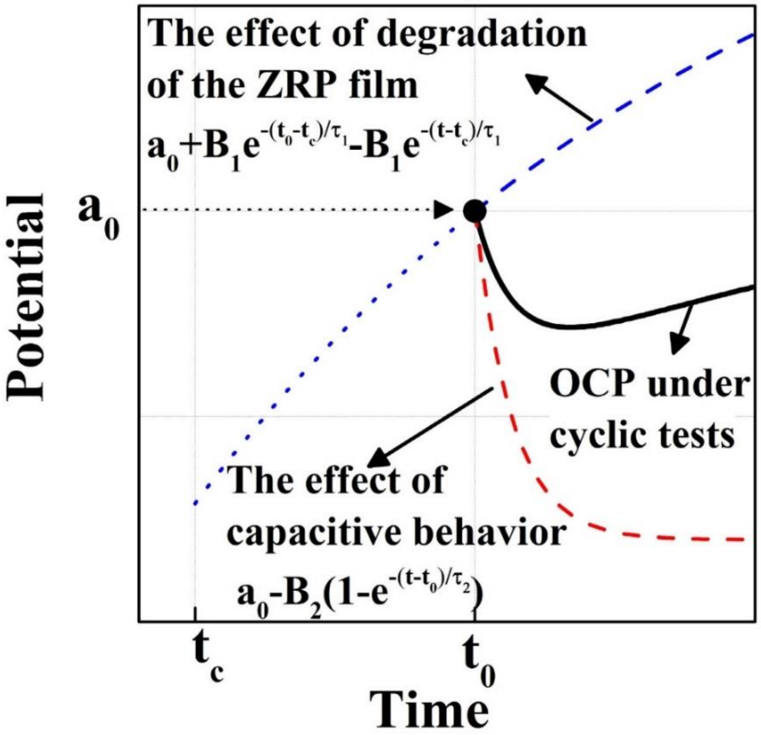

Figure 6.6 Schematic diagram of the charging-relaxation potential model of a ZRP film in the condition of immersion for representing norms.

Table 6.1 Parameters values used for the fitting procedure in Fig. 6.5.

Test (#)	Imm. (days)	a_0 (V)	B_1 (V)	t_0 (h)	t_c (h)	τ_1 (h)	B_2 (V)	τ_2 (h)
A (a-1)	6~23	-0.8559	0.1816	481	145	384	N/A	N/A
A (a-2)	6~23	-0.8625	0.1794	481	145	432	N/A	N/A
A (a-3)	6~23	-0.8711	0.2012	481	145	424.8	N/A	N/A
A (a-4)	6~23	-0.8721	0.2002	481	145	432	N/A	N/A
B (b-2)	17	-0.9079	6.4837	409	145	70	0.0403	1.2119
	18	-0.9038	1.0378	433	145	135	0.0232	0.55
	19	-0.9077	0.6849	457	145	185	0.0085	1.0865
	20	-0.8967	0.3119	481	145	340	0.0192	1.0842
	21	-0.8952	1.0175	505	145	165	0.0229	1.2308
	22	-0.8927	2.2274	529	145	130	0.0257	0.8598
	23	-0.8884	4.7177	553	145	110	0.0257	0.6385

The parameters of the fitting drawn in Fig. 6.5 are summarized in Table 6.1. To observe the natural degradation phenomenon mainly through electrochemical testing of the ZRP film, it is necessary to avoid the accumulating energy, denoted by B_2 and τ_2, during consecutive electrochemical conditioning. A longer sampling time rather than consecutive electrochemical experiments is required to understand the natural degradation mechanism of ZRP film in the immersed condition, because the longer sampling time provides an appropriate relaxation time to remove the charging effect caused by the electroanalytical technique. During the relaxation time of 12 hours, the OCP value shifted toward a more positive potential, owing to the combined effect of degradation and discharging from accumulated energies in Fig. 6.5(b). The film resistance and impedance responses at high frequency follow the trends of the OCP changes of the film in the sequences of electrochemical conditioning and relaxation. The negatively biased OCP due to the charging effect plays a role in an applied bias potential in the impedance tests, which were conducted at an amplitude of 10 mV (rms) around the OCP. Thus, the negatively biased OCP affects the impedance response of active electrical components, as shown in Fig. 6.5(b).

To further explore the influence of polarization on the film in electrolyte solution, we conducted EIS tests, with the function of a bias potential between -100mV (vs OCP) and +100mV (vs OCP), at a single frequency (20kHz), which is the peak point of the high-frequency loop in Fig. 6.7(a). The results in Fig. 6.7(b) indicate the same phenomenon as the impedance response of continuous cycling conditioning in Fig. 6.5(b). A more negative bias potential resulted in a decrease in the magnitude of the impedance response at the peak point of the high-frequency loop. Notably, the impedance magnitude of ZRP films in the high-frequency region exponentially decreased with decreasing potential, as shown in Fig. 6.7(b), similarly to the impedance response of a single diode with respect to an applied bias potential. Penetration of the electrolyte inside the pores of the ZRP films can form an electrical network with zinc and cause the formation of zinc corrosion products toward the substrate.

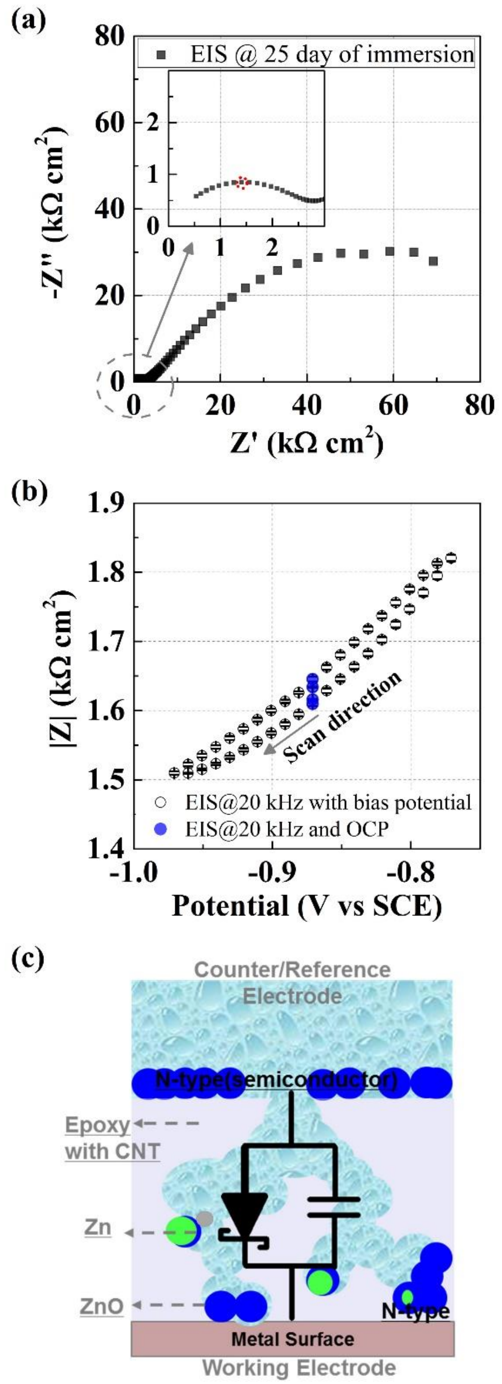

Figure 6.7 The effect of the bias potential on the ZRP film with ZnO at 25 days of immersion: (a) EIS image. (b) Magnitude plots at the peak point of the high-frequency loop with bias potential at the end of immersion. (c) Schematic image of the distribution of diode-like materials in the electrolyte solution.

Thus, one diode oriented with a capacitor can be proposed as the equivalent electrical circuit model of the ZRP film in the electrolyte solution, as illustrated in Fig. 6.7(c). Thus, as discussed above in Eq. (5.3), the charging phenomena during electrochemical conditioning tests can be identified as a negative bias environment, which leads to a decrease in impedance in the high-frequency capacitive loop in Fig. 6.5(b).

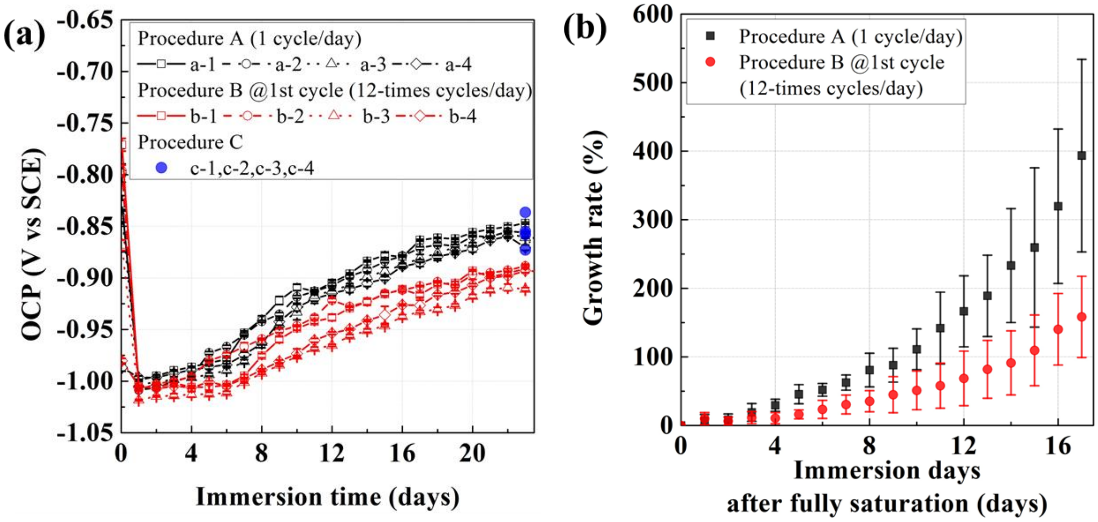

Figure 6.8 The long-term effect of electrochemical tests on the ZRP film immersed in the electrolyte: (a) OCP. (b) Growth rate of the peak point in the high-frequency capacitive loop.

Fig. 6.8 shows the long-term effects of bias on the charge distribution at the ZnO-electrolyte interface from continuous EIS sampling. For test procedures A and C, the OCP values were about -0.86 V (SCE) at the end of the testing period. However, the average OCP of the ZRP film for procedure B is -0.90 V (SCE). The results show that the coated system is cathodically polarized during the continuous EIS test loop because of the capacitive behavior of the system with ZnO. The relaxation of charge distribution occurs slowly in the negative bias through charge recombination. As we discussed before, the voltage of a capacitor discharging through a resistor decays fast as an exponential function of time. However, the voltage decay is a logarithmic function of time in a diode-capacitor circuit. This ZRP coating system shows a lack of relaxation under continuous cycling tests. This results in an OCP difference of 40 mV at the end of immersion. These accumulated energies in the coated system result in the delay of the corrosion process of the zinc particles (Fig 6.8(b)). The growth rate can be defined by the proposed expression:

$$G.R.(\%) = \frac{|Z|_s - |Z|_{ss}}{|Z|_{ss}} \times 100 \tag{6.9}$$

where $|Z|_s$ and $|Z|_{ss}$ are the impedance magnitudes of the peak point of the high-frequency capacitive loop at a specific immersion day after full saturation with the electrolyte and on the day of full saturation, respectively. The growth rate represents the percentage of impedance growth in the high-frequency region, which is related to the production rate of corrosion products of zinc to fill the voided space in the coated system. The ZRP-coated systems in the cycling tests (procedure B) shows a lower growth rate than the ZRP films in the condition of procedure A. Since the relaxation time of energy stored in capacitive behavior of the ZRP-coated system with zinc oxides is long, the system accumulates the energy from the electrical signal of the electroanalysis machine and shifts the electrode potential in the negative direction during continuous tests, mentioned above. Thus, there is a possibility that the combination of effects of this accumulated bias environment and short-term bias in potential occur at a lower growth rate of impedance response in the high-frequency capacitive loop.

6.4. Summary

We used electroanalytical techniques to document the electrochemical responses of a ZRP coating in the presence of a ZnO film with diode-like behavior. From an electrochemical standpoint, the resistance of the system with ZnO as a corrosion product in the ZRP film is susceptible to exposure to a transfer function signal. The applied bias potential was the main factor underlying the inconsistent electrochemical response of the ZRP film under the cyclic conditioning, owing to the formation of zinc corrosion products with electrolyte penetration. To understand the changes in OCP under consecutive testing, we propose a charging-relaxation potential model. The putatively non-destructive electrochemical measurements affected the overall results of the film resistance of the ZRP-coated system: charging effect of capacitive behavior on the potential was observed when a continuous testing procedure was applied, and the applied bias potential followed the change in OCP. Thus, longer sampling times for electroanalytical tests are necessary to observe the pure degradation process.

6.5. References

[1] H.W. Shi, F.C. Liu, E.H. Han, The corrosion behavior of zinc-rich paints on steel: Influence of simulated salts deposition in an offshore atmosphere at the steel/paint interface, Surface & Coatings Technology, 205 (2011) 4532-4539.

[2] C.M. Abreu, M. Izquierdo, M. Keddam, X.R. Novoa, H. Takenouti, Electrochemical behaviour of zinc-rich epoxy paints in 3% NaCl solution, Electrochimica Acta, 41 (1996) 2405-2415.

[3] Y. Cubides, S.S. Su, H. Castaneda, Influence of zinc content and chloride concentration on the corrosion protection performance of zinc-rich epoxy coatings containing carbon nanotubes on carbon steel in simulated concrete pore environments, Corrosion, 72 (2016) 1397-1423.

[4] C.M. Abreu, M. Izquierdo, P. Merino, X.R. Novoa, C. Perez, A new approach to the determination of the cathodic protection period in zinc-rich paints, Corrosion, 55 (1999) 1173-1181.

[5] A.H. Sofian, K. Noda, Corrosion resistance and mechanism of zinc rich paint in corrosive media, ECS Transactions, 58 (2014) 29-37.

[6] A. Meroufel, S. Touzain, EIS characterisation of new zinc-rich powder coatings, Progress in Organic Coatings, 59 (2007) 197-205.

[7] K. Wipperman, J.W. Schultze, R. Kessel, J. Penninger, The inhibition of zinc corrosion by bisaminotriazole and other triazole derivatives, Corrosion Science, 32 (1991) 205-230.

[8] J. He, J. Hu, X. Mo, Q. Hao, Z. Fan, G. He, Y. Wang, W. Li, Q. He, Novel photocatalyst nitrogen-doped simonkolleite $Zn_5(OH)_8Cl_2 \cdot H_2O$ with vis-up-conversion photoluminescence and effective visible-light photocatalysis, Applied Physics A, 125 (2019) 3.

[9] J.F. Dewald, The charge distribution at the zinc oxide-electrolyte interface, Journal of Physics and Chemistry of Solids, 14 (1960) 155–161.

[10] A.J. Bard, L.R. Faulkner, J. Leddy, C.G. Zoski, Electrochemical methods: fundamentals and applications, John Wiley & Sons, 1980.

[11] Z. Chen, The open-circuit potential of a polarizable and reactive electrode, ECS Transactions, 6 (2008) 1-15.

[12] E.H. Hellen, Verifying the diode-capacitor circuit voltage decay, American Journal of Physics, 71 (2003) 797-800.

7. CONCLUSIONS AND FUTURE RECOMMENDATIONS

7.1. Conclusions

To understand and analyze the non-ideal and non-conventional impedance spectra that appear through electrical and electrochemical coating materials, this research investigated through theoretical and experimental approaches. Physicochemical properties related to impedance were designed and examined through various physical correlations within the coating in order to extract the physical processes that can be understood through various non-ideal and non-conventional impedance spectra of coated materials. The findings of this study can be summarized as follows.

- The first approach is to construct a two-dimensional impedance model that allows interpretation of the limited information that is difficult to analyze in one dimensional domain. Such deterministic and probabilistic 2D impedance model can be a tool to understand the effect of pore distribution in the coating space on impedance spectra. The pore distribution in the impedance model is used to reveal the electrolyte penetration ratio along with experimental results. The spatial and interfacial distributions of electrical material properties and electrochemical properties, respectively, of the 2D impedance model explain the physical and electrochemical degradation processes.
- The influence of the distribution of inter-correlated electrical properties inside the bulk coating system on non-ideal impedance response is studied. The

distributions of electrical properties such as electrical conductivity and permittivity on the impedance model are controlled by designing multivariate random variables through Copula. To understand the non-ideal spectra of the dry coating system, the distortion of impedance spectra in the Nyquist plot is mathematically expressed through aspect ratio, and the characteristics of the system are defined by using characteristic frequency. The degree of heterogeneity within the coating is found to affect the aspect ratio of the impedance spectra through the correlation coefficient of electrical conductivity and z-direction position as well as CV values of electrical properties. In addition, the correlation coefficient between log-normal electrical conductivity and log-normal permittivity for impedance spectra explains approaching the characteristic frequency and aspect ratio of the impedance spectra to the ideal response when it is close to the positive linear relationship between the two electrical properties.

- To understand the localized impedance spectra responding through the local defect generated by a scratch, a modified two-dimensional impedance model based on nodal analysis with charge conservation is proposed. The modified model explains the relationship with the localized impedance response to the electrolyte conductivity in the distribution of the local defect by considering the measurement current distribution inside of the system. This study not only suggests appropriate electrical solution conductivity for interpretable local measurement resolution, but also provides important information which is local measurement area and location according to actual applied frequency and the electrical properties of the measurement environment.

- As the final approach, non-conventional responses in the impedance spectra of a zinc-rich coating system are studied in electrical/electrochemical impedance measurements. The study reminds us of the concepts of non-destructive and steady state conditions about the existing impedance and finds new properties through experiment. Electroanalytical techniques are used to document the electrochemical responses of a ZRP coating in the presence of a ZnO with diode-like behavior. In order to understand the non-conventional impedance response that is expressed by the influence of external transfer function signal, approaches from an electrical and an electrochemical point of view have been studied. The research is undertaken under various temperature and bias potential conditions to analyze phenomena from an electrical standpoint. For the electrochemical approach, all experiments were performed by EIS and OCP in immersed conditions of coating systems. To understand the non-conventional impedance spectra, the charging-relaxation potential model is developed. The bulk ohmic resistance of the system with ZnO as a native product or a corrosion product in the ZRP film is susceptible to exposure to a transfer function signal.

The proposed study will be used as an important guide for optimal design of coating materials through the analysis, as well as a method to interpret the various physical meanings of the system though the impedance spectra.

7.2. Future Recommendations

It is expected that the research will be developed by overcoming the assumptions established in this study and demonstrating the hypotheses. Based on the outcomes of this research and the current status, the following future takes are recommended.

1) Development of optimization algorithms for finding physicochemical properties: The response and its meaning of impedance spectra can be interpreted through the 2D impedance model developed by designing a reasonable coated material environment. However, in order to extract local physicochemical properties from the experimental impedance spectra, a reasonable and logical optimization code is required for the 2D impedance model. The development will enable corrosion researchers to interpret and understand the distribution of local interfacial and bulk properties quickly.
2) Combination with the multi-physics model: The 2D impedance model expresses a system in a steady state condition, such as taking a snapshot of a momentary time. To predict an electrochemical system that changes over time and to express the impedance response that changes accordingly, it is necessary to combine time dependent multi-physics model with the 2D model.
3) It is necessary to focus more on the barrier changes that occur at the interface of the zinc oxide by the external electrical field. In particular, it is needed to observe the electrical characteristics that occur on a low scale through single particles or simple systems for a deeper understanding. In addition, research on the relaxation

time required by various zinc oxide or CNT distributions will also help the development of the electrochemistry field.